INFORMATION TO USERS

This manuscript has been reproduced from the microfilm master. UMI films the text directly from the original or copy submitted. Thus, some thesis and dissertation copies are in typewriter face, while others may be from any type of computer printer.

The quality of this reproduction is dependent upon the quality of the copy submitted. Broken or indistinct print, colored or poor quality illustrations and photographs, print bleedthrough, substandard margins, and improper alignment can adversely affect reproduction.

In the unlikely event that the author did not send UMI a complete manuscript and there are missing pages, these will be noted. Also, if unauthorized copyright material had to be removed, a note will indicate the deletion.

Oversize materials (e.g., maps, drawings, charts) are reproduced by sectioning the original, beginning at the upper left-hand corner and continuing from left to right in equal sections with small overlaps. Each original is also photographed in one exposure and is included in reduced form at the back of the book.

Photographs included in the original manuscript have been reproduced xerographically in this copy. Higher quality 6" x 9" black and white photographic prints are available for any photographs or illustrations appearing in this copy for an additional charge. Contact UMI directly to order.

UMI®

Bell & Howell Information and Learning
300 North Zeeb Road, Ann Arbor, MI 48106-1346 USA
800-521-0600

DYNAMICS OF A VERTICALLY TETHERED MARINE PLATFORM

by

Frederick Ralph Driscoll
B.Eng., University of Victoria, 1994

A Dissertation Submitted in Partial Fulfilment of the
Requirements for the Degree of

DOCTOR OF PHILOSOPHY

In Interdisciplinary Studies
(Department of Mechanical Engineering and School of Earth and Ocean Science)

We accept this dissertation as conforming
to the required standard

Dr. R. G. Lueck, Supervisor (School of Earth and Ocean Sciences)

Dr. M. Nahon, Supervisor (Department of Mechanical Engineering)

Dr. N. Dyilali, Departmental Member (Department of Mechanical Engineering)

Dr. J. S. Collins, Outside Member (Department of Electrical Engineering)

Dr. D. R. Yoerger, External Examiner (Department of Applied Ocean Physics and Engineering, Woods Hole Oceanographic Institution)

Abstract

Rapid and high resolution motion and tension measurements were made of a typical vertically tethered system, a caged deep–sea ROV, while it operated at sea. The system is essentially one–dimensional because only the vertical motions of the underwater platform and the ship were coherent, while horizontal motions of the platform were weak and incoherent with any component of motion of the ship. The natural frequency of the system is found to be within the frequency band of ship motion for most of its operating range and the platform response is weakly non–linear. This results in a vertical acceleration of the platform that is up to 2.2 times larger than that of the ship.

Large vertical excursions of the ship produce momentary slack in the tether near the platform. At the instant prior to re–tensioning, the tether and platform are moving apart and upon re–tensioning, the inertia of the platform imparts a large strain — a snap load — in the tether. The resulting strain wave propagates to the surface with the characteristic speed (3870 ms^{-1}) of tensile waves in the tether. An extremely repeatable pattern of echoes is detectable at each end.

Two models, a continuous (closed form) non–dimensional frequency domain model and a discrete finite–element time domain model are developed to represent vertically tethered systems subject to surface excitation. Both models accurately predicts the measured response, with slightly better accuracy in the discrete version. The continuous model shows that the response is governed by only two non–dimensional parameters. The continuous model is invalid for slack tether and inherently unable to predict snap loads. By slightly increasing the ship motion, the discrete model accurately reproduces the

observed snap loads and their characteristics. Discrepancies between the predicted and measured response of the platform bring into question the concepts of a constant drag coefficient and a constant added mass for oscillatory flow around the platform. By adding a simple wake model to account for flow history, the error in the calculated platform motion and tension in the tether were reduced by almost a factor of 2.

Passive ship–mounted and cage–mounted heave compensation systems were investigated with a view to reducing the cage motion and tension in the tether. Both systems were found to be effective and for reasonable parameters, they can reduce the motion of the cage and the tension in the tether by a factor of 2. Addition of either compensation system reduced the natural frequency of the system and extended the operating sea state of a cage ROV system. However, the characteristics of the compensation systems must be carefully chosen or the operational problems will be exacerbated. In particular, the natural frequency of higher modes may enter the wave–band for deeper operating depths. During extreme sea states, the cage compensated system eliminated all snap loads.

Dr. R. G. Lueck, Supervisor (School of Earth and Ocean Sciences)

Dr. .M. Nahon, Supervisor (Department of Mechanical Engineering)

Dr. N. Djilali, Departmental Member (Department of Mechanical Engineering)

Dr. J. S. Collins, Outside Member (Department of Electrical Engineering)

Dr. D. R. Yoerger, External Examiner (Department of Applied Ocean Physics and Engineering, Woods Hole Oceanographic Institution)

Table of Contents

List of Tables

Appendix A

Appendix B

Appendix C

List of Figures

Appendix A

Appendix B

Appendix C

Appendix D

Nomeclature

$I = [X \quad Y \quad Z]^T$	inertial reference frame with co-ordinates defined in Figure 2.5
$B^C = [x^C \quad y^C \quad z^C]^T$	cage–fixed reference frame with co-ordinates defined in Figure 2.5
$B^S = [x^S \quad y^S \quad z^S]^T$	Ship–fixed reference frame with co-ordinates defined in Figure 2.5
L_{IB}	rotation matrix used to transform vectors to the inertial frame
T_B	transformation matrix from angular rates to Euler rates
$A' = [A'_x \quad A'_y \quad A'_z]^T$	translational acceleration vector, including gravitational acceleration, in the inertial frame
$a' = [a'_x \quad a'_y \quad a'_z]^T$	translational acceleration vector, including gravitational acceleration, in a body frame
$A = [A_x \quad A_y \quad A_z]^T$	translational acceleration vector in the inertial frame
$a = [a_x \quad a_y \quad a_z]^T$	translational acceleration vector in body frame
$\Lambda = [\Lambda_x \quad \Lambda_y \quad \Lambda_z]^T$	angular acceleration vector in inertial frame
$\omega = [\omega_x \quad \omega_y \quad \omega_z]^T$	angular acceleration vector in body frame
$\beta = [\phi \quad \theta \quad \psi]^T$	Euler angles
$r^{MP} = [r_x^{MP} \quad r_y^{MP} \quad r_z^{MP}]^T$	position vector from the cage centre of gravity to the sensor mounting point
$R_B^{CR-MP} = [R_X^{CR-MP} \; R_Y^{CR-MP} \; R_Z^{CR-MP}]^T$	position vector from the point of minimal vertical acceleration of the ship to the instrumentation mounting point on the A–frame
$g = [0 \quad 0 \quad g]^T$	gravitational acceleration
C_{XX} or C_X	auto–specturm of some signal X
C_{XY}	cross–spectrum of signals X and Y
H_{XY}	transfer function between signals X and Y

Γ_{XY}^2	coherency of signals X and Y
σ_X	standard deviation of signal X
A	cross–sectional area of tether
A_C	cross–sectional area of cage
A_P	area of piston
a	vertical acceleration (discrete model)
β_i	boundary condition for the continuity of strain for element i
C_D	non–dimensional cage quadratic drag coefficient
C_{DT}	non–dimensional tangential drag coefficient of tether
C_{pd}	linear damping coefficient of compensator
C_V^{CG}	drag coefficient of cage
C_V^*	linearised drag coefficient of cage
c	speed of sound (tensile waves) through the tether
D	diameter of the tether
Δ_E	static equilibrium position of compensator
Δ_T	total compensator travel
δ	compensator displacement
$\delta_i^{(j)}$	j'th time–dependent coefficient of the trial solution for element i
E	equivalent Young's modulus
ε	local strain in the tether
F	hydrodynamic force on tether
f_i	i'th natural frequency (continuous model)
f_i	hydrodynamic, gravitational, and buoyancy force on element i (discrete model)
f_{HC}	compensator force

$\phi_{i,j}$	j'th shape function of element i
γ	phase between the vertical motion of the ship and age
j	imaginary unit
k	fractional tension range of compensator
L	unstretched length of tether
l_i	unstretched length of tether element i
M	mass of the cage (continuous model)
M_{CG}	mass of the cage (discrete model)
M_{ROV}	mass of the ROV (discrete model)
m	mass per unit length of the tether
N	number of elements in discrete model
n	ratio of specific heats of compensator gas
P	pressure of gas in pneumatic compensator,
P_{eq}	pressure of gas in pneumatic compensator at equilibrium
ρ_C	density of the tether,
ρ_W	density of sea water
R	reduction ratio
S_A	significant A–frame displacement
s	vertical unstretched co-ordinate of the tether
T	tension in the tether
$T' = T'_{stat} + T'_{dyn}$	sum of the non–dimensional static and dynamic tension
T_{HC}	Tension in tether at the compensator
t	time
τ	time lag between the vertical motion of the ship and cage
$U' = v' + w'$	sum of non–dimenstional static and dynamic displacement
$(U_t)_{rms}$	standard deviation of cage velocity

U	local displacement of the tether (continuous model)
$\dot{U}$	velocity of the tether (discrete model)
u	cumulative elastic displacement of tether
$\tilde{u}_i$	approximate elastic displacement of element i
V	volume of gas in pneumatic spring
V_R	accumulator volume
W	weight minus buoyancy of tether per unit length
W_{CG}	weight minus buoyancy of cage
W_T	weight supported by compensator
Ω_C	filter cut–off frequency
ω	angular frequency
ω_i	i'th natural frequency
Y	amplitude of ship displacement
Y_{CR}	critical amplitude of ship displacement at which the tether goes slack
ξ	ratio of drag force on cage to elastic force in the tether
ζ	ratio of cage to tether mass
Z	position of top of the tether
z	vertical location of a point in the tether
$( )_X$	derivative of () with respect to X
$\dot{(\cdot)}$	time derivative
$( )^{(1)}$	upper node (discrete model)
$( )^{(2)}$	lower node (discrete model)
$( )^C$	cage
$( )^S$	ship

Acknowledgements

Thank you, Lisa, for your patience, understanding and love. I appreciate your understanding when I had to stay late at the University or when I locked myself in the back room to complete this work. Your love kept me smiling and sane during the last stages when I felt I was making no progress.

Thank you, Meyer and Rolf for being outstanding supervisors. Your different perspectives have balanced my research so that I addressed problems from both engineering and physics standpoints. Rolf, thanks for the hunting trips where we solved differential equations and fishing trips where we examined the basic physical oceanography of the Strait of Juan de Fuca. Meyer, thank you for pushing me through and keeping me focused.

Thank you, Jim McFarlane and the staff of International Submarine Engineering (ISE) for your continual support and assistance in this project. Jim, you are very inspiring and I consider you one of my mentors.

Thank you, John Garrett, Kim Juniper, Steve Scott, Keith Shepherd, Bob Holland, Captain Anderson and crew of the *CSS John P. Tully* for graciously providing access to the *ROPOS* ROV system and berthing during the experiment.

I am also very grateful for the financial support provided by the Science Council of British Columbia (SCBC), ISE and the Natural Science and Engineering Research Council (NSERC). The project would not have possible without your contributions, thank you.

Chapter 1

Introduction and Motivation

1.1 Vertically Tethered Marine Systems

The ocean is a hostile environment that is inaccessible to humans without support equipment. Initial access to the deep ocean was facilitated by diving bells which limited the occupants to localised observations. As technology advanced, more effective means of working at large depths emerged, including: autonomous underwater vehicles, submersibles, and tethered platforms. All these systems are complementary and provide humans with the ability to explore and work in the world's oceans.

Vertically tethered systems are an important subclass of tethered vehicles that provide safe and effective access to the ocean. Vertically tethered systems manifest themselves in many forms which range from small hydrophones and conductivity/temperature/depth instrumentation (CTDs), which can be lowered from small research vessels and helicopters, to large piston coring tools and Remotely Operated Vehicles (ROVs), which require large support vessels. These systems have many applications, including scientific exploration of deep ocean phenomena; assembly, inspection and repair of undersea structures; and dangerous military operations. All vertically tethered systems consist of an underwater platform that is connected to the support vessel by a flexible tether. In most tethers, layers of steel armour house an inner core of electrical and optical conductors that are used to power and communicate with the supported undersea platform.

The virtue of tethered systems is their ability to perform dangerous tasks in the hostile deep–sea environment while their human operators remain safely onboard the support vessel. In addition to safety issues, tethered systems have many advantages over other manned systems and divers. In particular, tethered systems can stay at the underwater work site indefinitely because their power is supplied by the support vessel, and the crew can be rotated without recovering the system. While the tether provides many advantages, it is also the greatest disadvantage because it couples the ship motion to the undersea unit. As a result, operation in rough seas may result in slack tether and large 'snap' loads — a large strain wave that is induced in the slack tether when it is rapidly re–tensioned — which can cause structural damage to the tether (umbilical cable) and its internal electrical and optical conductors. The resulting degradation reduces the life of the cable and endangers the recovery of the underwater platform. With damaged conductors, communication and power to the underwater system is cut off and the system becomes inoperable. Additionally, snap loads can jerk the undersea platform and damage its instrumentation and other delicate parts. Large vertical displacements of the platform can also occur when operating in rough seas which may degrade the quality of measurements and make landing on the ocean floor difficult. In the case of an ROV system, the vehicle is loosely attached to a large cage at the end of the tether. The ROV remains vertically stationary in the water while the cage oscillates rapidly and this makes docking difficult, if not impossible.

Examples of the problematic dynamic characteristics of vertically tethered systems are common. For example, during a two week expedition in rough weather, the *ROPOS* (Remotely Operated Platform for Oceanographic Science) ROV (an International

Submarine Engineering Hysub 5000, ISE 1998) only logged five hours of operation; its main umbilical tether had to be re–terminated because the optical conductors were broken by many snap loads; and the tether connecting the cage and ROV was sheared during a docking attempt due to the large vertical motion of the cage. This damage was costly but the down time resulting from the limited operating window is much more expensive. In this case, the five hours of operation cost approximately $280,000. On a larger scale, drill ships are more expensive to operate and operators can lose millions of dollars on a single well due to down time resulting from rough operating conditions.

Clearly, knowledge of the dynamic characteristics of vertically tethered systems are needed to predict safe operating conditions and to design dynamically well–behaved systems. However, intuitive understanding of vertically tethered systems is difficult because the tension and motion are transmitted as a strain wave with finite and frequency–dependent speed along the tether (only when taut) and the undersea platform is subject to non–linear drag and added mass. Experimental measurements and analytic models can provide this knowledge.

Although we may be able to design tethered systems that effectively operate in normal sea conditions, storms can develop quickly and rapidly increase the sea state. Operating in rough conditions may be unavoidable because tethered systems can take many hours to recover when working at large ocean depths. Therefore, it is necessary to develop mechanisms that uncouple the motions of the ship from the undersea platform because this would increase the maximum operating sea state and provide safe recovery in the event of extreme weather.

1.2 Previous Work in Tethered Underwater Systems

Experimental measurements are the most reliable but the most costly method of quantifying the dynamic characteristics of vertically tethered systems. Measurements of vertically tethered systems are uncommon and limited to the pressure and tension records of CTDs (Garrett, 1994) and acceleration and rate gyro records of diving bells and submersibles during launch and recovery (Mellem, 1979). Measurements of other tethered systems are more common. Some excellent examples are Grosenbaugh (1996) who measured the motion and tether tension of a deeply moored buoy and Yoerger *et al.* (1991) and Hover and Yoerger (1992), who measured the motion of a deeply towed underwater vehicle system. I did not find any work that uses motion and tension measurements to perform a fundamental analysis of the dynamics of the tether that couples the surface ship and undersea platform during operation in typical and rough seas.

In comparison with experimental measurements, analytic models provide a less costly and more versatile method of quantifying the characteristics of dynamic systems. Two different modelling techniques are available to predict the response of tethered systems — continuous (closed-form analytical) and discrete models. Continuous models can provide quick estimates of many of the dynamic characteristics of tethered systems, including motion and tension spectra, transfer functions, the natural frequencies, and the onset of slack in the tether. Both Niedzwecki and Thampi (1991) and Huang and Vassalos (1995) used a single degree–of–freedom model to characterise the response of a vertically suspended mass to sinusoidal forcing. These simple models provide a first order approximation to vertically tethered systems but they ignore the mass of the tether

(drill string in the case of Niedzwecki and Thampi (1991)) which is an important factor in the response of the system. In an earlier publication Niedzwecki and Thampi (1988) also derived a set of closed form solutions to a series of equations that represent a heave–compensated, multi–segment drill string. This model included the drill sting mass, but used a computational double sweep recursive process to calculate the response. An analytical model with a single closed form solution that includes the mass of the tether would be useful because it would provide a quick (non computational) tool to accurately predict the response of vertically tethered systems.

Continuous models are effective tools but they have limitations. Equivalent linearization techniques are used to approximate the quadratic drag for steady amplitudes which enables closed form solutions and frequency–domain analysis (Caughey 1963; and Grosenbaugh 1996). Thus, these models are not appropriate when the sea state is time dependent (non–stationary). Continuous models are also invalid for a slack tether, which is the precursor to snap-loads, and it is difficult (if not impossible) to solve the differential equations governing a tether when its properties are length dependent. Discrete models are not necessarily constrained by these limitations and they are valid for a wider range of operating conditions and system configurations. For example, they can encompass non–linear properties, such as quadratic drag, temporally/spatially varying properties, and different slack and taut tether representations. Additionally, a discrete implementation can be quickly assembled to model multi–component systems connected by tethers with different properties. Components, such as ROV cages, weights/floats, and intermediate platforms can be easily added because they are each represented as a point

mass and the hydrodynamic, gravitational and buoyancy forces acting on them are described by one differential equation.

Niedzwecki and Thampi (1991) developed a discrete multi–segment lumped–parameter representation of a drill string connecting a ship to a subsea package and used it to investigate snap loading. Driscoll and Biggins (1993) used a similar lumped parameter model to perform a preliminary study of a caged ROV system. Although discrete models of strictly vertical system are rare in the literature, discrete models of towed systems are more common and their axial equations of motion are similar to those of vertically tethered systems (Sanders, 1992, Ablow and Schechter 1983, and Hover et al 1994).

Both continuous and discrete representations do not model all the dynamic processes acting in/on vertically tethered system and both use simplifying assumptions (linearization, constant drag and added mass coefficients, linear elasticity, straight elements, etc.) to reduce the complexity of predicting the response. Thus, validation against experimental data is necessary to prove accuracy. However, validation of the predicted axial response of these systems against data is virtually non–existent. A refreshing example is Grosenbaugh, 1996, who compared motion and tension measurements of a long vertically tethered surface mooring with his continuous model. The model was accurate but its lower boundary condition is fixed and the mooring system is therefore different from vertically tethered systems. Clearly, a fundamental validation of the models of vertically tethered systems would prove their usefulness and identify their limitations.

To solve the problems of operation in rough seas outlined in the previous section, both continuous and discrete models have been used to investigate and design ship–mounted heave compensation systems to uncouple the ship and cage motions. Much effort has been devoted to the design of actively controlled heave compensation (HC) systems to reduce the heave motion and dynamic tension of drill strings and tethered systems (Korde, 1998, Kirstein, 1986, Bennet and Forex, 1997, Gaddy, 1997). For active systems to work well, the dynamic characteristics of the overboard system must be accurately known so that depth dependent gains are chosen appropriately. Additionally, active systems are complicated and require significant support equipment. Passive ship–mounted heave compensation systems have also been examined because they provide a simpler design but they have received less attention. Both Hover *et al.*, 1994 and Niedzwecki and Thampi, 1988 present excellent analyses of passive systems. Hover investigated a ship–mounted system for a deeply towed body by varying the values of the compensator's linear stiffness and damping over a range of sea states at a single operating depth. Both works show that a poorly chosen stiffness of the compensator can increase both the displacement of the platform and the tension in the tether. No work as been found that investigates the effectiveness of a bottom mounted heave compensation system.

1.3 Contributions of this Dissertation

The purpose of my work is to further the field of vertically tethered underwater systems by providing:

- a fundamental understanding and characterisation of the dynamics of vertically tethered system;

- a set of accurate and validated mathematical tools to help predict and understand the response to ship forcing; and
- a numerical implementation of a passive heave compensator and an investigation of its effectiveness for different operating parameters and mounting locations.

One vertically tethered system that was readily available for investigation was the *ROPOS* deep sea ROV system (Figure 1.1). This ROV is dynamically similar to most tethered systems and suffers from all of the operational problems. Therefore, *ROPOS* is used as a case study in my research.

The first contribution is achieved by analyzing rapid and high resolution motion and tension measurements of *ROPOS*. Both temporal and frequency domain techniques were used to extract the fundamental dynamic characteristics, such as the natural frequencies and the magnitude and phase of the platform response, from the data. Additionally, several snap loads were measured and this provided sufficient evidence to determine the cause and major characteristics of such loads.

For the second contribution, I develop and validate a continuous non–dimensional model (which includes the mass of the tether and has a single closed form solution) and a finite–element lumped–mass model of a vertically tethered system. The continuous model is used to provide quick and accurate predictions of the response of the undersea platform and tension in the tether. As well, a discrete model is developed because it is more versatile than the continuous model and has a larger range of validity, including slack tether. Both representations are developed using widely accepted equations for visco–elastic tethers and in the finite–element model, a standard discretization method is

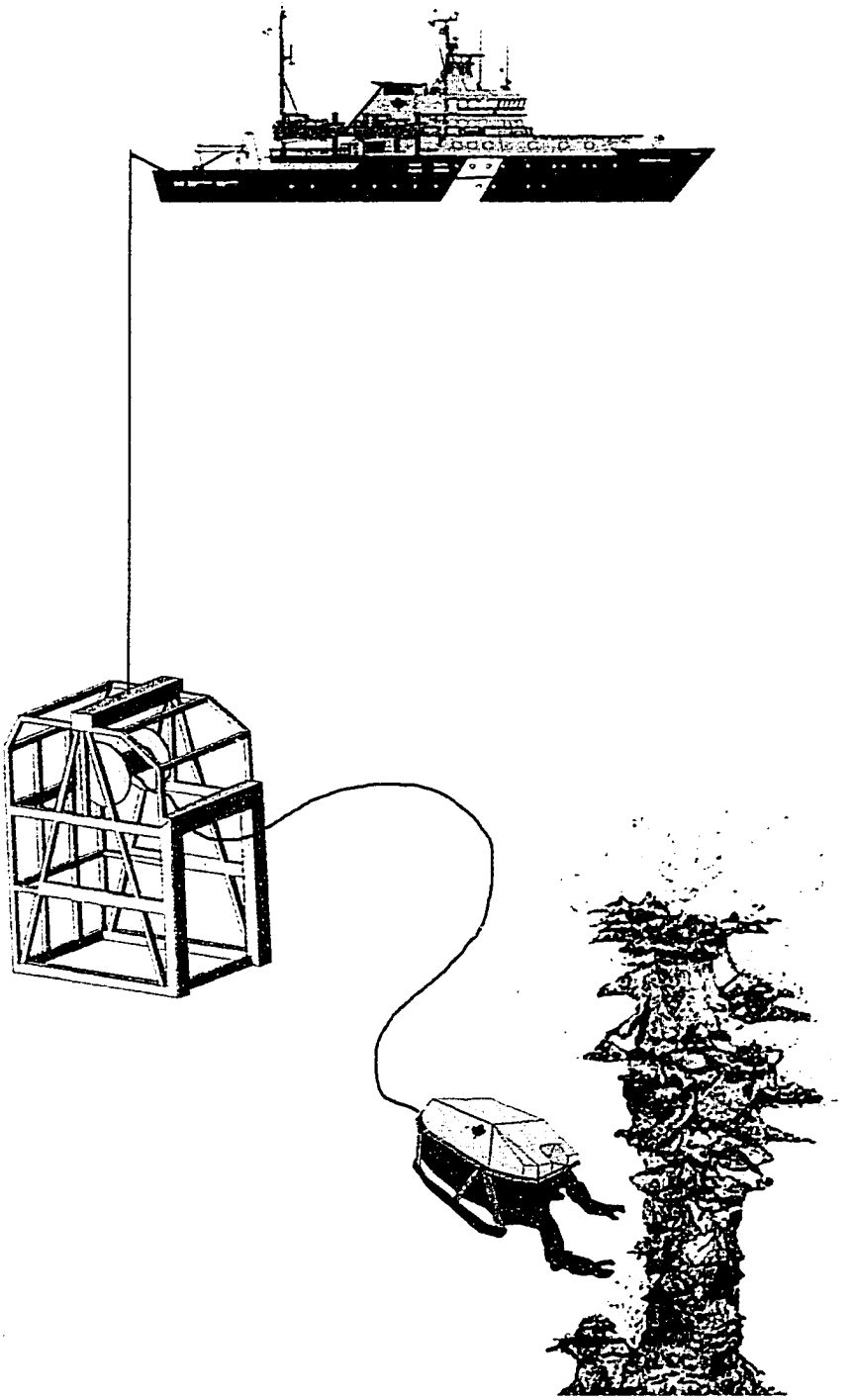

Figure 1.1: Diagrammatic representation of the ROPOS ROV system consisting of a support ship (C.S.S. John P. Tully), winch, umbilical tether, cage and vehicle. ROPOS is investigating the actively-venting sulphide structure Godzilla (Robigou, 1993).

applied to the tether equations. Each model is formally validated against the experimental measurements.

In the third contribution, I develop a discrete representation of a passive heave compensator. This discrete representation is used in my finite–element model to investigate both ship–mounted and cage–mounted heave compensation systems over a large range of compensator stiffness and operating depth. Fundamental characteristics such as the natural frequencies and transfer functions are used to evaluate and characterise the effectiveness of the compensators at attenuating platform motion and tension in the tether. Additionally, the performance of the compensated systems are quantified for extreme operating conditions.

1.4 Dissertation Organisation

My contributions are contained in four logically progressing papers which are entitled:

- The Motion of a Deep–Sea Remotely Operated Vehicle System. Part 1: Motion Observations (Driscoll *et al*, 1999a);
- The Motion of a Deep–Sea Remotely Operated Vehicle System. Part 2: Analytical Model (Driscoll *et al*, 1999b);
- Development and Validation of a Lumped–Mass Dynamics Model of a Deep–Sea ROV System (Driscoll *et al*, 1999c); and
- A Comparison Between Ship–Mounted and Cage–Mounted Passive Heave Compensation Systems (Driscoll *et al*, 1999d).

These papers are contained in appendices A, B, C and D, respectively. The body of this dissertation is divided into four chapters, Chapters 2 to 5, which correspond to each of the appendices and explain the methods and procedures used, my contributions, and provide

the relationships between these papers. In chapter 6, the findings and contributions are summarised and I discuss the outstanding problems and make recommendations for future work.

Chapter 2

Motion Observations

The lack of data and the need to understand the dynamic characteristics of real tethered systems led to an extensive field test in which we measured the motion and tension of the *ROPOS* ROV system. Motion and tension data were collected while the system operated over the Juan de Fuca Ridge, approximately 200 km off the coast of British Columbia, Canada. Measurements were made for five dives and included deployment (descent to bottom), recovery (ascent to ship) and near bottom operation. The maximum depth was 1 765 m and sea conditions were moderately rough. Typical vertical displacements of the sheave were 2 m, peak–to–peak, and several intervals of calm and rough seas led to displacements of 1 and 4 m, peak–to–peak, respectively (Appendix A, Section 4).

ROPOS consists of a support ship (Figure 2.1), cage (or intermediate platform, Figure 2.2), vehicle (Figure 2.3), and an umbilical tether (Figure 2.4). The support ship contains all surface equipment necessary for system operation and includes the winch, the power generators, the control console, and the crew. The vehicle itself is capable of diving to 5 000 m, weighs 26 700 N in air and has dimensions of 1.45 m × 2.6 m × 1.7 m (WLH). A 300 m retractable neutrally buoyant tether attaches the ROV to the cage which acts as a garage where it resides during deployment and recovery. The cage is essentially a large weight that keeps the underwater system directly below the ship and contains many of the electronic systems and power supplies needed by the ROV. The cage weighs 49 000 N in air and has dimensions of 2.1 m × 3.4 m × 4.2 m (WLH). The tether

connecting the ship and cage has three layers of steel armour surrounding a core of electrical and optical conductors. The tether is 3 cm in diameter, 4 200 m long, weighs 30.5 Nm^{-1}, and has a maximum working load and breaking strength of 200 000 N and 550 000 N, respectively.

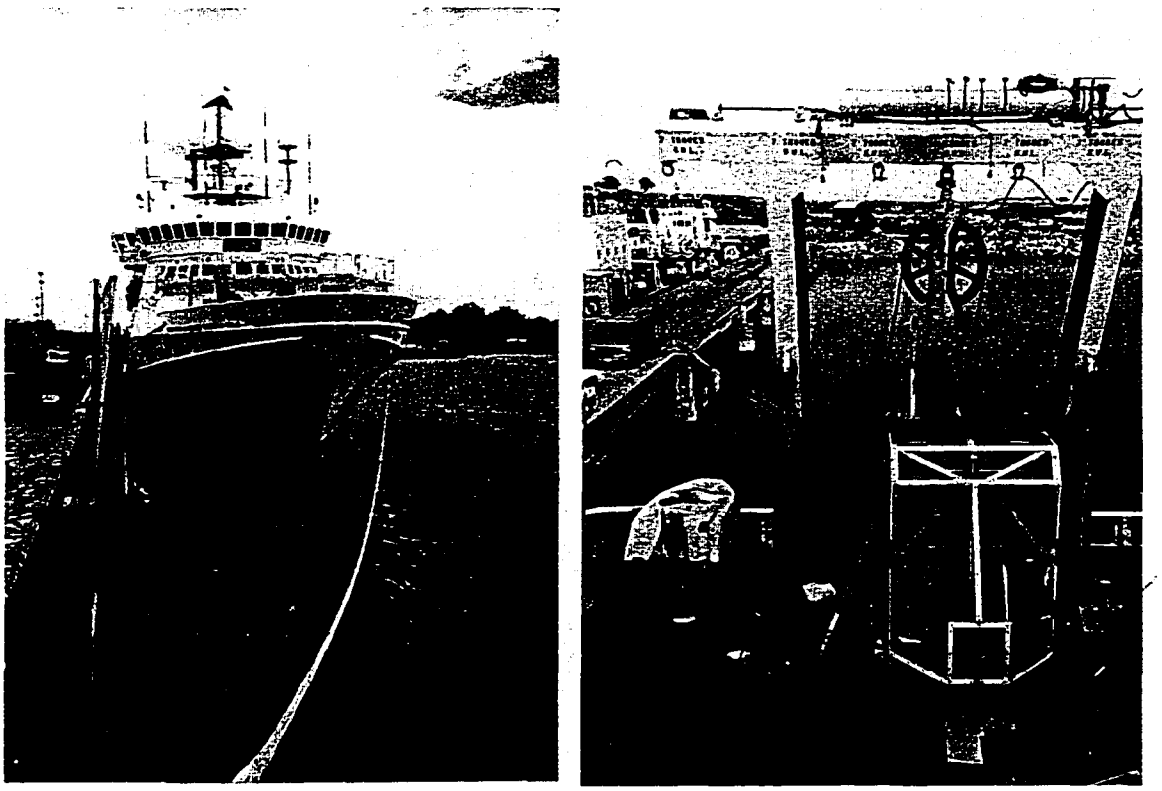

Figure 2.1: Forward and deck views of the *C.S.S. John P. Tully*. The ROV, cage and A–frame are shown in the deck view.

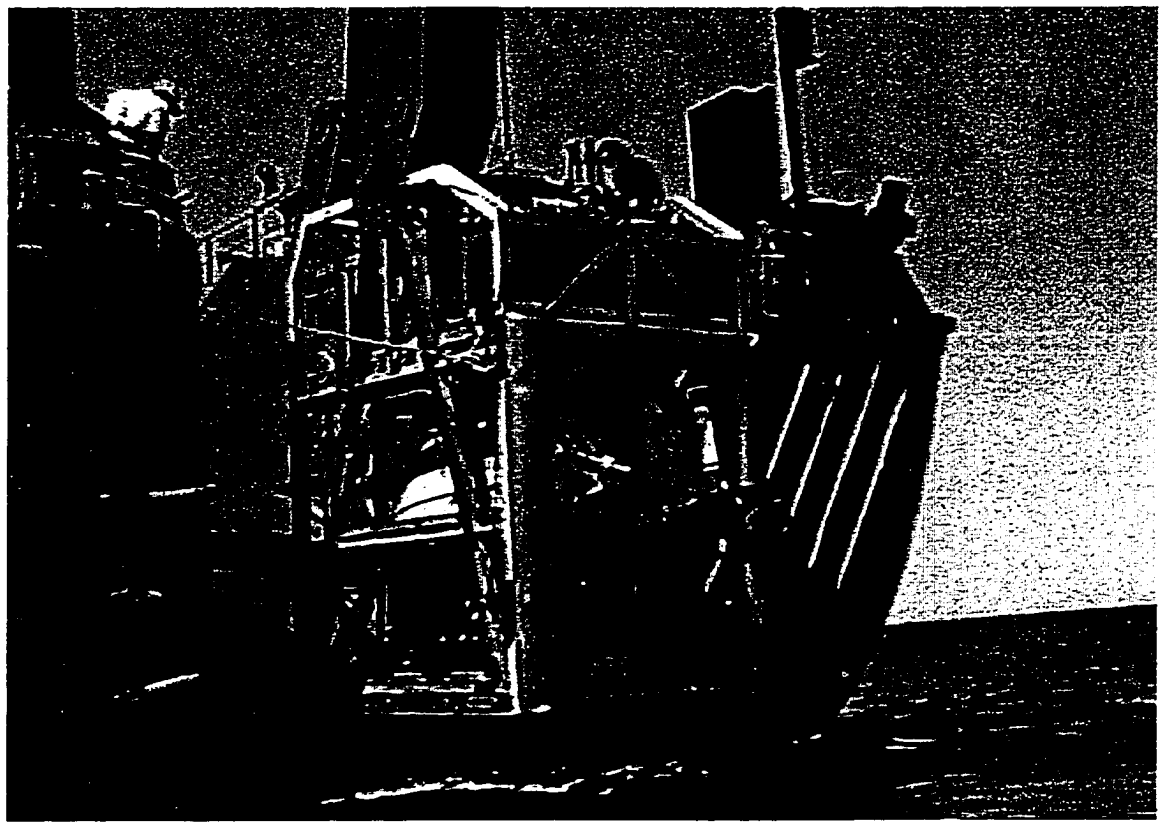

Figure 2.2: ROPOS in the cage during a launch from the *R/V Sonne*

Figure 2.3: The ROPOS remotely operated vehicle

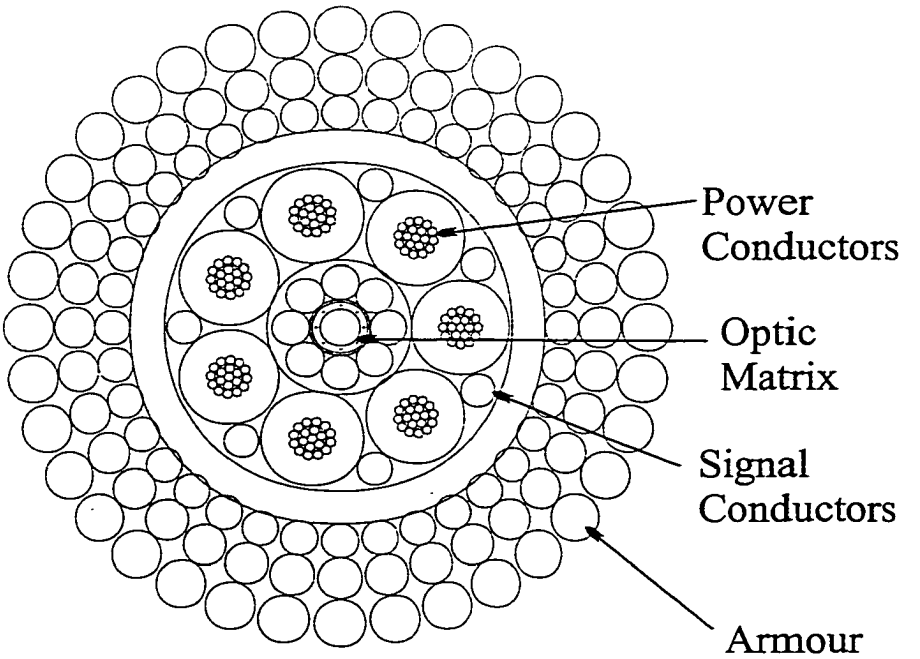

Figure 2.4: A cross–section of the tether used in the ROPOS ROV system.

2.1 Data Acquisition and Processing

We wanted to measure the motion of the tether at the ship, the motion of the cage and the tension in tether. Therefore, we instrumented the top of the ship's A–frame (directly above the sheave that supports the tether) and the top of the ROV cage with tri–axial accelerometers and rate gyros. A pressure sensor was installed on the cage to measure depth and a load cell was used in the axle of the sheave to measure tension. Data were acquired by the real time Ocean Data Acquisition System (Appendix A, Figure 2, from hereon I use the format – Figure A2) which communicated sampling commands and data serially between the ship–board computer and the remote instrumentation sites. The data, collected from the A–frame and cage, were synchronised in time and can be related at any instant even though they were separated by up to 1 765 m.

The ship and cage rotate differently and thus, the measurements from each site (the ship–fixed and cage–fixed frames of reference) were transformed into a common

inertial (earth–fixed) frame of reference for comparison (Figure 2.5). The Euler angles (Etkin, 1972, Chapter 4) were synthesised iteratively from a combination of accelerometer and rate gyro measurements and they were used to transform the acceleration measurements (Figure A3) . Once transformed, the acceleration signal were integrated using filtering techniques (Antoniou, 1979) to obtain records of velocity and position of the ship and cage.

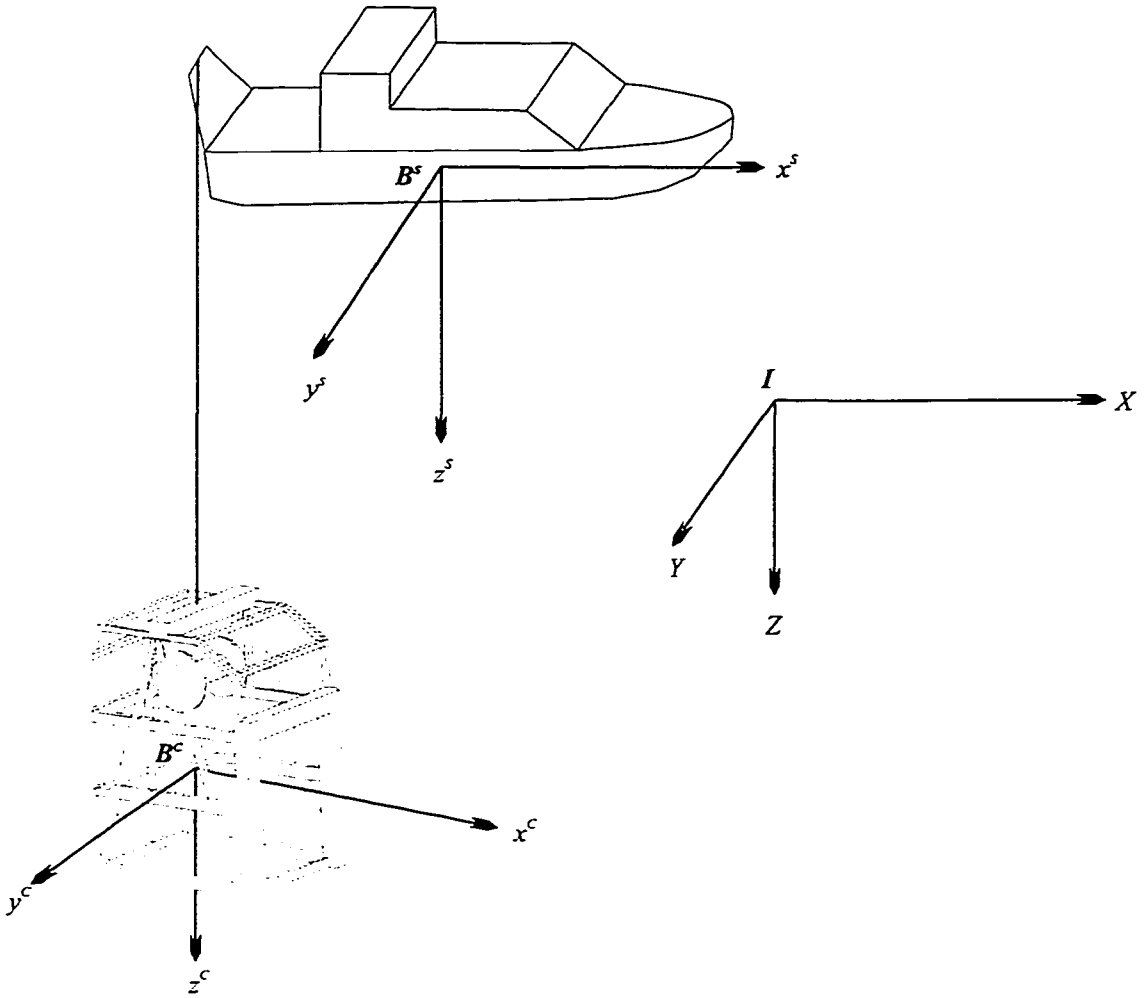

Figure 2.5: Body–fixed and inertial (earth–fixed) reference frames.

2.2 Wave–Frequency Motion Observations

Translational acceleration of the support ship occurs in two frequency bands, the low–frequency band and the high–frequency band, which are separated by a spectral gap at 1.4 Hz (Figure A4). Variance in the low– frequency band is due to swell and developed wind waves while the high-frequency variance has been attributed to mechanical vibrations of the ship. The spectral distribution of ship motion will not change for other sea states because the motion of waves that are much shorter (high frequency) than the hull length will always be greatly attenuated while the mechanical vibrations will not change in frequency with varying sea state. Within the low–frequency band, we restricted the analyses to the range of 0.1 to 0.25 Hz that contains 90% of the variance of the vertical acceleration and we denoted it as the *wave–band.*

In the absence of time varying currents or large horizontal excursions of the support vessel, coherencies between all six degrees of motion of the ship and cage show that the ship and underwater platform are only coupled vertically (Figure A15). The displacements of the underwater platform due to surge, sway, roll, pitch, and yaw motions of the ship are small compared to the vertical scale O(1:1000) of the tether and such motions are not effectively transmitted by the tether. Analysis of the translation and rotation of the ship show that most of its heave is due to the pitching of the vessel about its nominal centre of gravity (CoG). Therefore, vertical motion imparted to the overboard system can be significantly reduced by reducing the distance between the CoG and the A–frame.

One major finding is that the cage response is weakly non–linear, although it is subject to quadratic drag. This is evidenced by the relative variance at the odd harmonics of the fundamental frequency of excitation which is trivial (~2% of the total variance).

The magnitude of the transfer function between the ship and cage, $\left|H_{z^s z^c}\right|$, is asymmetric and peaks at a slightly lower frequency than the first natural frequency, f_1, of the system (Figures A6 and A7). Thus, with symmetric forcing, more motion is transferred from the ship to the cage at frequencies less than f_1 than at frequencies above the natural frequency. The tether's stiffness in inversely proportional to its length and the natural frequencies of the system decrease (increase) with increasing (decreasing) operating depth. Consequently, the peak of $\left|H_{z^s z^c}\right|$ moves to lower (higher) frequencies and increases (decreases) in value with increasing (decreasing) operating depths. This implies that there exists a critical depth for which the frequency of the maximum ship motion and the peak of the transfer function nearly align and the cage motion will be maximised. We estimate this depth to be 2 500 m. We also estimate that f_1 will be within the wave –band between 1 450 and 5 000 m and thus, the system will be in resonance for most of its operating depths. Measurements reflect this — the vertical motion of the cage is larger than that of the ship (Figure A5). Another important consideration is that the second and third natural frequencies decrease with increasing operating depth and they will move into the wave–band at deeper depths. Other vertical systems have similar non–dimensional parameters (discussed in Chapter 3) and will likely suffer from the same resonance conditions.

At wave frequencies, the phase between the ship and cage motion changes non–linearly with frequency and the lag of the cage changes significantly through the wave–band. As a result, the time histories of ship and cage motion will not be identical. Instead, the various spectral components of the motion of the ship will be phase shifted by different amounts as they propagate down the tether.

2.3 Snap Loads

The motion of the system during a snap load is different from that during typical operation and exhibits discontinuous and rapidly changing characteristics (Figure A8). All snap loads that we measured are characterised by a regular series of jerks (defined in Hibbeler, 1989 as the rate of change of the vertical acceleration) of the cage and corresponding rapid increases in the tension in the tether at the surface (Figure A10). Snap loads occur when the slack tether at the cage is rapidly re–tensioned. At the instant that slack disappears, the cage and tether are moving apart. The inertia of the cage is large and therefore it induces a large strain in the tether as it is accelerated to the velocity of the tether. The resulting strain wave propagates up the tether at a speed equal to the longitudinal speed of sound in the tether and reflects at the ends of the tether. This results in regularly spaced rapid increases in cage acceleration. A similar pattern of tension spikes occurs at the ship and this pattern is delayed by the travel time of the strain wave along the tether.

The maximum tension caused by a snap load did not exceed the manufacturer's recommended working limit and it is, therefore, unlikely that the induced strain could have caused any structural or conductor damage. However, the cage pitched when the

tether was slack because the centre of weight and buoyancy are horizontally offset (Figure A10). When re–tensioned, the tether is bent tightly and beyond the minimum radius of curvature recommended by the manufacturer at the cage termination. This likely fractured the fibre optic conductors and stressed the steel armour. Additionally, the cage was accelerated by up to half of the acceleration of gravity and this could shake free electrical and mechanical components.

2.4 Discussion

The operating problems of the *ROPOS* ROV are common to other vertically tethered (and likely deeply towed) systems and may degrade their performance. For example, CTDs are delicate instruments that are used to obtain profiles of sea water properties. Vertical excursions create turbulence that disturbs the water around the CTD and contaminates the measurements. Also, the jerk from a snap load would likely disrupt the water flow through the CTD rendering measurements made at that time meaningless.

To obtain smooth profiles, free falling instruments have been developed. These instruments are typically connected to the ship by a light tether that is used for communication and recovery. During descent, the tether is fed out rapidly so that slack builds on the surface and the vehicle is essentially decoupled from the ship. However, during recovery, slack can occur at the surface because the tether is nearly neutrally buoyant and it falls slowly through the water but rapidly through air. The resulting snap loads can damage the tether and shake the body violently (Lueck, 1999). In this case, the snap loads starts at the surface.

Clearly, vertically tethers systems must be designed to be dynamically well behaved and, for safety's sake, operators must be aware of the dangerous operating conditions. Since motion measurements are expensive and not always possible, tools are needed that can predict the response of tethered systems. In the next two sections we develop a continuous model and a discrete model that represent the *ROPOS* ROV system. The motion observations have outlined many characteristics that can aid in the development of these models. In particular, the only significant relationship between the ship and cage is in the vertical direction in the absence of strong cross–currents. Thus, the remaining five degrees of freedom need not be modelled and a one–dimensional model of the vertical system should be sufficient to accurately reproduce these measurements. The striking characteristics of the ROV system also provide challenging tests for the models. Realistic models should reproduce: (*i*) the transfer function between ship and cage motions (both magnitude and phase), (*ii*) the natural frequency and harmonics, and (*iii*) the regular pattern of rapid increases in the cage acceleration and tether tension during a snap load.

Chapter 3

Continuous Model

Analytical models are attractive tools in the design and analysis of tethered systems because they can be used to predict the behaviour of system during the design process while avoiding the expense and time of iterative prototyping and sea trials. They can also be used to evaluate existing systems without the cost of experimental measurements. Two modelling techniques were introduced in Chapter 1: continuous (closed form) and discrete models. Discrete models are valid over a wider range of conditions than continuous models but they can be difficult to set up, require large computer resources and take long periods of time to investigate a few simple cases. Continuous models have a smaller range of validity than discrete models but they can quickly calculate the important dynamic characteristics of tethered systems. In this chapter, we summarise the development and validation of a continuous one–dimensional linearized model and its closed form solution. The details are given in Appendix B.

3.1 Analytical Model

In the absence of time varying currents or large horizontal excursions of the support vessel, vertically tethered systems are only excited by heave motion and horizontal and rotational motions are not transmitted to the undersea platform Additionally, the response of the underwater platform was found to be weakly non–linear within the range of measurements presented in Chapter 2. Therefore, a one–dimensional linearized analytic model is sufficient to represent most vertically tethered systems. The tether is approximated as an elastic rod and its elongation is described by a hyperbolic

equation (Rao Chapter 8, 1990). Gravitational effects are described by a depth dependent load and the fluid drag on the tether is small enough to be ignored. The general linear–elastic tether equation is:

$$\frac{EA}{m}U_{zz}+\frac{g(\rho_C-\rho_W)A}{m}=U_{tt} \tag{3.1}$$

where z is the vertical unstretched position along the tether, $U(z,t)$ is the local displacement of the tether, t is the time, E is its equivalent Young's modulus, A is its cross–sectional area, m is its mass per unit length, g is the gravitational acceleration, ρ_C is the density of the tether and ρ_W is the density of sea water. The vertical motion of the A–frame is assumed to be known and is modelled as a harmonic displacement function applied to the upper end of the tether. The underwater platform is represented as a point mass subject to gravity, buoyancy, drag, and the tension in the tether. The response of the underwater platform is weakly non–linear and we used an equivalent linearization of the quadratic drag (Caughey, 1963). Therefore the boundary condition at the lower end of the cable is:

$$U_z(L,t)=\frac{1}{EA}\left(W_{cg}-C_V^*U_t(L,t)-MU_{tt}(L,t)\right) \tag{3.2}$$

where C_V^* is the equivalent linear–viscous drag coefficient of the platform, W_{CG} is the weight minus buoyancy of the platform, M is the mass of the platform (including entrained and added mass) and L is the length of the tether.

For generality, the governing differential equation and its boundary conditions are non–dimensionalized and the resulting closed form solution is divided into two independent parts, a static and a dynamic solution. The static solution is:

$$v'(z') = -\frac{\beta}{2}(z')^2 + \left(\frac{W_{cg}L}{YEA} + \beta\right)z' \tag{3.3}$$

where

$$\beta = \frac{L^2}{Yc^2}\frac{g(\rho_C - \rho_W)A}{m},$$

and the non–dimensional parameters are denoted by $(\cdot)'$. The dynamic part is solved in the frequency domain and its solution is:

$$w'(z',t') = \frac{\left(\{\sin\omega' + \sigma\cos\omega'\}\sin\omega' z' + \{\cos\omega' - \sigma\sin\omega'\}\cos\omega' z'\right)e^{j\omega' t'}}{\cos\omega' - \sigma\sin\omega'} \tag{3.4}$$

where

$$\sigma = \zeta\omega' - j\xi, \qquad \zeta = \frac{M}{mL}, \qquad \xi = C_V^*\sqrt{\frac{m}{EA}}, \qquad \omega' = \omega\frac{L}{c},$$

ω' is the non–dimensional frequency and the two non–dimensional parameters ζ and ξ represent the cage–to–tether mass ratio and the drag force on the underwater platform–to–elastic force in the tether ratio respectively. They may also be considered as the dimensionless mass of the platform and its dimensionless drag.

The dimensional model is a function of several dimensional variables; however, when the frequency is non–dimensionalized by L/c, the response at any given frequency

is determined by only ζ and ξ. This implies that designers need only determine optimal values for these two non–dimensional coefficients instead of five dimensional variables. Since the non–dimensional variables are functions of five dimensional variables (M, E, A, m, and C_V^*), there is flexibility in design because the optimal values for the non–dimensional variables can be achieved using different combinations of those five dimensional variables.

3.2 Predictions and Discussion

We validated our closed form solution by comparing the model output against the measured behaviour of the *ROPOS* ROV system presented in Chapter 2. For the validation, the most accurate results for $L = 0 - 1730$ m were obtained by using $\xi = 0.93$ and $\zeta = 1.78$. These values only differed by 14 and 16.5% from the values that were calculated using empirical data for the drag coefficient and added mass and the manufacturer's specification for the tether. We found that our model accurately predicts: i) the natural frequencies (Table B1), ii) the transfer function of ship–to–cage acceleration, velocity and displacement (Figures B2 and B3), and iii) the transfer function between the ship motion and tension in the tether at the ship (Figures B4 and B5). Most predictions were within the 95% confidence interval of the wave–band measurements. We also calculated the sensitivity of our model to the non–dimensional model parameters and found it was robust and stable. In particular, we found: i) the first natural frequency is insensitive to variations in ζ and ξ, ii) the higher order natural frequencies are nearly independent of ζ and ξ (Table B2), and iii) the transfer function between the motion of

the ship and cage and between the motion of the ship and tension in the tether are only moderately sensitive to variations in ζ and ξ (Figures B7, B8, and B9).

For comparison with the parameters of the *ROPOS* ROV system ($\xi = 0.93$ and $\zeta = 1.78$), the parameters for a more streamlined and massive platform (a piston coring tool) and a less streamlined platform (a water sampling rosette) are $\xi = 0.46$ and $\zeta = 2.50$; and $\xi = 1.27$ and $\zeta = 1.9$, respectively for $L = 1\,730$ m. These values are reasonably close (within a factor of 2) to those for the *ROPOS* system, and therefore, our model should be valid for most tethered systems and each of these systems will have similar dynamic characteristics. Of particular interest, the magnitude of the transfer function between ship and platform motion will not be reduced by reasonable changes in ζ and ξ. That is, minor alterations in the system cannot reduce the motion of the cage so it is less than that of the ship.

Measurements in Chapter 2 show that when any of the natural frequencies occur in or near the wave–band, the cage motion will be larger than the motion of the ship. These conditions make operation difficult and would likely result in snap loading. Therefore, the ability to accurately predict these frequencies during a design is important for the development of a safe, reliable and effective system. We found that the natural frequencies are nearly independent of the cage drag and can be accurately calculated using:

$$\omega_i' \tan(\omega_i') = \frac{1}{\zeta}. \tag{3.5}$$

By analysing (3.5) we found that the second and higher order natural frequencies occur at integer multiples of 0.5 and are nearly independent of ζ. This is also reflected in our measurements (Figure B1). The first natural frequency changes only slightly when the value of ζ is varied. This has significant implications because many other vertically tethered systems have similar values of ζ and are likely operating in resonance.

Predicting the tension in the tether for any given sea condition is important because it provides a quantitative criterion for the selection of a tether. We developed a simple and accurate non–dimensional transfer function between the ship motion and tension in the tether. The total (static + dynamic) tension is largest at the surface and the transfer function at that point is:

$$H_{Z^S T^S} = \frac{\omega'(\sin\omega' + \sigma\cos\omega')}{(\cos\omega' - \sigma\sin\omega')} + \left((1-z')\beta + \frac{W_{cg}L}{YEA}\right)e^{-j\omega' t'} \tag{3.6}$$

Predicting the tension at the cage is useful because it can be used to predict the sea conditions for which the tether becomes slack and snap loading will occur. Although the model is only valid when the tether is taut, it can be used to predict the critical amplitude of ship motion that the tether tension at the cage goes to zero:

$$Y_{CR} = \frac{\frac{W_{cg}L}{EA}}{\left|\frac{\omega'\sigma}{\cos\omega' - \sigma\sin\omega'}\right|} \tag{3.7}$$

We validated (3.7) by overlaying plots of Y_{CR} estimated from the model and Y that contains 99% of the measured amplitudes (in the wave–band) in a long record in which a

few snap loads occurred in extreme conditions (Figure B6). Slack tether occurs when $Y_{CR} > Y$. Indeed Y did exceed the lines of zero tension over a small range at higher frequencies in the wave–band. Thus, (3.7) provides a relatively simple, quick and accurate means of determining the safe operating range of most tethered systems and their susceptibility to snap loading. However, it implicitly assumes a single frequency wave, when, in reality, waves energy is spread over a band of frequencies.

Our continuous model provides quick and accurate estimates of the dynamic characteristics of vertically tethered systems. However, our model has limitations. The actual drag acting on the cage is quadratic, but it is linearized for a "steady" amplitude of vertical motion. Thus, our model is not appropriate for unsteady wave conditions. Our model is also invalid for a slack tether, which is the precursor to snap-loads. Finally, properties of the tether must be uniform along its length.

Chapter 4

Finite–Element Lumped–Mass Model

Discrete models are not constrained by the limitations of continuous models and they are valid for a wider range of operating conditions and system configurations. We chose a finite–element implementation because it is versatile and can model the complicated characteristics of vertically tethered systems. In this chapter, we give an overview of the development and validation of a one–dimensional finite–model lumped–model of a vertically tethered system. The details are given in Appendix C.

4.1 Model Development

The system is broken down into three individual sub–systems: the support ship with its A–frame, the tether, and the cage and ROV. As in Chapter 3, a one–dimensional model is sufficient. The model is developed using a single inertial reference frame located at the mean sea surface, with downward displacements defined as positive. We represent the tether as a long elastic cylinder that is suspended directly below the ship's A–frame and the balance of forces (per unit length) at any point in the tether is:

$$\frac{\partial T}{\partial s} + W + F = ma \tag{4.1}$$

where s is the vertical unstretched co–ordinate along the tether, $W(s)$ is the *in situ* weight (per unit length), $T(s)$ is the tension in the tether, $F(s)$ is the hydrodynamic force (per unit length), and m is the effective mass (per unit length including entrained water).

Although (4.1) is in a slightly different form than the governing equation (3.1) used in the continuous model, in the limit of zero tether drag and linear cage drag, they are identical.

The tether is discretised by first dividing it into N segments (elements) which have the same properties as the continuous tether and the location of any point is defined using a coupled set of reference and elastic co-ordinates (Shabana, 1989). The end points of each element are denoted as the nodes of the system. We use an elemental trial solution with a linear shape function to approximate the elastic displacement at any point in an element. By applying Galerkin's method of weighted residuals (Burnett 1987) to (4.1) (Appendix E) and replacing the consistent–mass matrix with a lumped–mass matrix (Logan 1992) to uncouple the acceleration terms, we obtain the following finite–element equations of a visco–elastic tether element i:

$$\frac{m_i l_i}{2}\begin{bmatrix}\ddot{Z}\\ \ddot{Z}\end{bmatrix}+m_i l_i\begin{bmatrix}1/2 & 0\\ 0 & 1/2\end{bmatrix}\begin{bmatrix}\ddot{u}_i^{(1)}\\ \ddot{u}_i^{(2)}\end{bmatrix}+\frac{E_i A_i}{l_i}\begin{bmatrix}1 & -1\\ -1 & 1\end{bmatrix}\begin{bmatrix}u_i^{(1)}\\ u_i^{(2)}\end{bmatrix}=\begin{bmatrix}f_i^{(1)}\\ f_i^{(2)}\end{bmatrix}+\begin{bmatrix}\beta_i^{(1)}\\ \beta_i^{(2)}\end{bmatrix} \qquad (4.2)$$

where

$$f_i^{(1)} = 1/2\,(m_i-\rho_w A_i)\,g l_i - 1/2\,\rho_w D_i C_{DT}^i l_i\big(1/3(\dot{Z}+\dot{u}_i^{(1)})\big|\dot{Z}+\dot{u}_i^{(1)}\big| + 1/6(\dot{Z}+\dot{u}_i^{(2)})\big|\dot{Z}+\dot{u}_i^{(2)}\big| - 1/12\,(\dot{u}_i^{(1)}-\dot{u}_i^{(2)})\big|\dot{u}_i^{(1)}-\dot{u}_i^{(2)}\big|\big)$$

$$f_i^{(2)} = 1/2\,(m_i-\rho_w A_i)\,g l_i - 1/2\,\rho_w D_i C_{DT}^i l_i\big(1/6(\dot{Z}+\dot{u}_i^{(1)})\big|\dot{Z}+\dot{u}_i^{(1)}\big| + 1/3(\dot{Z}+\dot{u}_i^{(2)})\big|\dot{Z}+\dot{u}_i^{(2)}\big| - 1/12\,(\dot{u}_i^{(1)}-\dot{u}_i^{(2)})\big|\dot{u}_i^{(1)}-\dot{u}_i^{(2)}\big|\big)$$

l_i is the element length, E_i is the effective Young's modulus of the tether, D_i is the diameter of the tether, C_{DT}^i is the tangential drag coefficient, $u_i^{(1)}$ and $u_i^{(2)}$ are the elastic

displacements of the upper and lower nodes, respectively, $\beta_i^{(1)}$ and $\beta_i^{(2)}$ are the boundary conditions for the continuity of strain between nodes of connecting elements at the upper and lower nodes, respectively, and $(\dot{})$ represents a time derivative.

Similar to our continuous model, the vertical motion of the ship is modelled as a prescribed displacement function applied to the upper end (first node) of the tether, $Z = Z^S(t)$. Because the motion of the first node is prescribed, measured (actual) ship motion data can be used as input. Thus, our model can be validated by directly comparing the calculated cage motion and tension in the tether against the actual values for the same ship motion. The equation governing the motion of the cage and ROV is nearly identical to (3.2) but the linear drag is replaced by the more accurate quadratic representation.

The complete model is obtained when the N tether elements are assembled end–to–end and joined at their node points. Nodes are numbered consecutively from the top node, 1, to the bottom node, $N+1$. The second time derivative of the prescribed ship motion is the acceleration of node 1 and the cage and ROV are included by adding their mass to that of node $N+1$ and applying the forces acting on them to that node. The assembled set of differential equations is given in Appendix C. A Runge–Kutta fourth-fifth order numerical integration routine with adaptive step size is used to obtain the temporal response.

4.2 Model Predictions and Results

We used our measurements of the motion and tension of the *ROPOS* ROV system to determine the unknown model coefficients and to verify manufacturer's specifications.

For all measurements, the ROV was out of the cage, and thus, the mass of the ROV, M_{ROV}, and the *in situ* weight of the ROV, W_{ROV}, are set to zero. We determined the weight less buoyancy of the tether, W (per unit length), and cage, W_{CG}, by applying a linear fit to the tension record using depth as the independent variable (Table 2.1). The mass of the tether is approximated by its dry mass plus the mass of the water entrained into the void space between the strands of armour. The mass, M_{CG}, and viscous drag coefficient, C_V^{CG}, of the cage are determined by applying a least squares fit to the tension record using the cage acceleration and velocity as input. Finally, the axial stiffness of the tether, EA, was determined using the speed of strain waves along the tether, c, which was measured when the tether was impulsively loaded during snap loads.

Coefficient	Value
m	3.01 ± 0.06 kg m^{-1}
W	25.4 ± 0.5 N m^{-1}
W_{CG}	$43\,200 \pm 1000$ N
EA	$45.5 \pm 1.4 \times 10^6$ N
C_{DT}	0.02
C_V^{CG}	$8\,150 \pm 170$ kg m^{-1}
M_{CG}	7750 ± 160 kg

Table 4.1: Values of the model coefficients estimated using motion and tension measurements of the ROPOS ROV system.

Different sections of data were used to calibrate and validate the model. We found that our FE model accurately predicts: i) the motion of the cage, ii) the tension in the tether at the ship (Figure C2), and iii) the natural frequencies (Figure C3 and C4). In comparison to the continuous model, the transfer function between the motion of the ship and cage predicted by the FE model is slightly more accurate and agrees better with that calculated from our data (Figure C4).

Although our FE models is accurate, it is not exact and there exists a small (~11%) disagreement between the real and predicted cage motion. The sensitivity analysis indicated that differences between our measured and modelled results cannot be explained by parameter uncertainty. This suggests that there is a significant physical process that is not accurately modelled for oscillatory flow about a body. The differences may be due to the limitations of the concept of a constant drag coefficient and a constant added mass (Simiu and Scanlan 1978 and Sarpkaya and Isaacson 1981). To test this notion, we added a simple wake model that makes some account of the history of motion and the accuracy of the simulated response improved (Figure C4). In particular, the wake model improved the predictions of the larger motions and the real and predicted transfer function between the motion of the ship and cage were nearly identical within the wave–band (Figure C4). For smaller platforms that experience similar vertical motions, such at CTDs, the assumption of a constant drag coefficient and added mass may be less valid because wake will be more developed. Thus, the predicted response of vertically tethered systems should improve if the time varying forcing acting on oscillating packages attached to tethers are more accurately modelled.

Snap loads occurred in less than 1% of the motion cycles in the record we used for validation. Such threshold conditions are very difficult to predict because they require the numerical model to be very precise and our model did not reproduce these snap loads even with the inclusion of the wake model. Therefore, we increased the ship motion by 10% to induce a snap load so we could study the response. Indeed, our model did reproduce the snap loads and all the associated characteristics of the acceleration of the cage and of the tension at the ship (Figure C6). Therefore our discrete model can be used

to investigate the response of vertically tethered systems in extreme seas where existing continuous models are invalid.

4.3 Discussion

Our finite–element lumped–mass model is a useful tool that accurately predicts the response of a caged ROV system to surface excitation and it should be applicable to all vertically tethered system operating in any sea condition. It is also flexible because different systems can be modelled by changing the values of the coefficients without modifying the actual model. Additionally, complex components, such as heave compensation systems, can be added as a specialised element.

Both the continuous and discrete model show that the response of the cage is relatively insensitive to variations in the model coefficients (Figures B7, B8, B9 and C5). This implies that large changes in the model coefficients (and thus, significant physical changes to the real system) are needed to significantly alter the response of the cage to ship motion. However, in many cases, altering the system to fix one operational problem may exacerbate another. For example, increasing the mass and *in situ* weight of the cage, decreases the occurrence of snap loads, but increases the static tension in the tether and rms cage motion. Heave compensation systems provide an alternative because they can change the response of the overboard system without major physical modifications.

Chapter 5

Ship and Cage–Mounted Passive Heave Compensation

In Chapters 2, 3 and 4, we identified several problematic characteristics of the *ROPOS* system which are likely shared with many other vertically tethered systems. In particular, the system is in resonance for much of its operating range, the motion of the ship is amplified at the cage, the motion amplification increases with increasing operating depth (until the first natural frequency begins to move out of the wave–band), and the rapid re–tensioning of slack tether at the cage impulsively loads the tether and jerks the cage. Heave compensation systems would help alleviate these problems and increase the operating envelope of vertically tethered systems. In this chapter we develop a discrete representation of a passive heave compensation system and add it to our finite–element model to investigate the effectiveness of a ship–mounted and a cage–mounted compensation system.

5.1 Heave Compensator Design and Numerical Implentation

Vertically tethered systems can be complex and multifaceted and the addition of a heave compensation system adds additional complexity. We chose a passive design because of its simplicity. However, the load in the tether at the surface increases with increasing operating depth, and thus, the ship–system must be actively adjusted for the variable weight of the overboard system. By contrast, a cage–mounted compensator only supports the weight of the cage and it can be completely passive. To facilitate this passive design, we chose a ram-tensioner design that consists of a pneumatic spring and a viscous damper. Its operation is described in detail in Appendix D.

The tension-displacement curves of the pneumatic spring are determined by modelling its isentropic compression and expansion. A constant volume accumulator is attached to the spring and its volume is determined by specifying the tension range of the compensator. Thus, the non–linear tension–displacement relationship of the compensator is given by:

$$T_{HC} = \frac{W_T(1+k)}{\left(\left(\frac{1+k}{1-k}\right)^{\frac{1}{n}}\left(1-\frac{\delta}{\Delta_T}\right)+\frac{\delta}{\Delta_T}\right)^n} + C_{pd}(\dot{\delta}) \tag{5.1}$$

where W_T is the supported weight less buoyancy, Δ_T is the total compensator travel, k is the range of the tension in the tether (at the compensator) over Δ_T and it is specified as a fraction of W_T, δ is the compensator displacement (line pay out), C_{pd} is the linear damping constant, and n is the ratio of specific heats of the gas (n = 1.4 for air).

The formulation of this discrete–element lumped–mass representation allows a compensation mechanism to be easily incorporated into our model as an additional element inserted at any location. We inserted a compensator element as either the top or bottom element, to represent either a ship–mounted or a cage–mounted compensation system, respectively. The discretized force equations for a pneumatic compensator element are:

$$f_{HC}^{(1)} = \frac{W_T(1+k)}{\left(\left(\frac{1+k}{1-k}\right)^{\frac{1}{n}}\left(1-\frac{z_{i+1}-z_i}{\Delta_T}\right)+\frac{z_{i+1}-z_i}{\Delta_T}\right)^n} + C_{pd}(\dot{z}_{i+1}-\dot{z}_i) \tag{5.2a}$$

and

$$f_{HC}^{(2)} = -f_{HC}^{(1)} \tag{5.2b}$$

where $z_i^{(1)}$ and $z_i^{(2)}$ are the vertical location of the upper, $^{(1)}$, and lower, $^{(2)}$, nodes of the compensator element i, respectively. The mass of the compensator is lumped with the mass of either the cage or the ship, for cage–mounted and ship–mounted configurations, respectively.

5.2 Results

Our FE model is calibrated and validated for the *ROPOS* ROV system, and therefore, it (*ROPOS*) is used as our test case to evaluate the performance of the ship–mounted and cage–mounted compensators. The compensated response was investigated at three different depths (1 000, 2 500 and 5 000 m) for a large range of the total travel of the compensator (Δ_T = 3 to 20 m). The value of k was set to be ± one "average" standard deviation of the tension at the mounting location. For ship–mounting k = 0.2 and for cage–mounting, k = 0.4 (Figure D2). Different values of the damping constant, C_{pd}, were chosen for each mounting location and each value of Δ_T investigated so that the rms motion of cage was minimised at an operating depth of 2 500 m. Because k is constant at each location, the stiffness of the compensators is increased (decreased) by decreasing (increasing) Δ_T.

Addition of the heave compensators affects the dynamic characteristics of tethered system in two ways: 1) the effective stiffness of the system decreases which shifts the natural frequencies to lower values, and 2) the transfer function between the

motion of the ship and cage peaks at a much lower frequency than the first natural frequency and its asymmetry is increased (Figure D8). In the cases investigated, the peak of the transfer function was shifted to the low frequency side of the wave–band. Thus, under normal operating conditions, we found that both the ship–mounted and the cage–mounted compensators reduce the vertical motion of the cage, decrease the rms and peak tension in the tether (Figure D6), and kept the tether taut, thereby eliminating snap loads (Figure D5). For all but the maximum operating depth, 5 000 m, we also found that the effectiveness of the compensators increased with increasing Δ_T. At 5 000 m, the second natural frequency of the cage compensated system was brought closer to and eventually into the wave–band as Δ_T was increased. Thus, the effectiveness of the compensators decreased as the second mode was excited.

It is necessary to prove heave compensation systems do not exacerbate operating problems when sea condition unexpectedly increases above its specified maximum. To simulate storm sea states, we increased the record of ship motion by a factor of two and three. The significant A–frame displacement, S_A, is defined here as the average amplitude of the 25% largest displacements, analogous to the classical definition of significant wave height. The measured displacement of the A–frame used has $S_A = 7.2$ ft (2.2 m), and the records amplified by factors of two and three have $S_A =$ 14.4 ft (4.4 m) and $S_A = 21.7$ ft (6.6 m), respectively. In very rough seas with a significant A–frame displacement of $S_A = 4.4$ m, the uncompensated system experienced many snap loads. The ship and cage compensated systems with $\Delta_T = 5$ m do not experience any snap loads and do not hit their end stops (Figure D10). However, in extreme sea conditions, of

$S_A = 6.6$ m, the tether at the cage goes slack and the piston hits its end stops for both compensator mounting locations (Figure D11). The cage–mounted compensator is compliant so subsequent re–tensioning is gradual and snap loads are not produced. Rapid re–tensioning and snap loads do occur in the ship compensated system although, they are significantly reduced in comparison to those of the uncompensated system. When the compensators (both ship– and cage–mounted) hit their upper end stops, rapid increases in tension, analogous to a snap load, develop, but the spikes in the tension record are smaller than those of the snap loads.

Although the compensators are effective for most of the conditions investigated, we identified two conditions for which the compensated system may have a larger response than the uncompensated system. First, the peak of the transfer function was shifted to the frequency range of swell (fully developed surface ocean waves, 0.05–0.1 Hz), and thus, the systems response to swell will increase. Second, the second natural frequency of the system with the cage–mounted compensator may be brought into the wave–band, exciting the second mode and increasing the rms tension and cause the cage to oscillate out of phase with the ship.

5.3 Discussion

Addition of either a ship–mounted or cage–mounted compensator can improve the operating characteristics of vertically tethered system and significantly increase the range of sea states that are safe. However, when a passive compensation system is added to any vertically tethered system, the characteristics of that compensator must be carefully chosen so that the desired response is achieved over the full operating range.

Additionally, our model can be used to identify operating depths and conditions for which the compensated response will be greater than that of the uncompensated system.

Chapter 6

Conclusions and Future Work

There were three primary objectives of this research. The first was to measure the motion and tether tension of a vertically tethered system and use that data to characterise and understand the dynamic interaction between the support vessel and the undersea platform. The second objective was to develop tools that can help us understand and predict the response to ship excitation. The third objective was to investigate the effectiveness of a ship–mounted and a cage–mounted passive pneumatic heave compensation device at reducing the vertical motion of the undersea platform, decreasing the rms tension in the tether and eliminating snap loads.

The operating problems, such as snap loading and large vertical oscillations of the undersea platform, that plague vertically tethered system were introduced in Chapter 1. Besides making operations troublesome, these problems limit the operating sea state, can damage the tether and instrumentation on the platform and degrade scientific measurements. Understanding the dynamics that cause these problems is difficult because the system is very complex and its response is non–linear. Only a few publications address modelling of vertically tethered systems and their investigations are very specific. No work exists for vertically tethered systems that examines their fundamental dynamic characteristics or rigorously validates their analytical and numerical representations against experimental measurements.

A typical vertically tethered system, a caged deep–sea ROV, was instrumented and data of the motion of the ship and undersea platform and the tension in the tether at

the ship were simultaneously measured using a centralised data acquisition system while the system operated at sea. After processing the data, analysis of the rapid and high resolution measurements yielded the fundamental dynamics of that system. It was found that: i) the system is essentially one–dimensional in the absence of time varying cross–currents and large horizontal excursions of the ship; ii) the first natural frequency is within the wave–band and the system is in resonance for much of its operating range; iii) the platform motion is larger than that of the ship; and iv) the platform response is weakly non–linear. Of particular interest, the characteristics of a snap load are not random as predicted by Huang and Vassalos, (1995). Instead, snap loads are characterised by a regular set of rapid increases in the acceleration of the cage and the tension at the ship which are equally spaced at the travel time of a tensile wave through the tether.

A linearised non–dimensional analytical model of a vertically tethered system and its closed form solution were presented in Chapter 3. The solution is simple in form, yet it is a powerful tool because it is accurate and provides a physical basis for many of the characteristics observed in the measurements (Chapter 2). In particular, the solution provides simple equations that can be used to estimate: i) the natural frequencies, ii) the transfer function between the motion of the ship and cage, and iii) the transfer function between the motion of the ship and the tension in the tether of most vertically tethered systems. Although the solution is only valid for a taut tether, it can predict ship motion that produces slack tether and snap loads. The most notable insight gained arises from the model's simplicity — the dynamic response of vertically tethered system is governed by only two parameters and that response is not very sensitive to changes in those

parameters. In most other vertically tethered system the value of the two coefficients differ by at most a factor of two from the *ROPOS* ROV system, and thus, they will share similar operating characteristics and problems.

The finite–element model presented in Chapter 4 was developed so that it can represent any vertically tethered system and can be reconfigured to model more complex, multi–component systems. Once calibrated using data from the experimental measurements, the discrete representation proved more accurate than the analytic model and it was valid over all sea conditions. However, it did not reproduce the snap loads that occurred in the measurements. Analysis of the small discrepancy between the real and predicted response of the platform showed that the concept of a single drag coefficient and a single added mass coefficient for the platform many not be completely accurate for oscillatory motion. A simple wake model was added to account for the time history of the motion and indeed, it improved the predicted response but still did not reproduce any snap loads. Although the constant coefficient concept yielded reasonable results in the caged ROV model, it is likely that this concept is less accurate (correct) for smaller platforms. By increasing ship motion by 10%, the discrete model with the wake representation accurately reproduced the snap loads that occurred during the measurements and their non–linear characteristics – a regularly spaced series of rapid increases in the acceleration of the cage and tension at the ship. Thus the model is also capable of modelling the transition between slack and taut tether.

A discrete representations of a heave compensator was added to the finite–model in Chapter 5. This representation was easily incorporated into the finite–model because of its generality. Passive ship–mounted and cage–mounted compensators were found to

effectively uncouple ship and cage motion and to increase the range of safe sea states. During extreme seas, the snap loading did not occur for the cage compensated system because the transition between slack and taut was more gradual. Conversely, snap loading did occur with the ship–mounted system but the rate of change of cage acceleration and tension in tether were significantly reduced in comparison to the uncompensated response. When the compensators hit their upper end stops, rapid increases in tension resulted and were larger for the ship compensated system than for the cage compensated system. Although passive compensators can be effective, their stiffness and damping characteristics must be chosen carefully and the response of the compensated system should be investigated over all depths. If the characteristics are improperly chosen, the platform response could increase and exacerbate the operational problems.

6.1 Suggestions for Future Work

The success of my work described in this dissertation encourages future work to expand the range of understanding of tethered systems in general and increase the applicability of my models. In particular, future work should address the following issues and problems:

- During deep operation, horizontal currents may cause the undersea platform to move large horizontal distances with little change in depth. If these currents are time varying or if the ship is being dynamically positioned, the systems may oscillate horizontally which makes navigation and positioning of ROVs difficult, degrades the measurements from horizontal profilers, and makes precision landing of packages on the ocean floor impossible. To investigate these situations, my

models can be extended to include horizontal motions by including rotating reference frames, the normal components of drag acting upon the tether and underwater platform and the horizontal motion variables.

- Once extended to include horizontal motions my model could be used to investigate a much larger range of systems such as towed vehicles, moored buoys, and tension leg platform by simply changing the boundary conditions on the ends of the tether. For example, the bottom boundary condition can be changed to reflect the hydrodynamics of a tow fish.

- The internal forces in a slack tether are not zero and they may exert forces on attached segments or bodies. By including bending and compressive stiffness in my model, these forces may be approximated. This would allow the tether shape to be estimated during compression or low–tension and increase the accuracy of snap load predictions.

- The concept of a constant drag coefficient and a constant added mass is not completely accurate for oscillatory flow. Instead, these coefficients are time varying and the time history of the flow is important. Further work on oscillating bodies may provide a more accurate representation of the hydrodynamic forces.

- Although active compensation system are more complex than passive systems, they may provide better compensation and eliminate the jerks that occur when the piston hits its end stops. In addition, active systems can use software to predict the future ship motion (for example, by linear prediction) and use this information to

optimally move the compensation system. Clearly this could be a fruitful direction for research in control systems.

References

Ablow, C.M. and Schechter, S. 1983. Numerical simulation of undersea cable dynamics. *Ocean Engineering.* **10**, 443–457.

Antoniou, A. 1979. *Digital filters: analysis and design.* McGraw–Hill, New York.

Bennett, P. and Forex, S. 1997, Active heave: the benefits to operations as seen in the north sea, *Proceedings of the SPE/IADC Drilling Conference*, 207-217.

Burnett, D.S. 1987, *Finite element analysis from concepts to applications*. Addison-Wesley Publishing Company, Don Mills, Ontario.

Caughey, T.K. 1963. Equivalent linearization techniques. *Journal of the Acoustic Society of America* **35**, 1706–1711.

Driscoll F.R. and Biggins L. 1993. Passive damping to attenuate snap loading on umbilical cables of remotely operated vehicles. *IEEE Oceanic Engineering Society Newsletter* **28**, 17-22.

Driscoll F.R., Lueck R.G., and Nahon N. 1999a. The motion of a deep–sea remotely operated vehicle system. Part 1: motion observations. *Ocean Engineering*, in press.

Driscoll F.R., Lueck R.G., and Nahon N. 1999b. The motion of a deep–sea remotely operated vehicle system. Part 2: analytic model. *Ocean Engineering*, in press.

Driscoll, F.R., Lueck, R.G., and Nahon, N. 1999c. Development and validation of a lumped–mass dynamics Model of a deep–sea ROV system. Submitted to *Applied Ocean Research.*

Driscoll, F.R., Nahon, N., and Lueck, R.G. 1999d. A comparison of ship–mounted and cage–mounted passive heave compensation systems. Submitted to the *Journal of Offshore and Arctic Engineering*.

Etkin, 1972. *Dynamics of atmospheric flight*. John Wiley & Sons, New York.

Gaddy, D.E. 1997, Ultradeep drillship will react to heave with electric–heave compensating draworks. *Oil & Gas Journal*, July, 68

Garret, J. 1994, Safe operating conditions for the IOS WOCE rosette package, Internal report, Institute of Ocean Sciences, Sidney, British Columbia, Canada.

Grosenbaugh, M.A. 1996. On the dynamics of oceanographic surface moorings. *Ocean Engineering,* **32**, 7–25

Hibbeler, R.C. 1989. *Engineering mechanics – statics and dynamics*. MacMillan Publishing Company, New York.

Hover, F.S. and Yoerger, D.R. 1992. Identification of low–order dynamic models for deeply towed underwater vehicle systems. *International Journal of Offshore and Polar Engineering*, **2**, 38–45.

Hover, F.S., Grosenbaugh, M.A. and Triantafyllou, M.S. 1994. Calculation of dynamic motions and tension in towed underwater cables. *IEEE Journal of Oceanic Engineering*, **19**, 449–457

Huang, S. and Vassalos, D. 1995. Chaotic heave motion of marine cable–body systems. *Proceedings of the ISOPE–Ocean Mining Symposium*, Tsukuba, Japan, 83–90.

ISE 1998, International Submarine Engineering Hysub 5000, 1734 Broadway Street, Port Coquitlam, B.C., Canada, V3C 2M8, web page, http://www.ise.bc.ca/rov.html#hys5000.

Jenkins G.M.and Watts D.G. 1968. *Spectral analysis and its applications*. Holden–Day, San Francisco.

Kirstein, H. 1986, Active heave compensation systems on board vessels and offshore rigs, *Marine Technology*, **17**, 59-61.

Korde, U.A. 1998, Active heave compensation on drill–ships in irregular waves, *Ocean Engineering*, **25**, 541-561.

Logan, D.L. 1992. *A first course in the finite element method*. PWS-KENT Publishing Company, Boston.

Lueck, R. 1999, Personal communications, Centre for Earth and Ocean Research, University of Victoria, B.C., Canada.

Mellem T. 1979. Surface handling of diving bells and submersibles in rough sea. *Proceedings of the Offshore Technology Conference*, Houston, Texas, 1571–1580.

Niedzwecki, J.M. and Thampi, S.K 1988. Heave compensated response of long multi-segment drill strings, *Applied Ocean Research*, **10**, 181-190.

Niedzwecki, J.M. and Thampi, S.K. 1991. Snap loading of marine cable systems. *Applied Ocean Research*, **13**, 210–218.

Rao, S.S. 1990. *Mechanical vibrations*. Addison–Wesley Publishing Company, New York.

Robigou, V. 1993. *Journal of Geophysical Research Letters*, **20**, Cover Page.

Sanders, J.V. 1982. A three–dimensional dynamic analysis of a towed system, *Ocean Engineering*, **9**, 483 – 499.

Sarpkaya, T. and Isaacson, I. 1981, *Mechanics of wave forces on offshore structures*. Van Nostrand Reinhold Company, Toronto.

Shabana, A.A. 1989. *Dynamics of multibody systems*. John Wiley & Sons, New York.

Simiu,E. and Scanlan, R.H. 1978. *Wind effects on structures – an introduction to wind engineering*. John Wiley & Sons, Inc, New York.

Yoerger, D.A., Grosenbaugh, M.A., Triantafyllou, M.S. and Burgess, J.J. 1991. Drag forces and flow–induced vibrations of a long vertical tow cable — part 1: steady–state towing conditions. *Journal of Offshore Mechanics and Arctic Engineering*, **113**, 117-127

Appendix A

The Motion of a Deep–Sea Remotely Operated Vehicle System.

Part 1: Motion Observations

The Motion of a Deep–Sea Remotely Operated Vehicle System. Part 1: Motion Observations

F. R. Driscoll[a,*], R. G. Lueck[b] and M. Nahon[c]

(In press, Ocean Engineering, 1999)

[a] Department of Mechanical Engineering and School of Earth and Ocean Sciences, University of Victoria, Victoria, B.C., V8W 3P6
[b]School of Earth and Ocean Research, University of Victoria, Victoria, B.C., Canada, V8W 3P6
[c]Department of Mechanical Engineering, University of Victoria, Victoria, B.C., Canada, V8W 3P6

Abstract

Rapid and high resolution motion and tension measurements were made of a caged deep–sea ROV system. Simultaneous measurements were made of all six components of motion at the cage and ship A–frame and of the tension in the tether at the ship. Data were collected for cage depths of 0 to 1 765 m. The most significant forcing was in the wave–frequency band (0.1 – 0.25 Hz) and accounted for over 90% of the variance of vertical acceleration. The vertical acceleration of the cage lagged the acceleration of the A–frame by up to 1.9 s and its variance was larger by up to a factor 2.2. For moderate displacements of the A–frame ($\leq$2 m), the system is only weakly non–linear because the harmonics (3rd and 5th) of the vertical acceleration of the cage account for less than 2% of the total variance. The system is essentially one–dimensional because only the vertical motion of the cage and the vertical motion of the A–frame were coherent, while horizontal motions of the cage were weak and incoherent with any component of motion of the A–frame. The natural frequency of the system is 0.22 Hz at 1 730 m, and we estimate that it is within the wave–band for depths between 1 450 m and the full operating depth of 5 000 m.

Large vertical excursions of the A–frame produce momentary slack in the tether near the cage. Retensioning results in snap loads with vertical accelerations of 0.5 gravity. Large rates of change of tension and vertical acceleration first occur at the cage during its downward motion and propagate to the surface with the characteristic speed (3 870 m s^{-1}) of tensile waves for the tether. Six echoes are clearly

* Corresponding author.

detectable at both ends of the tether, and their pattern is extremely repeatable in different snap loads. Due to misalignment of the tether termination with the centres of mass and buoyancy, the cage pitches by up 14° during a snap. The resulting small radius of curvature poses the greatest stress on the tether.

Keywords: *Tethered marine systems, remotely operated vehicles, ROV, tether, snap loading, cable dynamics, motion and tension measurements.*

---

1. Introduction

Caged remotely operated vehicles (ROVs) are vital tools that provide safe and effective access to deep water the world over. ROV systems have many applications, including scientific exploration of deep ocean phenomena; assembly, inspection and repair of undersea structures; and dangerous military operations. However, operation of these systems is usually restricted to calm conditions because slack cable and large snap loads can occur during rough seas. Operation during rough seas can cause structural damage to the tether (umbilical cable) and its internal electrical and optical conductors that reduces the life of the tether and endangers the recovery of the ROV.

Increasing the tether life and maximising the safe operating range of ROV systems is not an easy task. Fig. 1 shows a typical caged ROV system where the ship and undersea unit are connected by a long elastic structural member — the tether. Capable of sustaining only tensile loading and having length–dependent properties, the tether is a complex dynamic system in itself. The cage adds an additional level of complexity because of its non–linear dynamic characteristics. An accurate numerical model should

be very useful to predict unsafe sea conditions and can identify changes necessary to improve system operation.

The focus in modelling tethered underwater vehicles has been on towed systems (see Ablow and Schechter, 1983; Hover and Yoerger, 1992; Hover, Grosenbaugh and Triantafyllou, 1994; and Chapman, 1984), and only a few authors have addressed vertically–tethered systems (Niedzwecki and Thampi, 1991; Driscoll and Biggins, 1993; and Huang and Vassalos, 1995). In these works, discrete approximation methods are used for modeling the complex non–linear dynamics of these undersea vehicle systems. However, we did not find any work comparing the motion and tension in a model of a vertically tethered system against real data in our literature review. Validation against real motion and tension measurements is essential in proving the reliability of these models as an effective tool. Validation data was found for deep sea ocean moorings (Grosenbaugh, 1996), as well as motion and tension measurements for a diving bell operating near the surface and in the air–sea interface (Mellem, 1979). The lack of available data for vertically–tethered systems and the need to validate our finite–element lumped–mass model led to an extensive field test in which we measured the motion and tension of a caged ROV system.

In this paper, we present the motion and tension in the tether of a caged ROV system operating at sea. We provide a detailed overview of the ROV system and instrumentation used. Signal processing that converts the data into a useful form for our analysis is presented. We expand a technique that combines different measurements into a single enhanced signal. While the model validation is not directly addressed in this

paper, this data nevertheless provides many insights into the dynamic characteristics of the caged ROV system. In particular, the system is weakly non–linear, the vertical cage motion is larger than that of the ship, and the system is not operating far from its natural frequency. Additionally, several snap loads were recorded that provide novel insights into some mechanisms leading to premature tether failure. Lastly, the data supports the assumption that the dominant motion occurs in the vertical direction and that a one–dimensional model should be sufficient to predict the motion of the cage. It is shown in Part II of this paper that the transfer function (both magnitude and phase) between ship and cage motion and the natural frequency and harmonics can be accurately predicted by a continuous one–dimensional model.

2. ROV System and Instrumentation

2.1 ROPOS remotely operated vehicle system

Motion data were collected for the *ROPOS* (Remotely Operated Platform for Oceanographic Science) deep sea ROV system (an International submarine Engineering Hysub 5000, ISE 1998) while it was operating over the Juan de Fuca Ridge, approximately 200 km off the coast of British Columbia, Canada. *ROPOS* is a caged ROV system capable of diving to 5 000 m, which weighs 26 700 N in air and has dimensions of 1.45 m × 2.6 m × 1.7 m (WLH). A 300 m retractable tether attaches the ROV to the cage (garage), where it can reside during deployment and recovery. The cage is essentially a large weight that keeps the underwater system directly below the ship and contains many of the electronic systems and power supplies needed by the ROV. The cage weighs 49 000 N in air and has dimensions of 2.1 m × 3.4 m × 4.2 m (WLH). The

tether connecting the ship and cage has three layers of steel armour surrounding a core of electrical and optical conductors. The tether is 3 cm in diameter, 4 200 m long, weighs 30.5 Nm^{-1}, has a maximum working load and breaking strength of 200 000 N and 550 000 N, respectively. The support vessel used is the arctic survey vessel *CSS John P. Tully* which is 69 m long with a beam of 14 m.

2.2 Instrumentation

We wanted to measure the motion of the tether at the ship, the motion of the cage and the tension in the tether. Thus, two sites were instrumented: the top of the ship's A–frame (directly above the sheave that supports the tether) and the top of the ROV cage. The accelerations and rotation rates were measured using tri–axial, orthogonal accelerometers and rate gyros at each location. Corresponding accelerometers and rate gyros axes were closely aligned. A pressure sensor was used to measure the cage depth and its rate of change. A load cell in the axle of the sheave was used to measure tension in the tether at the A–frame. Thermometers were located in each gyro sensor and the cage accelerometers to allow temperature correction of the signals, though the actual corrections proved to be small and of no practical consequence.

Signals from the accelerometers, rate gyros and load cell were low–pass filtered and sampled at 256 Hz to a resolution of 16 bits. Eight–pole elliptic low–pass filters with a cutoff at 100 Hz were used to suppress aliasing. Temperature, pressure and its analog derivative were sampled at 32 Hz to a resolution of 16 bits (Table 1).

The data were sampled sequentially from both sites by a single computer aboard the ship. The data were acquired by the software/hardware Ocean Data Acquisition System, ODAS (Fig. 2), developed at the University of Victoria. ODAS was chosen because of its ability to rapidly interrogate sensors that are widely distributed, with a pattern and temporal co–ordination determined by a central computer. The sampling jitter is negligible (less than 10^{-7} s) and the samples from the remote cage and the ship A–frame are completely synchronised. Sampling commands and data were communicated serially from the ship–board computer to the remote sites using shielded and twisted wire pairs for the A–frame and a pair of fibre optic conductors for the cage. Thus, it is possible to relate the instantaneous motions of the A–frame to those of the cage even though these two sites are separated by up to 1 765 m (the maximum operating depth for the cruise discussed here).

3. Signal Processing

3.1 Reference Frames

Three independent reference frames are used in the data processing: an inertial (earth fixed) frame, $\boldsymbol{I}$; and two instrumentation body–fixed frames, one attached to the cage, $\boldsymbol{B}^C$, and one attached to the ship, $\boldsymbol{B}^S$. The inertial reference frame $(X \quad Y \quad Z)$ has its origin at the mean sea surface. X and Y are perpendicular horizontal directions and Z points down and is aligned with gravity. At the cage, the instrument frame $\boldsymbol{B}^C$ has directions $(x^C \quad y^C \quad z^C)$ pointing from stern to bow, starboard to port, and top to bottom, respectively. The origin is in the pressure case at the top of the cage. The ROV

exits from the front (bow) of the cage, in the positive x^C–direction. The ship reference frame $\boldsymbol{B}^S$ $\left(x^S \quad y^S \quad z^S\right)$ is defined similarly and has its origin at the top of the A–frame. The axes of the accelerometers and rate gyros are aligned with the instrument frames.

3.2 Euler angle transformation of accelerometers

The ship and cage reference frames are independent and rotate differently; thus, the signals in each need to be transformed into a fixed, common frame of reference for comparison. The inertial frame is a convenient choice and allows easy removal of the gravitational signal in the accelerometers. Premultiplying the accelerometer records by the rotation matrix $\boldsymbol{L}_{IB}$ transforms the data into the inertial frame. $\boldsymbol{L}_{IB}$ is constructed using three consecutive Euler angle rotations about the z, y and x axes, in that order. The rotation angles are defined as: ψ –yaw about z; θ –pitch about y; and ϕ –roll about x (Etkin Chapter 4, 1972).

$$\boldsymbol{A}' = \boldsymbol{L}_{IB}\boldsymbol{a}' \tag{1}$$

$$\boldsymbol{L}_{IB} = \begin{bmatrix} c\psi c\theta & c\psi s\theta s\phi - s\psi c\phi & c\psi s\theta c\phi + s\psi s\phi \\ s\psi c\theta & s\psi s\theta s\phi + c\psi c\phi & s\psi s\theta c\phi - c\psi s\phi \\ -s\theta & c\theta s\phi & c\phi c\theta \end{bmatrix} \quad \boldsymbol{A}' = \begin{bmatrix} A_x' \\ A_y' \\ A_z' \end{bmatrix} \quad \boldsymbol{a}' = \begin{bmatrix} a_x' \\ a_y' \\ a_z' \end{bmatrix}$$

$$s\cdot = \sin(\cdot) \quad c\cdot = \cos(\cdot)$$

where $\boldsymbol{A}'$ and $\boldsymbol{a}'$ are the acceleration vectors (including gravitational acceleration) expressed in the inertial and instrumentation reference frames.

3.3 Accelerometer Integration

Accelerometers measure force per unit mass along their axis of sensitivity. Thus, if an accelerometer measures along an axis that is not perpendicular to gravity, it will report inertial acceleration as well as the component of gravity. Because the instrumentation frames rotate around all three axes of I with respect to gravity, the acceleration measurements are "contaminated" by gravitational acceleration. After transforming the accelerometer signals from the instrumentation frame to the inertial frame, the "contamination" only appears in the vertical component as a constant offset that is easily removed by subtraction.

$$A = L_{IB}a' - g \qquad g = [0,0,g]^T$$

where A is the translational acceleration vector in the inertial reference frame and g is the gravitational acceleration.

Motion measurements at the top end of the tether and at the cage centre of gravity were required. The ship board accelerometers were mounted very close to the sheave and provided the former. However, the cage mounted accelerometers were located a distance from the cage centre of gravity. The accelerations of the centre of gravity of the cage, therefore, had to be calculated using:

$$A^{COG} = A^{MP} - L_{IB}\left(\Lambda \times r^{MP} + \omega \times \left(\omega \times r^{MP}\right)\right) \tag{2}$$

where A^{COG} and A^{MP} are the cage accelerations at the centre of gravity and at the sensor mounting point respectively; $r^{MP} = \begin{bmatrix} r_x^{MP} & r_y^{MP} & r_z^{MP} \end{bmatrix}^T$ is the position vector from the cage centre of gravity to the sensor mounting point, expressed in B^C; and $\omega = \begin{bmatrix} \omega_x & \omega_y & \omega_z \end{bmatrix}^T$ and $\Lambda = \begin{bmatrix} \Lambda_x & \Lambda_y & \Lambda_z \end{bmatrix}^T$ are the vectors of angular velocities and angular accelerations, expressed in B^C.

The vertical velocity of the ship and cage, in the inertial frame, were calculated by integrating the inertial acceleration records. The accelerations of the ship and cage were first high–pass filtered, to remove bias, and integrated by convolving the resulting signal with a first–order low–pass Butterworth filter (Antoniou Chapter 5, 1979). The resulting velocity records of the ship and cage were integrated using the same technique to calculate the position.

3.4 Pressure Record Enhancement

A pressure sensor attached to the cage provided an accurate measure of depth. However, the range of the pressure signal was 5 000 m and since the digitization was limited to 16 bits; the digital resolution was very coarse. The analog derivative of the pressure signal was also recorded and had a much smaller range, thus preserving the high resolution of the pressure signal. Combining the pressure and pressure derivative records (Mudge and Lueck, 1994), the resolution of the signal was increased from 0.15 to 0.02 m. This is equivalent to using a 19 bit A/D converter. For operation at a nominally stationary depth, the acceleration at the location of the pressure sensor was calculated using (2). The two cage vertical position records, one from the integration of the acceleration records

and one from the pressure record were overlaid and were nearly identical. For a 2 000 s record with vertical motions of 0.86 m rms, the difference between the position signals was less than 0.04 m rms, which is close to the resolution of the pressure signal and mostly due to the wider bandwidth of the acceleration record.

3.5 Euler angle calculation

The Euler angles, $\beta = [\phi \quad \theta \quad \psi]^T$ were not directly measured. They were instead synthesised from a combination of the accelerometer and rate gyro measurements. At very low frequencies ($f < 0.1$ Hz), the inertial accelerations are very small and the gravitational acceleration g dominates the accelerometer output, thus:

$$(\boldsymbol{a}')_L \cong \boldsymbol{L}_{BI}\boldsymbol{g} \tag{3}$$

where $(\boldsymbol{a}')_L$ is the low–frequency component of the acceleration vector and $\boldsymbol{L}_{BI} = \boldsymbol{L}_{IB}^T$. After low–pass filtering $\boldsymbol{a}'$, a low–frequency estimate of roll, ϕ_L and pitch, θ_L is provided by solving the first and second components of (3) for:

$$\theta_L = \sin^{-1}\left(\frac{-a_x'}{g}\right) \tag{4a}$$

$$\phi_L = \sin^{-1}\left(\frac{a_y'}{g\cos(\theta_L)}\right) \tag{4b}$$

This technique cannot yield a low–frequency yaw estimate.

Higher frequency information about the roll and pitch is provided by the gyros in terms of rotation rates. The time derivatives of the Euler angles were found according to (Etkin Chapter 4, 1972):

$$\dot{\beta} = T_B \omega \tag{5}$$

$$T_B = \begin{bmatrix} 1 & \sin(\phi)\tan(\theta) & \cos(\phi)\tan(\theta) \\ 0 & \cos(\phi) & -\sin(\phi) \\ 0 & \sin(\phi)\sec(\theta) & \cos(\phi)\sec(\theta) \end{bmatrix} \qquad \dot{\beta} = \begin{bmatrix} \dot{\phi} \\ \dot{\theta} \\ \dot{\psi} \end{bmatrix}$$

The estimate of T_B requires *a priori* knowledge of the roll and pitch angles, but these are known only for low frequencies (from the accelerometers). Therefore, an iterative method is used to accurately calculate Euler rates (Fig. 3). In the first iteration, T_B is calculated using ϕ_L and θ_L, and the resulting Euler rates are used to calculate the Euler angles. In subsequent iterations, T_B is recalculated using roll and pitch angles from the previous iteration. Using this method, the roll and pitch rates converge to 0.01% of their final value after three iterations.

Direct integration of the Euler rates should yield the Euler angles. However, the Euler rates are subject to slight error in the form of an offset (bias), causing the integrated signal to drift. High–pass filtering can reduce the drift, but also eliminates all information with frequencies less than the filter cut–off. The pre–emphasized (Mudge and Lueck, 1994) roll $\phi_E(t)$ (pitch $\theta_E(t)$) was obtained by combining the low–frequency roll ϕ_L (pitch θ_L) with the roll rate $\dot{\phi}$ (pitch rate $\dot{\theta}$):

$$\phi_E = \phi_L + \frac{1}{\Omega_C}\dot{\phi}; \qquad \theta_E = \theta_L + \frac{1}{\Omega_C}\dot{\theta} \tag{6}$$

where Ω_C is a filter cut off frequency (explained next). The pre–emphasised roll and pitch (ϕ_E, θ_E) contain low–frequency information from the accelerometers (ϕ_L, θ_L) and high–frequency information from the gyros $(\dot{\phi}, \dot{\theta})$. The roll and pitch signals are recovered for all frequencies by low–pass filtering (deconvolving) the pre–emphasised signals with a single–pole low–pass with a cut–off at Ω_C (Mudge and Lueck, 1994). Using this technique, information is preserved at all frequencies and the resulting signals are drift free. Measurements that contain low–frequency yaw information, such as compass heading, were not available, and therefore we could not apply a similar procedure to the yaw rate. Instead, the yaw rate was high–pass filtered and directly integrated to yield the yaw angle. Therefore, the relative bearing between the ship and cage is unknown, but this is not essential in our analysis.

4. Motion Observations

Motion and tension measurements were made during five dives (Table 2), which include periods of deployment (descent to bottom), recovery (ascent to ship) and near bottom operation. The ascents and descents were interrupted at a variety of depths for approximately 5 minutes to provide stationary data (Table 3). Data were collected for up to 3.5 hours when the cage was at its terminal depth for scientific operations of the ROV (typically 1 730 m). The maximum depth was 1 765 m. Sea conditions were moderately rough and the sheave experienced typical vertical displacements of 2 m, peak–to–peak. Several intervals of relatively calm and rough sea conditions occurred with sheave

displacements less than 1 m and greater than 4 m, respectively. The ship was station keeping with the bow pointing into the waves during all operations and cross–currents were typically less than 0.3 ms^{-1}. Wave direction was steady and small adjustments in position were made using ship thrusters.

The scope of this section is limited to measurements of the system operating at nominally constant depths. A total of 13 140 s of data were recorded while the system operated at 1 730 m, which we denote as the terminal depth. This is the largest data record for stationary operation and constitutes 57% of the stationary data. We present this data along with some examples from shallower depths.

For the terminal depth, spectra of the horizontal and vertical accelerations of the ship and cage were calculated using a 5 000 s record (Fig. 4). The integral of a signal spectrum over all frequencies up to the Nyquist frequency yields the signal variance:

$$\overline{X^2} = \int_0^{f_N} C_X \mathrm{d}f$$

where C_X is the auto–spectrum of some signal X; f is the frequency and f_N is the Nyquist frequency (half the sample frequency). Spectra were calculated by averaging the periodograms of data segments 64 s long and overlapped by 50% (Press, et al Chapter 13, 1992). This method increased the statistical certainty of the spectra. For frequencies above 32 Hz at this depth, there is negligible cage acceleration and the ship and cage accelerations are incoherent. Therefore, in Fig. 4, we restrict the upper limit of the frequency axis to 32 Hz. Spectra of the acceleration of the ship peak between 0.1 and 0.2 Hz and decrease rapidly to a minimum at 1.4 Hz. Above 1.4 Hz, there are bands of

significant variance and these have been attributed to vibrations of the A–frame. The spectral gap at 1.4 Hz exists for all conditions and is not particular to operation at the terminal depth (1 730 m). We use this gap to separate the wave–induced motions from high–frequency excitations and will refer to these two regions as the wave–frequency and high–frequency bands, respectively. Spectra of the acceleration of the cage also peak between 0.1 and 0.2 Hz but there is no clear spectral gap.

4.1 Wave–frequency motion observations

Within the wave–frequency band, we restrict analyses to the frequency range containing 90% of the variance of the vertical ship acceleration that extends from 0.1 to 0.25 Hz and denote this range as the wave–band. Of the remaining variance, 5% is at lower frequencies and 5% is at higher frequencies. The motion records of the ship and cage were high–pass filtered with a cut–off at 0.1 Hz and are summarised in Table 4. The motions of the ship and cage are primarily vertical and the vertical motion of the cage is larger than that of the ship. For example, the variances of the horizontal accelerations of the ship (A_X^S and A_Y^S) are smaller than the variance of vertical acceleration (A_Z^S) by factors of 17 and 5.3, respectively. For the cage, the variances of horizontal accelerations (A_X^C and A_Y^C) are smaller than the variance of vertical acceleration (A_Z^C) by factors of 136 and 296, respectively. The ratio of vertical–to–horizontal cage variance is $O(10^2)$ at all depths from 0–1 765 m. The variance of the vertical cage acceleration exceeds that of the ship by a factor 2.19. The ratio of vertical cage–to–ship acceleration variance decreases with decreasing depth, but remains larger than unity at all depths. For example,

at 975 meters the amplitude ratio is 1.53. The large peak–to–peak pitch motions in Table 4 occur during snap loads which are addressed later.

The spectra of the cage acceleration also peak between 0.1 and 0.25 Hz. The vertical acceleration peaks at 0.15 Hz and its third and fifth harmonics are evident at 0.44 and 0.73 Hz in Fig. 4(b). The cage is a bluff body, subject to quadratic drag, and thus, can only produce spectral variance at odd harmonics of the fundamental frequency of excitation. A measure of the non–linearity of the system is provided by the relative strength of these wave–frequency harmonics. The variance below 0.3 Hz accounts for 98.3% of the total variance, while the subsequent harmonics only contribute 1.3 and 0.1%, respectively. Therefore, the vertical cage acceleration is weakly non–linear within the range of our measurements. For these measurements, the application of linear system theory (coherency, cross–spectra, transfer–functions, etc.) is justified. However, the drag is a quadratic function of cage velocity, and for higher sea–states, the non–linear response will become important.

Time series of vertical ship and cage motions are very similar and the larger cage peak–to–peak motion is evident when the signals are overlaid. A 150 s section is shown in Fig. 5. The cage motion is larger than the ship motion and therefore implies the system is operating near a resonant frequency and it is lightly damped within the range of motions recorded. Knowledge of the resonant frequencies is crucial to the design of a ROV system. Either the resonance frequency must be kept outside of the range of operation, or the system must be built strong enough to survive operation at, or near, this

frequency. The propagation time that the ship motion takes to reach the cage can clearly be seen in the lag between ship and cage motions.

A measure of the motion amplification between the ship and cage is provided by the transfer function estimate (TFE). For two related signals, the transfer function is estimated using:

$$H_{XY} = \frac{C_{XY}}{C_{XX}} \tag{7}$$

where C_{XY} is the cross–spectrum of the signals X (the input) and Y (the output), and C_{XX} is the auto–spectrum of X. The magnitude of the TFE between the vertical ship and cage motion, $\left|H_{Z^S Z^C}\right|$ changes with frequency (Fig. 6). At 0 Hz, $\left|H_{Z^S Z^C}\right|$ is approximately unity and increases through the wave–band to a maximum of 1.68 at 0.2 Hz. The vertical motion records are very close to Gaussian; therefore, we use the parametric estimates of statistical uncertainty as given by Jenkins and Watts (1968, Chapter 3) to yield the 95% confidence interval (given by the vertical error bars in Fig. 6). Only statistically coherent data are plotted. For shallower operating depths, the peak of $\left|H_{Z^S Z^C}\right|$ moves to higher frequencies (Fig. 7).

At wave frequencies, the cage heave lags the ship heave. The time lag is a measure of the propagation time of motion along the tether from the ship to the cage and is defined as:

$$\tau = -\frac{\partial \gamma}{\partial \omega} \tag{8}$$

where γ is the phase between the ship and cage motion and ω is the angular frequency. The phase changes non–linearly with frequency (Fig. 6(b)) and therefore, the lag evident in the time series (Fig. 5) is frequency dependent. We calculated the time–lag by first fitting a 5^{th} order polynomial to the frequency in a least squares sense, using the phase as the independent variable, and then numerically differentiating the phase with respect to the calculated frequency. The lag increases rapidly through the wave–band to a maximum of 1.93 s at 0.23 Hz. Within the wave–band, the lag varies between 0.71 s and 1.93 s and can be up to 50% of the motion period. Thus, the time histories of ship and cage motion will not be identical. Instead, the various spectral components of the motion of the ship will be phase shifted at different rates as they propagate down the tether. Therefore, in order to produce an accurate temporal record of cage motion, any dynamic model of a deep sea ROV system must include a mechanism for modelling the lag. At shallower depths, such at 975 m, lag decreases and the maximum lag is shifted to higher frequencies (Fig. 7). The lag reaches a maximum of 1.43 s at 0.33 Hz.

4.2 System natural frequency and harmonics

The cage is connected to the ship by an elastic member, the umbilical cable, and thus has a natural frequency, f_1, and associated harmonics. If f_1, or one of the harmonics, occur in (or not far from) a frequency band containing significant ship motion, the system will be in (or not far from) resonance and the ship motion may be amplified at the cage. This occurrence could lead to very large cage motions, making

vehicle docking difficult and snap loads likely. Thus, knowing the natural frequency and the harmonics is very important for predicting safe operating conditions. In any continuous system, f_1 is the frequency at which the phase between forcing and response first passes through 90°. Using the transfer function estimate (Fig. 6), f_1 is 0.22 Hz at 1 730 m. Although f_1 is not evident in the spectra of vertical cage acceleration (Fig. 4(b)), the harmonics can be clearly seen at higher frequencies. The second and third harmonics occur at 1.17 and 2.25 Hz. The harmonic frequencies of the system are not integer multiples of f_1. At shallower depths, f_1 is higher and equals 0.35 Hz at 975 meters.

At 1 730 m, the system is in resonance because f_1 is within the wave–band. To estimate the depth range for which f_1 is within the wave–band, we fitted a 3rd order polynomial to the depth, using the measured natural frequency as input and extrapolated to find that the natural frequency will be within the wave–band from 1 450 m to the maximum operating depth of 5 000 m. In all stationary measurements, $|H_{z^s z^c}|$ peaks at a slightly lower frequency than f_1 and it decreases much more rapidly on the high–frequency side of f_1 than on the low–frequency side. Because of this asymmetry, more motion is transferred from the ship to the cage at frequencies less than f_1 than at frequencies above f_1. In addition, $|H_{z^s z^c}|$ is greater than one at its peak. Much of the variance of the ship motion in the wave–band is contained within a narrow band centred at 0.16 Hz, and as a result, much of that motion is transferred to and amplified at the cage when f_1 is greater than 0.16 Hz. Assuming $|H_{z^s z^c}|$ is also asymmetric at depths greater than 1 765 m, much less motion will be transferred between the ship and cage when f_1 is

less than 0.16 Hz. We estimate that f_1 coincides with the spectral peak of ship acceleration (0.16 Hz) at 2 940 m.

4.3 High–frequency motion observations

In the high–frequency band (f > 1.4 Hz), the system is excited by broad–band ship vibration and narrow–band cage vibration which are small in magnitude and do not significantly excite the cage. Consequently, the transfer function estimate suffers from large uncertainty and is not presented for the high–frequency band. However, snap loads do provide significant excitation in the high–frequency band and we discuss the associated transfer function in the following section.

4.4 Snap Loads

Snap loads cause structural damage to the tether and its internal electrical and optical components. Additionally, large vertical cage displacement, cage pitching, and excitation of system harmonics occurred during snap loads in the ROPOS ROV system. Thus, an understanding of snap loads and the ensuing cage motion is essential to the development of counter–measures that increase tether life, reduce undesirable cage motion, and possibly eliminate snap loads. In our literature search, we were not able to find any measurements of snap loads for a deep–sea ROV system. Here, we present an overview of the motion and tension measurement for several snap loads recorded when the system was operating at the terminal depth (1 730 m).

For a typical snap load, the tether tension, vertical ship and cage motions, and the cage pitch are shown in Fig. 8. The motion of the system during a snap load is different

from that during normal operation. Most notably, the cage experiences a large pitch and the A–frame "rings". As well, the motion exhibits non–linear characteristics such as a nearly discontinuous vertical cage acceleration. Using 16 s records of 8 snap loads, the variance and maximum deviations for these measurements were calculated (Table 5). During a snap load, the variances of the vertical acceleration of ship and cage and the pitch of the cage were larger than their variances during typical operation by factors of 5.8, 3.21 and 13, respectively. Other motions (e.g. roll, yaw, etc) were only slightly affected by snap loads and remained within their normal range (Table 4).

All snap loads are characterised by a series of jerks: rapid increases in the vertical acceleration. These jerks typically begin when the ship and cage are near the bottom of their motion cycle and continue for at least one wave period. A jerk typically lasts for 0.15 s, during which, the cage may accelerate by up to 5 ms^{-2}. Rapid increases in tether tension cause the cage jerks. In Fig. 9, the acceleration records of 8 snap loads are overlaid. Clearly, the jerks are not random, but occur at regular intervals, common to all snap loads at the same operating depth. A measure of a jerk is often defined as the time derivative of the acceleration (Hibbeler, 1989, Chapter 12). In Fig. 10 (a), the jerk records for the same 8 snap loads are overlaid and are remarkably similar. The cage jerks have corresponding rapid increases in tether tension (measured at the surface) that lag in time (Fig. 8). The mass of the ship is much larger than that of the cage and therefore, the acceleration of the ship is only minimally affected by a snap load. The rapid increases in tension are emphasised by taking the first time derivative of the tension records corresponding to the 8 snap loads. Again, we see that all 8 records are remarkably similar (Fig. 10(b)). Thus, we ensemble averaged the records of the derivatives of jerk and

tension and overlaid the resulting two records in Fig. 11. The spacing of the jerks is nearly constant and is 0.92, 0.89 and 0.87 s between the first and second, second and third, and third and fourth jerks respectively. The peaks of the first derivative of the tension are located midway between the peaks of the jerks. The second jerk and first peak of the tension derivative are the strongest with later maxima decreasing monotonically. The first jerk precedes the first maxima of the tension derivative which shows that strain wave originates at the cage, propagates along the tether and is reflected when it reaches the ship or cage. On average, the strain wave takes 0.445 s to travel the length of the tether (1 730 m).

The kinematics of the first jerk can be explained from video observation made during the operation of the vehicle. Using ROV–cameras, the tether was observed to bow out above its cage termination prior to the first evidence of a snap load at the surface (a large vibration of the A–frame and ship deck) (Shepherd, 1997).

The maximum tension for a snap load was larger by a factor of up to 2.1 than that for the prior motion cycle and 65 000 N (14 600 lbs) greater than the static tension of 82 700 N (18 500 lbs). However, for several snap loads, the maximum tension was less than that for the prior motion cycle. For operation at the terminal depth (1 730 m), the tension never exceeded the maximum recommended working load of 200 000 N (45 000 lbs), and therefore, the associated axial strain is unlikely to damage the tether. However, the static tension increases with depth, and the additional tension from a snap load may exceed the rating of the tether. For example, at 5 000 m, the static tension is

165 000 N (37 000 lbs). If the snap load is similar to that found at 1 730 m depth, then the total tension will exceed the maximum recommended load.

The centre of weight and buoyancy of the cage are horizontally offset at a zero pitch angle, and for this reason, they apply a torque to the cage, causing it to pitch entrance down. The tether termination at the cage is also horizontally offset from the centre of weight, and applies a torque causing the cage to pitch entrance up. Statically, the torques balance when the cage is pitched 7° nose up. For typical operation, the pitch deviates by 0.97° rms. However, when the tether tension goes to zero during a snap load, peak–to–peak pitching can exceed 14° (Table 5). During our measurements, nothing restricted the bending radius of the tether at the cage termination. The tether bowed out prior to a snap load and when the tether is subsequently retensioned, the bending radius at the termination was much smaller than the minimum recommended by the manufacturer. Hence, each snap load may create small fractures in the optical conductors, which attenuate the optical signal and lead to premature optical failure at the termination. This is a common occurrence with ROPOS. With this insight, we later placed a bend restrictor at the cage termination, limiting tether bending so that it is never less than the recommended minimum.

Using the 8 records of snap loads, 16 s long, we calculated the spectra of the vertical cage accelerations and their respective coherency and transfer function estimates (Fig. 12). The vertical cage jerks are impulsive and excite the natural frequency and harmonics of the system. Variance of the vertical cage acceleration increased by a factor of 19 over its value during normal operation. At the natural frequency, second harmonic,

and third harmonic, the transfer function estimate exceeds 100, 10, and 3 respectively, and it is between 1 and 2 at higher frequencies. The ship and cage are typically in phase or 180° out of phase for $f > 1$ Hz. These phase characteristics are consistent with that of an elastic system. However, the changes in phase do not occur at the natural frequency or the harmonics. The effects of snap loads at deeper operation are not clear, but will surely exacerbate the undesirable motions and tether damage outlined in this section.

Excitation of the harmonics is also seen in the high–frequency oscillation of the acceleration record of the A–frame (Fig. 8). The scale of the high–frequency vertical cage motion is much smaller than at wave frequencies and is not clearly visible in Fig. 8. Thus, we high–pass filtered the vertical cage acceleration and position records to isolate the high–frequency motion imparted during a snap load (Fig. 13). The high–frequency motion decays slowly which indicates that the system is highly under–damped at these frequencies and velocity amplitudes.

5. Wave Frequency Motion Relationships

Development of efficient and accurate dynamic models requires *a prior* knowledge of what motion variables are important and must be included in the model. In this section, we use spectral techniques to identify (*i*) the ship motion variables that are important in forcing the system, (*ii*) the cage motion variables that respond coherently and (*iii*) the significance of the response. Motion measurements were made of all 6 degrees of freedom at the ship and cage; 3 translational accelerations, and 3 rates of rotation. Each of these measurements corresponds to a unique motion variable. We will identify relationships between any two variables (motion variable pairs) of the set of 12

motion variables. The local (ship–ship and cage–cage) motion variable pairs provide information on the intra–dependence of ship and cage motions. These local motion variable pairs are used to identify variables that contain redundant or insignificant information and are not needed to model the ROV system. The inter–dependent pairs (ship–cage) provide information on the response of each cage motion variable to the forcing applied by each ship motion variable. These inter–dependent pairs are used to identify ship and cage motion variables that are related and significant in forcing and response.

In the wave–frequency band, the only clear relationship between motion variables is evident between the vertical motions variables. All other motion variables appear inharmonious in time and any relationship between them is difficult to see (Fig. 14). Similarly, there is no relationship evident in the time domain between pairs of rotation rates. To clarify the relationships between motion of the ship and cage, we estimate the average coherency among all combinations of linear and angular acceleration variables in the wave–band (0.1 to 0.25 Hz) at the terminal operating depth (Fig. 15). The average coherency coefficient, $\langle \Gamma_{XY}^2 \rangle$, is estimated using:

$$\langle \Gamma_{XY}^2 \rangle = \frac{|\langle C_{XY} \rangle|^2}{\langle C_{XX} \rangle \langle C_{YY} \rangle} \tag{9}$$

where the angled braces represent an average over the wave–band (Jenkins and Watts chapter 9, 1968). Fig. 15 is divided into 4 equal quadrants. The upper left quadrant presents the intra–coherency of ship motions, the lower right quadrant presents the intra–

coherency between cage motions and the lower left quadrant presents the inter–coherency between the ship and cage motions. The information is symmetric about the diagonal and thus, the upper triangle is left blank for clarity. Any variable pair having coherency greater than 0.4 is significant and there are five significant ship–cage motion pairs: $A_Z^S - A_Z^C$, $\Lambda_Y^S - A_Z^C$, $\Lambda_X^S - A_Z^C$, $A_Z^S - A_X^C$, and $\Lambda_Y^S - A_X^C$ (Table 6).

Three ship motion variables, A_Z^S, Λ_X^S, and Λ_Y^S are related to A_Z^C (Table 6). We will now show that Λ_X^S and Λ_Y^S are redundant and can be eliminated because much of the acceleration of the A–frame is due to the roll and pitch accelerations of the ship about a point of minimal vertical acceleration (2). For this reason, A_Z^S is 41% and 76% coherent with Λ_X^S and Λ_Y^S, respectively. The vertical acceleration of the ship measured at the A–frame is, (the angular velocity terms are small and omitted):

$$A_Z^S = A_Z^{S-CR} + \Lambda_X^S R_Y^{CR-MP} - \Lambda_Y^S R_X^{CR-MP} \tag{10}$$

where A_Z^{S-CR} is the vertical ship acceleration at the centre of rotation; and $\boldsymbol{R}_B^{CR-MP} = [R_X^{CR-MP} \quad R_Y^{CR-MP} \quad R_Z^{CR-MP}]^T$ is the position vector from the point of minimal vertical acceleration to the instrumentation mounting point. All vector components are expressed in the inertial frame. The part of A_Z^S due to the angular accelerations is therefore:

$$A_R = \Lambda_X^S R_Y^{CR-MP} - \Lambda_Y^S R_X^{CR-MP} \tag{11}$$

Solving (11) for R_X^{CR-MP} and R_Y^{CR-MP} in the frequency domain gives:

$$R_Y^{CR-MP}\left(1-\Gamma^2_{\Lambda_X^S \Lambda_Y^S}\right)=\frac{C_{\Lambda_X^S A_R}}{C_{\Lambda_X^S}}-\frac{C_{\Lambda_Y^S A_R} C_{\Lambda_X^S \Lambda_Y^S}}{C_{\Lambda_X^S} C_{\Lambda_Y^S}} \tag{12a}$$

$$R_X^{CR-MP}\left(1-\Gamma^2_{\Lambda_X^S \Lambda_Y^S}\right)=\frac{C_{\Lambda_X^S A_R} C_{\Lambda_X^S \Lambda_Y^S}}{C_{\Lambda_X^S} C_{\Lambda_Y^S}}-\frac{C_{\Lambda_Y^S A_R}}{C_{\Lambda_Y^S}} \tag{12b}$$

Applying the average of (12a) and (12b) over the wave–band to the data from 1 730 m, we find that the ship predominantly pitches about an axis located 30 m ahead of the accelerometers on the A–frame. Using the same development for A_Y^S, we find that the ship rolls about an axis located 15 m below the accelerometers. These axes intersect near the nominal centre of gravity of the ship. Using this intersection as the ship's predominant centre of rotation, Λ_X^S and Λ_Y^S account for 90% of the variance of the A_Z^S, while only 10% is due to heave. Thus, we conclude that A_Z^S already includes all the effects of Λ_X^S and Λ_Y^S, making redundant an explicit consideration of the variable pairs $\Lambda_X^S - A_Z^C$ and $\Lambda_Y^S - A_Z^C$.

Both the ship motion variables A_Z^S and Λ_Y^S are related to A_X^C. Again, Λ_Y^S is redundant because its effect is included in A_Z^S. We will now show that we can reject the relationship pair $A_Z^S - A_X^C$ as negligible in comparison to $A_Z^S - A_Z^C$. Statically, the cage pitch is 7° (entrance up) and therefore, the outer surfaces are inclined with respect to the vertical axis. When moved vertically, the inclined surfaces cause water to flow asymmetrically around the cage which forces the cage sideways. Thus, the X–acceleration of the cage is directly related to its vertical motion, explaining the 76% coherency between A_Z^C and A_X^C (Fig. 15) and the 63% coherency between A_Z^S and A_X^C.

We introduce the relative coherent variance (the magnitude squared of the transfer function averaged over the wave–band), a measure of variance transferred between related variables, to compare the variance transferred between variable pairs. The relative coherent variance between signals X (the input) and Y (the output) is:

$$\left\langle |H_{XY}|^2 \right\rangle = \left\langle \Gamma_{XY}^2 \right\rangle \frac{\langle C_{YY} \rangle}{\langle C_{XX} \rangle}$$

Between A_Z^C and A_X^C, the relative coherent variance is only 0.01 and it is even smaller between A_Z^S and A_X^C. For comparison, the relative coherent variance between $A_Z^S - A_Z^C$ is 1.95. Therefore, we declare the relationship pair $A_Z^S - A_X^C$ as negligible.

Neither measurement system carried a compass, and therefore we do not have a measure of the absolute orientation of the ship and cage in the horizontal plane. We did measure the rate of rotation about the vertical axis and integrated it to obtain the angular position around the vertical axis. However, the integration ignored frequencies below 0.025 Hz to suppress the bias in the rate measurement. The ship orientation was nearly steady for $f < 0.025$ Hz due to the active station keeping. Therefore, the horizontal orientation of the ship and cage in the inertial frame are each unknown by a constant of integration, and the two frames could be in relative rotation at frequencies below 0.025 Hz. Hence, the individual components of acceleration in the horizontal plane cannot be compared directly. However, the horizontal acceleration can be compared by combining the X and Y components into a vector or complex time series ($A_H = A_X + jA_Y$) which is composed of a counter–clockwise rotating component (positive frequencies) and

a clockwise component (negative frequencies) (Mooers, 1973). In the wave–band, the horizontal acceleration of the ship and cage were 15% (10%) coherent and had a relative coherent variance of 0.0059 (0.0035) for clockwise (counter–clockwise) rotations. These low values can be attributed to the hydrodynamic damping of the horizontal motion of the tether and to the large ($\approx$ 1:1000) horizontal–to–vertical aspect ratio of the position vector connecting the ship and cage. As a result, the relative coherent variance between horizontal acceleration of the ship and cage are small in comparison to that of the vertical accelerations and therefore, can be neglected for modelling purposes.

The variance of the vertical acceleration of the cage is 2.19 times greater than the vertical acceleration of the ship and the signals are 89% coherent with a relative coherent variance of 1.95. Clearly, A_Z^S and A_Z^C are more closely related than any other non–redundant variable pair and have the largest relative coherent variance. Therefore, the only significant relationship in the wave–band is between the vertical motion variables (of the ship and cage) and a one–dimensional model should be sufficient to predict cage motion due to ship forcing.

6. Discussion

Knowing the natural frequency of an ROV system is essential to identify ships with compatible motion characteristics and to predict the safe operating conditions at the desired depth of operation. The natural frequency of the ROV decreases with increasing operating depth and is 0.35 Hz at 975 m and 0.22 Hz at 1 730 m. The forcing is predominately in the wave–band (0.1–0.25 Hz). Within the depth range of our measurements, the vertical cage motion was larger than that of the ship and the cage–to–

ship motion ratio increased with depth. These measurements are consistent with a system being forced at frequencies equal to or not far from its natural frequency. The fact that the ship–to–cage amplitude ratio increases with depth is also consistent with the natural frequency moving towards the wave–band. We estimate that the natural frequency will be within the wave–band for the depth range 1 450 to 5 000 m. Because of the asymmetry of the transfer function about the natural frequency, we predict the greatest amplification of cage motion will be for depths between 1 450 and 2 940 m where f_1 is higher than the peak of the wave–band ($0.16 \leq f_1 \leq 0.25$ Hz). Considering these characteristics, it is not surprising that snap loads and large vertical cage displacements were common at the terminal operating depth (1 730 m). One large displacement during a docking attempt sheared the tether connecting the cage and ROV. Luckily, the ROV was positively buoyant and so eventually floated to the surface.

The lag is an important factor characterising the relationship between ship and cage motions. For example, in dynamic models of ROV systems, the lag must be included to accurately predict time histories of cage motion. Within the wave–band, the lag changes non–linearly with frequency and the frequency corresponding to the maximum lag decreases with depth. This lag–frequency relationship results because the phase is a function of the elastic, inertial and drag properties of the entire system. At 1 730 m, the maximum lag is 0.91 s. However, all strain waves resulting from the snap loads consistently take 0.445 s to propagate the length of the tether with very little dispersion of the frequency content. The propagation speed is equal to the longitudinal speed of sound in the tether, approximately 3 870 ms^{-1}.

We initially thought that snap loads damage the tether and its internal electrical and optical conductors. However, the magnitudes of the tension spikes are smaller than initially thought, and the maximum tension recorded at the sheave, 145 500 N (32 600 lbs), never exceeded the manufacturer's recommended limit of 200 000 N (45 000 lbs). Was the tension at the cage larger than the maximum recommended by the manufacturer? At the cage, the static tension is 40 500 N (9000 lbs), half of that at the ship. Assuming that the magnitudes of the tension spikes at the cage, less the mean tension, are similar to those measured at the sheave, the manufacturer's recommended limit was also never exceeded at the cage. Thus, it is unlikely that the strain induced by tension caused any structural or internal damage to the tether. However, tether damage occurs regularly with ROPOS and most likely results from the bending of the tether at the cage termination when the tether bows while it is slack and when the cage pitches during retensioning. Using the ROV cameras, the tether was observed to bow significantly prior to the snap load. During the subsequent retensioning, the cage pitched from 4 to –12° (Fig. 8). Thus, with the tether under tension, a tight bend formed in the tether as the cage pitched and was likely much less than the minimum bending radius recommended by the tether manufacturer. Tight bending of this type causes fractures to form in the fibre optic communication lines and stresses the steel armour. With this knowledge, we understand why tether damage only occurs in a short section (< 2 m) at the cage termination. For example, near the end of the experiment, the fibre optic lines failed, and a 2 m section of tether at the cage termination was removed. The tether was reterminated, and communication was re–established with the cage. Frequent retermination may have prevented fatigue failure of the armour (and the loss of the cage and ROV).

Snap loads may also impact the components of the cage. The jerks (resulting from the snap loads) were rapid and large in magnitude, both shocking and vibrating the cage. During several jerks, the cage acceleration was up to half of gravity, and it rapidly oscillated with an amplitude of up to 5 cm peak–to–peak at its second harmonic frequency (1.17 Hz). Under these conditions, electronic and mechanical components can be shaken free and structural damage may occur from the large and rapid changes in acceleration. Although the tension spikes did not damage the tether directly, the resulting motions are very destructive and thus, snap loads need to be eliminated to reduce damage to the cage.

The initial purpose of our experiment was to obtain data for validating our existing one–dimensional dynamic numerical model of the ROV. The analysis of the data has outlined many motion characteristics that can be used to validate our model and justify our one–dimensional assumption. In particular, the only significant relationship between the ship and cage motion is in the vertical direction. Only the vertical motions need to be included in a model and the remaining 5 degrees of freedom need not be modelled. Thus, a one–dimensional dynamic model should be sufficient to accurately reproduce these measurements.

The striking characteristics of the ROV system provide challenging tests for numerical models. Realistic models should reproduce: (*i*) the non–linear transfer function between ship and cage motions (both magnitude and phase), (*ii*) the natural frequency and harmonics, and (*iii*) the regular pattern of cage acceleration and tether tension during a snap load.

7. Conclusions

We have made the first rapid and high resolution measurements of a caged deep sea ROV system which consists of a support ship, winch, umbilical tether, cage and ROV. In this investigation, the ROV and cage were vertically suspended below the support ship by a compliant umbilical tether. We simultaneously measured all six components of motion of the ship (at the A–frame) and of the cage and the tension in tether. By combining the low–frequency portion of the accelerometer records with the high–frequency part of the rates of rotation, we determined drift free roll and pitch records and the true inertial accelerations.

Over 90% of the variance of the vertical acceleration of the ship was in the wave–band (0.1 to 0.25 Hz) and this component of acceleration was the only significant forcing on the system. We found that the vertical motion of the cage exceeded that of the ship and that it was weakly non–linear for all depths (0–1 765 m). The cage motion lagged the ship motion by up to 1.9 s at 1 730 m and the natural frequency of the system was within the wave–band for depths greater than 1 450 m. The phase of the transfer function between ship and cage motion decreased non–linearly with frequency. The magnitude of the transfer function was greater than one near the peak frequency and was asymmetric with respect to the natural frequency. As a consequence of this asymmetry, much more ship motion is transferred to the cage at frequencies below, than above, the natural frequency. We estimate that the dangerous operating range is between 1 450 and 2 940 m where most of the ship motion will be transferred to and amplified at the cage.

At 1 730 m, the system was in resonance and subject to snap loads. Prior to each snap load, momentary slack developed in the tether at the cage. Rapid retensioning jerks the cage and produces a localised strain in the tether directly above the cage. A strain wave then propagates along the tether at 3 870 ms^{-1} (the characteristic speed of sound in the tether) and is reflected at the ship and cage. A regular pattern of spikes in cage acceleration/tension in the tether results and is repeated in 8 different snap loads. The temporal spacing of the spikes is determined by the travel time of the strain wave. The tension spikes did not exceed the tether's maximum working load (recommended by the manufacturer) but the acceleration spikes at the cage were as large as half of gravity. The cage also pitched by up to 14° which caused a tight bend in the tether at the cage termination and damaged the fibres housed within the tether.

We applied spectral techniques to determine that only in the vertical direction was there significant forcing (by the ship) and response (by the cage). Thus, a one–dimensional model should be sufficient to represent this ROV system and reproduce the characteristics of the real system.

Acknowledgements

The authors gratefully thank John Garrett, Kim Juniper, Steve Scott, Keith Shepherd, Bob Holland and the Captain and crew of the *CSS John P. Tully* operated by the Institute of Ocean Sciences in Sidney, B.C. Canada for graciously providing access to the ROPOS ROV system and berthing during the experiment. Additionally, we would like to thank Jim McFarlane and the staff of International Submarine Engineering (ISE) for their continual support and assistance in this project. F.R. Driscoll was financially

supported by scholarships from the Natural Science and Engineering Research Council (NSERC), the Science Council of British Columbia (SCBC) and ISE. This work was partially supported by the US Office of Naval Research under contract N00014–93–1–0362 and NSERC .

References

Ablow, C.M. and Schechter, S. 1983. Numerical simulation of undersea cable dynamics. *Ocean Engineering.* **10**, 443–457.

Antoniou, A. 1979. *Digital filters: analysis and design.* McGraw–Hill, New York.

Chapman D.A. 1984. Towed cable behaviours during ship turning maneuvers. *Ocean Engineering.* **11**, 327–361

Driscoll F.R. and Biggins L. 1993. Passive damping to attenuate snap loading on umbilical cables of remotely operated vehicles. *IEEE Oceanic Engineering Society Newsletter* **28**, 17-22.

Etkin, 1972. *Dynamics of atmospheric flight.* John Wiley & Sons, New York.

Grosenbaugh, M.A. 1996. On the dynamics of oceanographic surface moorings. *Ocean Engineering.* **32**, 7–25

Hibbeler, R.C. 1989. *Engineering mechanics – statics and dynamics.* MacMillan Publishing Company, New York.

Hover, F.S., Grosenbaugh, M.A. and Triantafyllou, M.S. 1994. Calculation of dynamic motions and tension in towed underwater cables. *IEEE Journal of Oceanic Engineering.* **19**, 449–457

Hover, F.S. and Yoerger, D.R. 1992. Identification of low–order dynamic models for deeply towed underwater vehicle systems. *International Journal of Offshore and Polar Engineering.* **2**, 38–45.

Huang, S. and Vassalos, D. 1995. Chaotic heave motion of marine cable–body systems. *Proceedings of the ISOPE–Ocean Mining Symposium*, Tsukuba, Japan. 83–90.

ISE 1998, International Submarine Engineering Hysub 5000, 1734 Broadway Street, Port Coquitlam, B.C., Canada, V3C 2M8, web page, http://www.ise.bc.ca/rov.html#hys5000.

Jenkins G.M.and Watts D.G. 1968. *Spectral analysis and its applications*. Holden–Day, San Francisco.

Mellem T. 1979. Surface handling of diving bells and submersibles in rough sea. *Proceedings of the Offshore Technology Conference*, Houston, Texas. 1571–1580.

Mooers, C.N.K. 1973. A technique of the cross spectrum analysis of pairs of complex–valued time series with emphasis on properties of polarized components and rotational invariants. *Deep–Sea Research.* 20, 1129–1141.

Mudge, T.D. and Lueck, R.G. 1994. Digital signal processing to enhance oceanographic observations. *Journal of Atmospheric and Oceanic Technology*. **11**, 825–836.

Niedzwecki, J.M. and Thampi, S.K. 1991. Snap loading of marine cable systems. *Applied Ocean Research*. **13**, 210–218.

Press,W.H., Teukolsky, S.A., Vetterling, W.T. and Flannery, B.P. 1992. *Numerical recipes in C, second edition*. Cambridge University Press, Cambridge.

Shepherd, K. 1997. Personal communication, Institute of Ocean Sciences, Department of Fisheries and Oceans, Sidney, B.C., Canada.

Table 1. Description of the instrumentation used to measure the motion of the ship and cage and the tension in the umbilical tether.

Instrument	Range	Resolution
Accelerometer	± 8 g	0.00024 g
Rate Gyro (Ship)	± 100 $°s^{-1}$	0.0031 $°s^{-1}$
Rate Gyro (Cage)	± 50 $°s^{-1}$	0.0015 $°s^{-1}$
Load Cell	0 – 267 500 N (0 – 60 000 lbs)	8.2 N (1.8 lbs)
Pressure Sensor (Pressure)	5 000 m	0.15 m
Pressure Sensor (Pressure Derivative)	± 25 ms^{-1}	0.0008 ms^{-1}

Table 2. Overview of the data

Dive		Depth (m)	Record Length (s)
1	Descent	50 – 1735	7 500
	At Bottom	1 740	940
2	Descent	100 – 190	460
	Ascent	300 – 80	940
3	Descent	44 – 1 736	6 030
	At Bottom	1 730	890
	Ascent	1 720 – 90	8 320
4	At Bottom	1 765	5 320
5	Descent	530 – 1 738	4 000
	At Bottom	1 730	13 140

Table 3. List of the depth and duration of the motion records for stationary operation, excluding records for operation at the terminal depth.

Depth (meters)	Record Time (sec)
233	320
488	320
631	460
778	320
975	620
1 133	360
1 378	360

Table 4. Summary of the motions for a 5 000 s record of the system operating near 1 730 m.

	Variance	Maximum Peak–to–peak		Variance	Maximum (absolute)
X^S	0.0096 m^2	0.65 m	A_X^S	0.0133 m^2s^{-4}	0.90 ms^{-2}
Y^S	0.0698 m^2	2.74 m	A_Y^S	0.0436 m^2s^{-4}	0.99 ms^{-2}
Z^S	0.328 m^2	3.79 m	A_Z^S	0.230 m^2s^{-4}	2.42 ms^{-2}
ϕ^S	0.275 $(°)^2$	6.79 °	$\ddot{\phi}^S$	0.170 $(°s^{-2})^2$	2.25 $°s^{-2}$
θ^S	0.930 $(°)^2$	6.34 °	$\ddot{\theta}^S$	0.700 $(°s^{-2})^2$	3.21 $°s^{-2}$
ψ^S	0.0924 $(°)^2$	2.45 °	$\ddot{\psi}^S$	0.0855 $(°s^{-2})^2$	1.39 $°s^{-2}$
X^C	0.0035 m^2	0.57 m	A_X^C	0.0037 m^2s^{-4}	1.11 ms^{-2}
Y^C	0.0003 m^2	0.18 m	A_Y^C	0.0017 m^2s^{-4}	1.19 ms^{-2}
Z^C	0.686 m^2	5.34 m	A_Z^C	0.502 m^2s^{-4}	4.17 ms^{-2}
ϕ^S	0.0427 $(°)^2$	3.01 °	$\ddot{\psi}^C$	0.844 $(°s^{-2})^2$	7.9 $°s^{-2}$
θ^C	0.560 $(°)^2$	14.86 °	$\ddot{\theta}^C$	4.66 $(°s^{-2})^2$	31.87 $°s^{-2}$
ψ^C	0.215 $(°)^2$	10.48 °	$\ddot{\psi}^C$	0.588 $(°s^{-2})^2$	9.57 $°s^{-2}$

Table 5. Summary of the large motions recorded during 8 snap loads.

	Variance	Maximum Peak–to–peak		Variance	Maximum (absolute)
Z^S	0.943 m^2	4.34 m	A_Z^S	1.26 m^2s^{-4}	4.64 ms^{-2}
Z^C	1.98 m^2	5.81 m	A_Z^C	1.47 m^2s^{-4}	5.17 ms^{-2}
θ^C	9.02 $(°)^2$	14.2 °	$\ddot{\theta}^C$	58.7 $(°s^{-2})^2$	45.4 $°s^{-2}$
	Variance	Maximum Peak–to–peak		Maximum	
Tension	1.13×10^6 N^2	0.116×10^5 N		0.146×10^5 N	

Table 6. Coherency and relative coherent variance between ship–cage variable pairs.

	$\langle \Gamma^2_{XY} \rangle$	$\langle H_{XY} \rangle$
$A^S_Z - A^C_Z$	89 %	1.95
$\Lambda^S_Y - A^C_Z$	76 %	-
$\Lambda^S_X - A^C_Z$	41 %	-
$A^S_Z - A^C_X$	63 %	0.014
$\Lambda^S_Y - A^C_X$	52 %	-

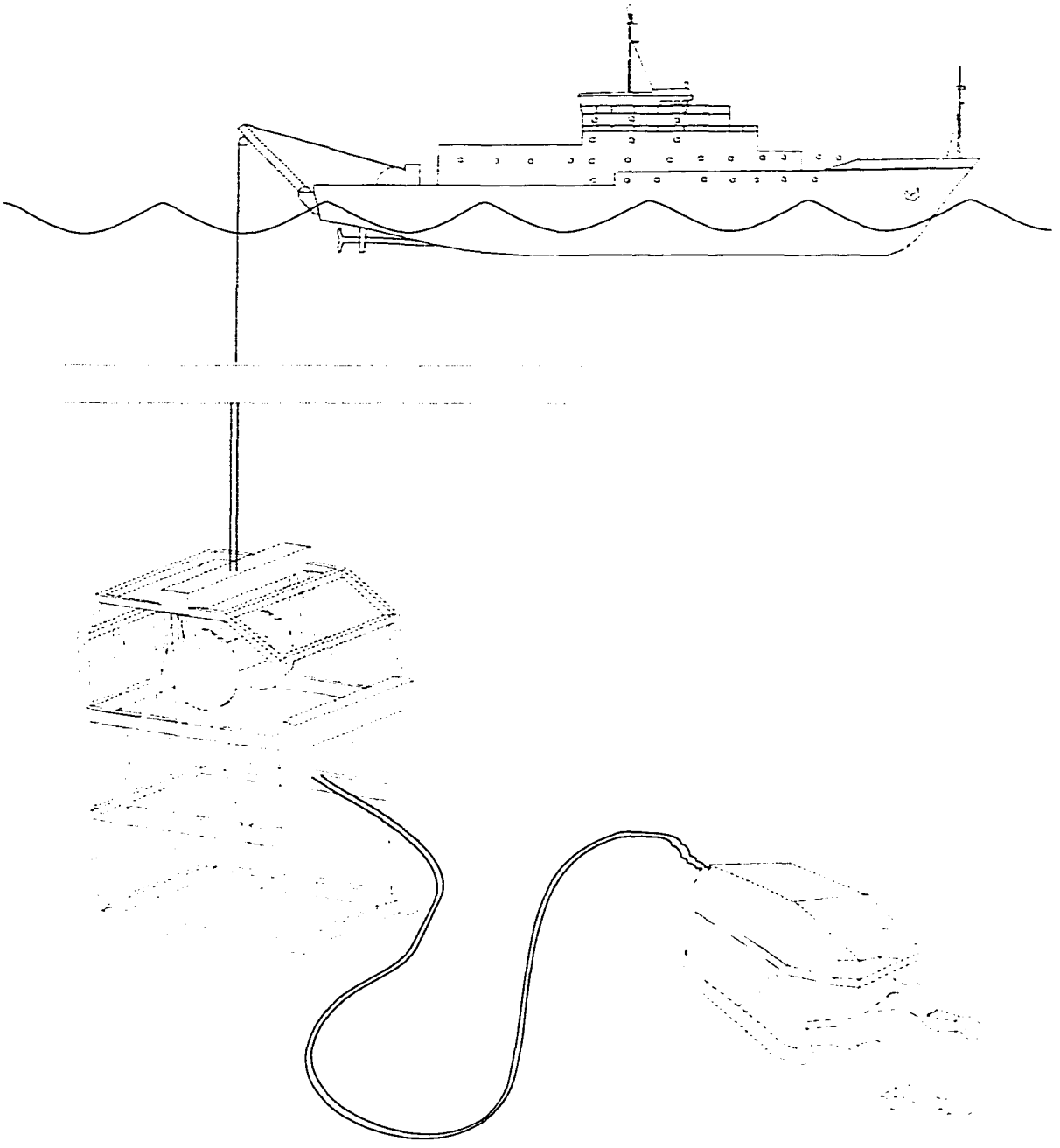

Fig. 1. Diagrammatic representation of a typical deep sea ROV system consisting of a support ship, winch, umbilical tether, cage and vehicle.

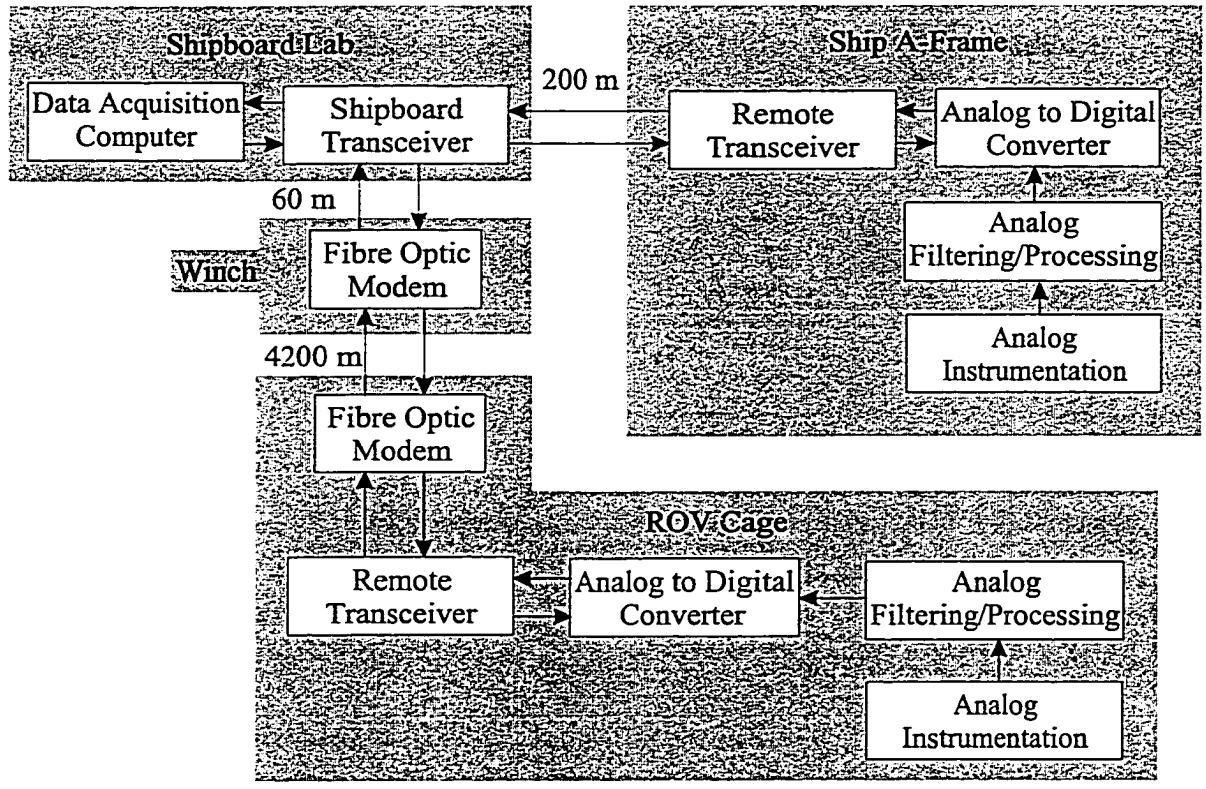

Fig. 2. Conceptual diagram of the Ocean Data Acquisition System used to measure the motions of a deep sea ROV system. The arrows represent the flow of instructions to, and data from, the instruments. Each white block represents a group of components performing a specific task (measuring, processing, transmission etc.).

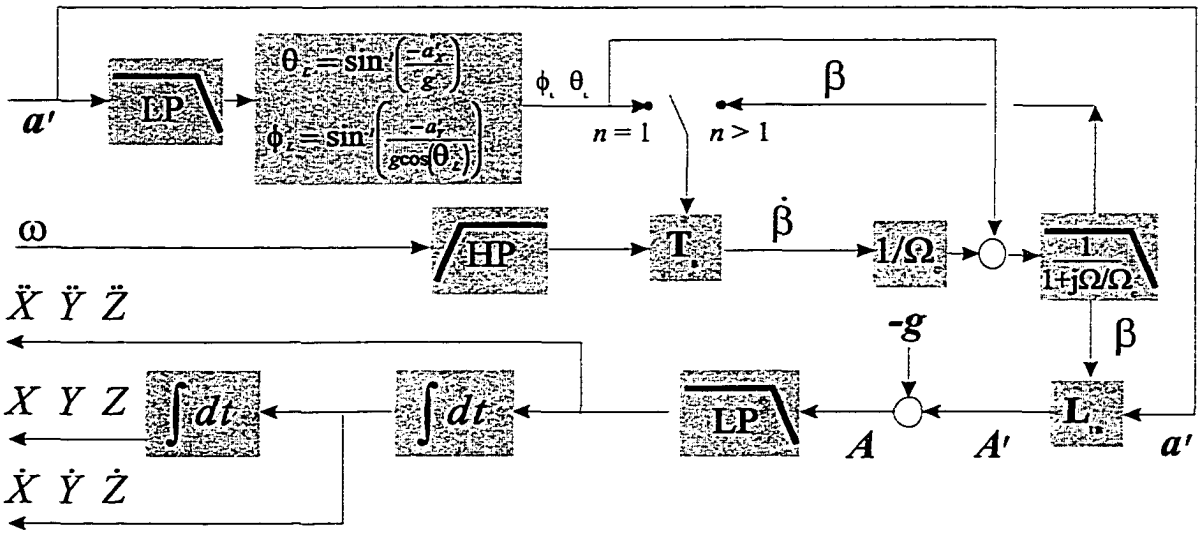

Fig. 3. Flow chart of the processing of the tri–axial accelerometer signals. The signals are first transformed from the instrumentation body–fixed frame to the inertial frame using an Euler angle transformation. The Euler angles are solved iteratively. The gravitational "contamination" of the acceleration signals is removed and the resulting signals are integrated to yield velocity and position.

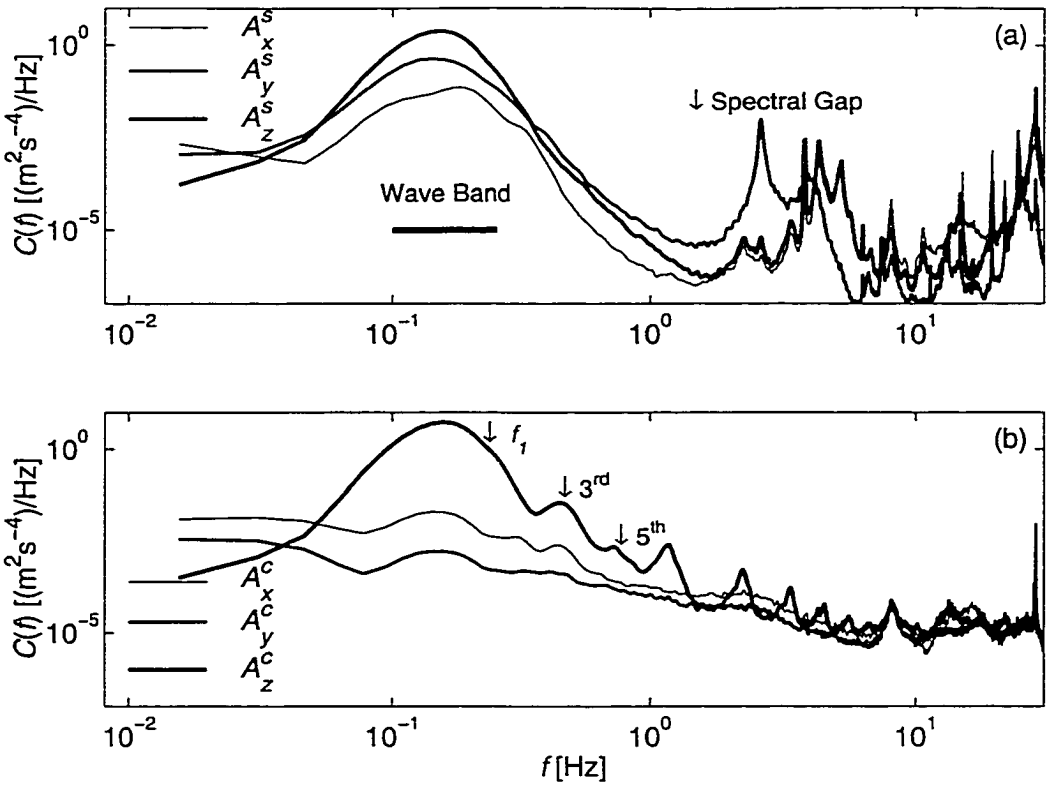

Fig. 4. Spectra of the inertial acceleration records of the ship (a) and cage (b) at a depth of 1 730 m. The wave–band (horizontal bar in (a)) contains 95% of the variance of vertical ship acceleration. The arrows are the spectral gap (a), the 3rd and 5th harmonic of the peak cage motion (b) and the natural frequency (f_1) (b).

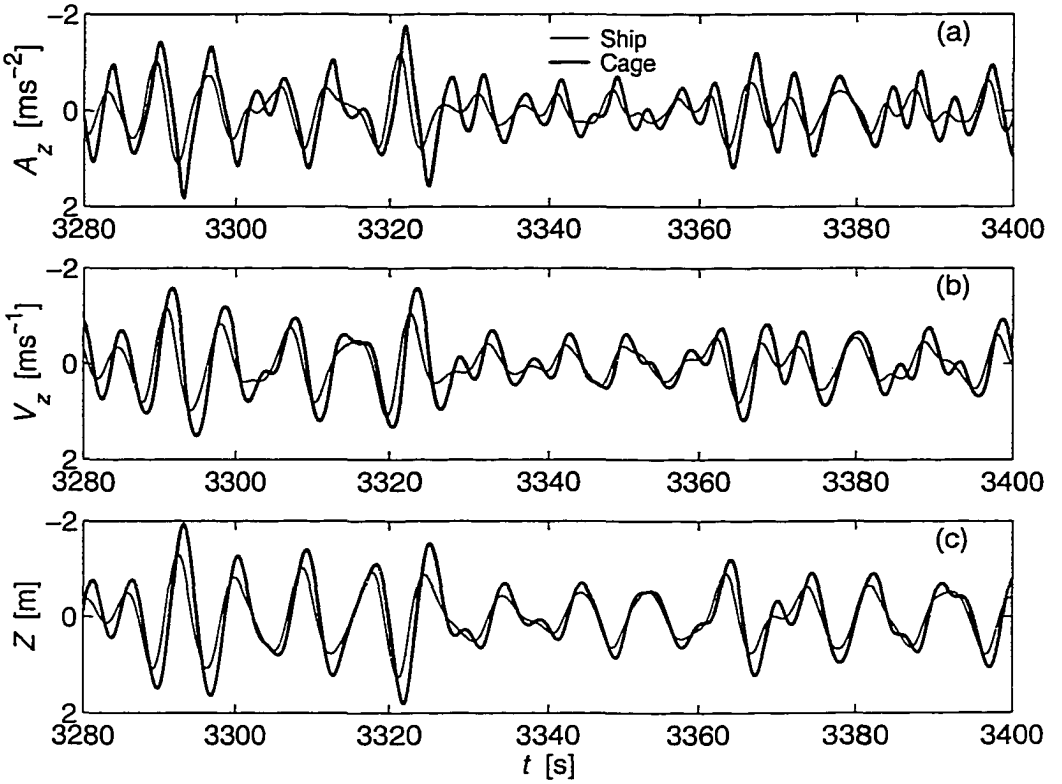

Fig. 5. Vertical acceleration (a), velocity (b), and position(c) of the ship and cage at 1 730 m. The motion records at the two locations are very similar and the cage motions are larger and lag those of the ship. To make viewing of the figure more intuitive, the y–axes have been flipped.

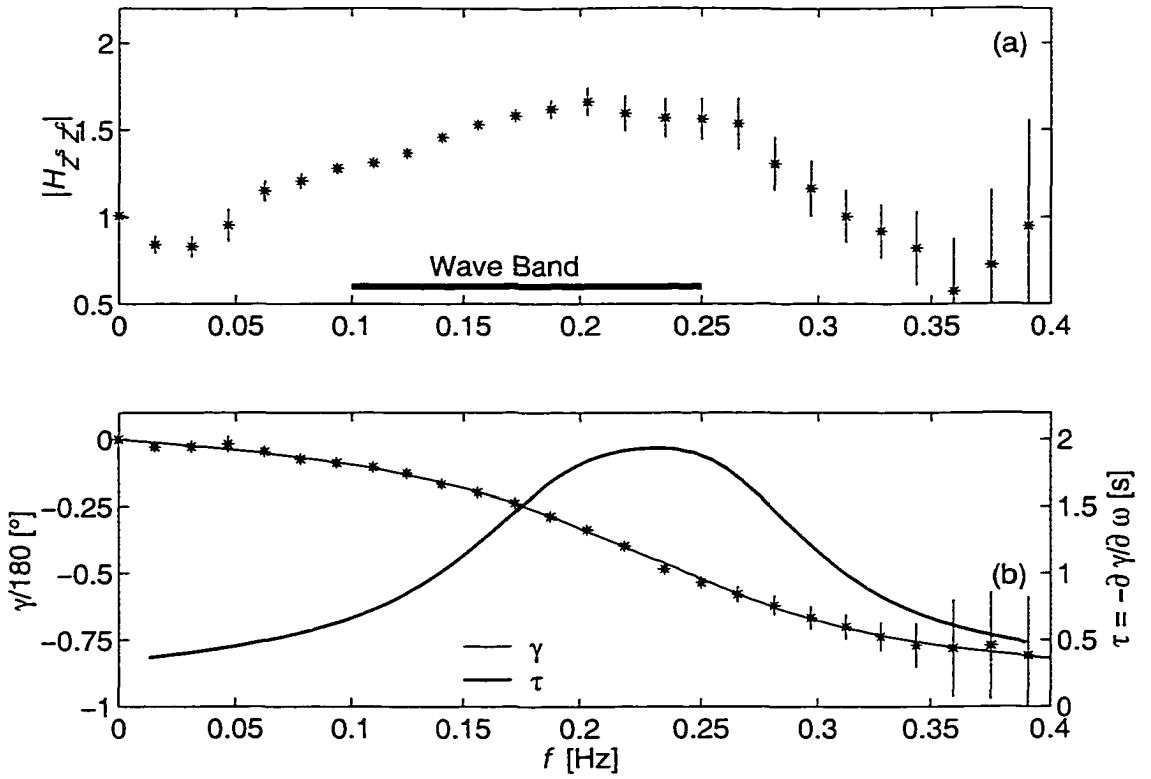

Fig. 6. Transfer function estimate (a) and phase (b–left axis) between ship and cage motions estimated from the acceleration records at 1 730 m. In (b), the thin line is a 5th–order polynomial fit to the frequency, using phase as the independent variable. The thick line is the time–lag (right axis) between the ship and cage acceleration.

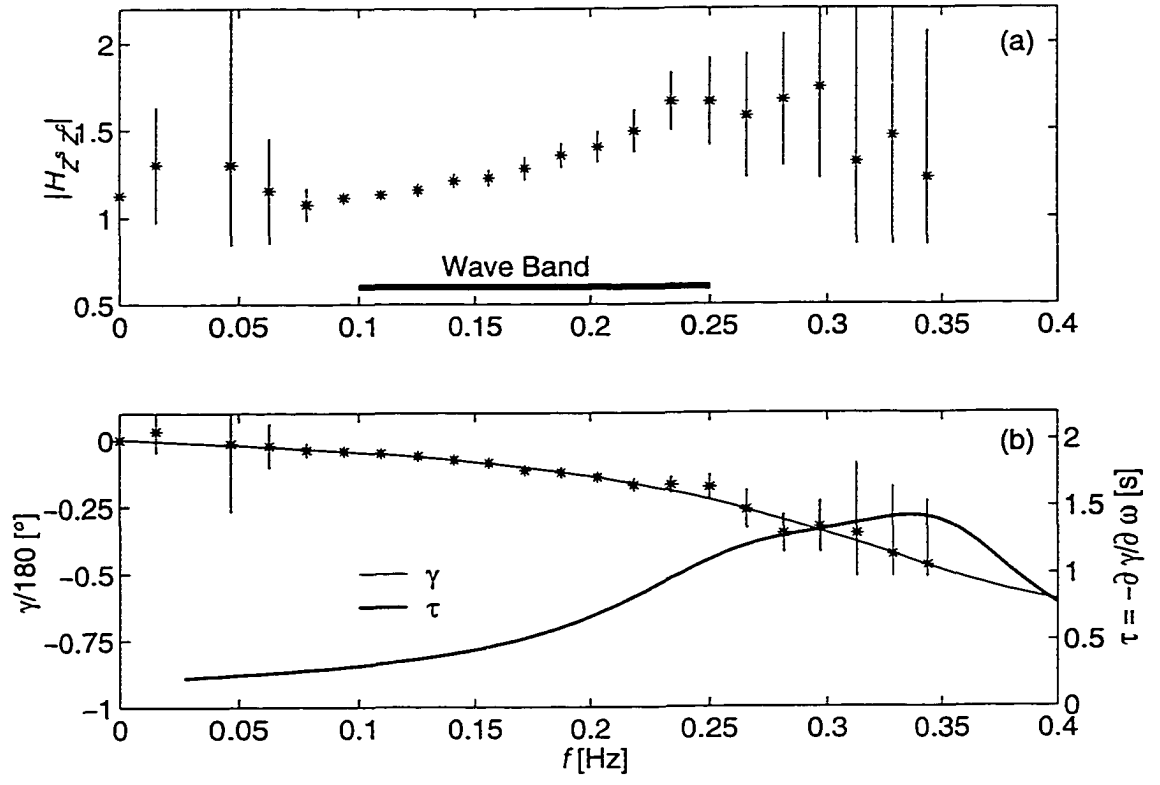

Fig. 7. Same as Fig. 6, but for 975 m depth.

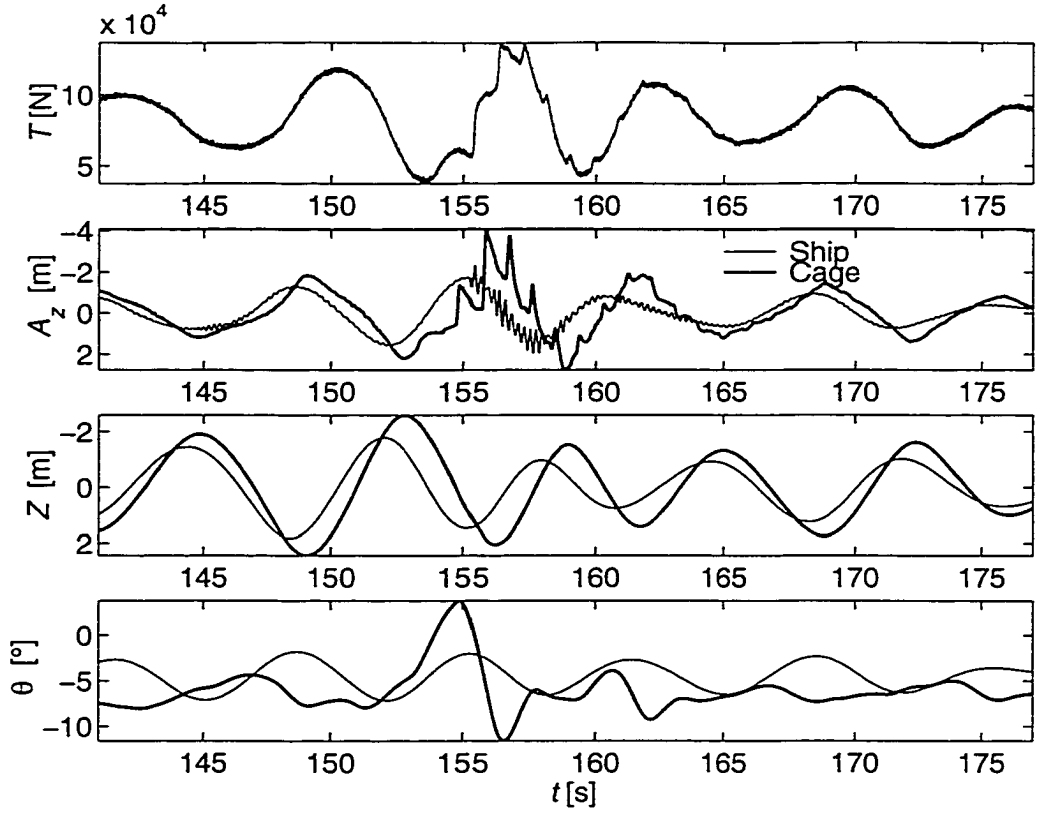

Fig. 8. Records of tension, vertical acceleration A_Z, vertical position Z and pitch θ, during a typical snap load. The snap load is identified by the large spikes (jerks) in the acceleration of the cage and rapid changes in the tension. Thin and thick lines are measurements at the ship and cage, respectively.

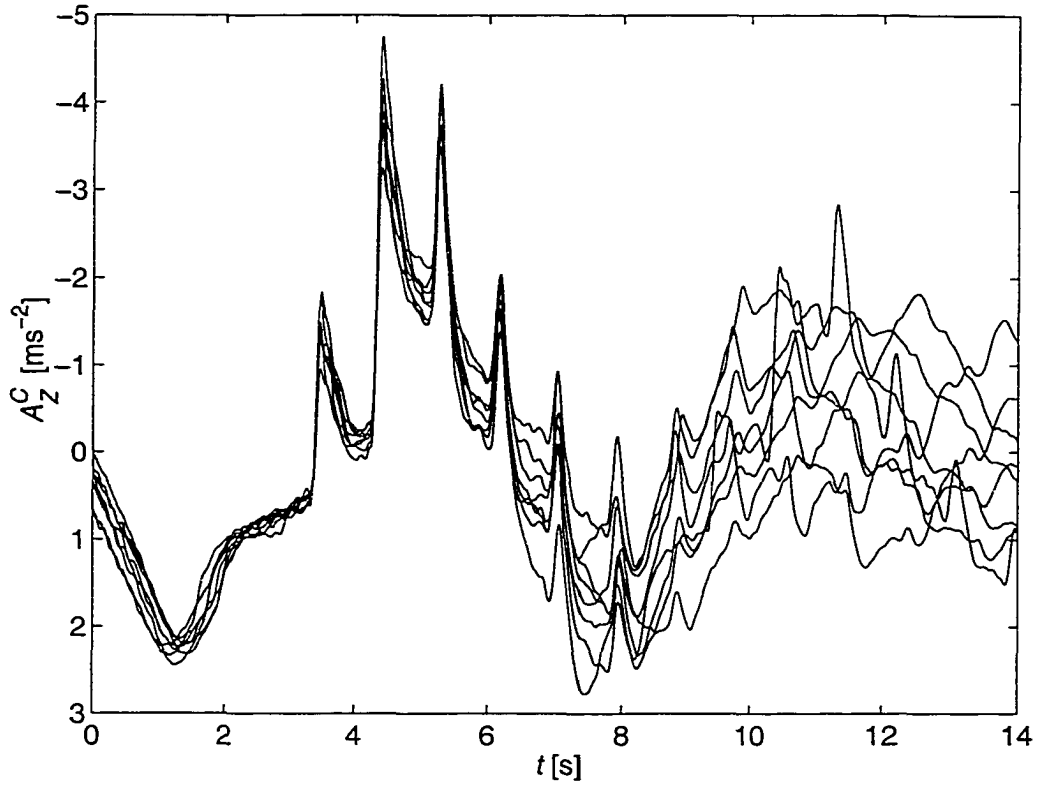

Fig. 9. Acceleration records of 8 snap loads overlaid, using the first jerk for alignment. The second and later jerks are remarkably well aligned and spaced by 0.9 s.

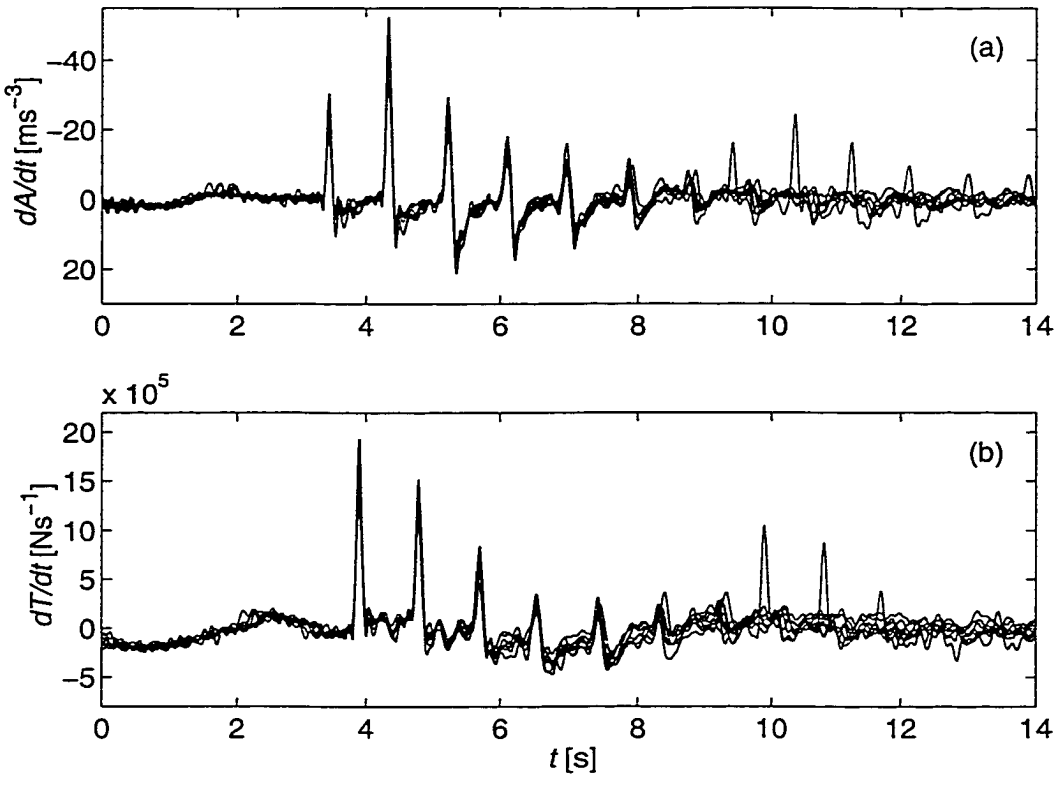

Fig. 10. Jerk at the cage (a) and time derivative of the tension (b) records for 8 snap loads overlaid, using the first jerk for alignment.

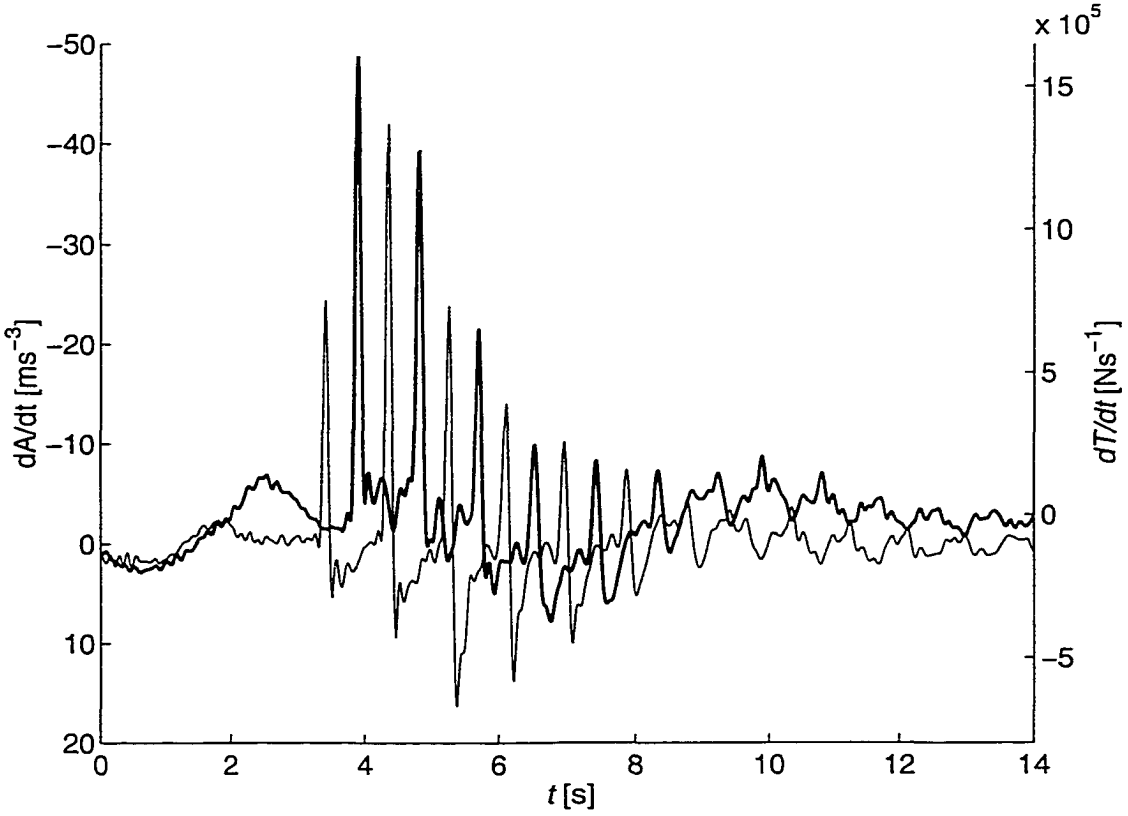

Fig. 11. Ensemble average of the 8 jerk records (thin line, left axis) and the 8 tension derivative records overlaid (thick line, right axis). The peaks of these records are spaced at 0.445 s.

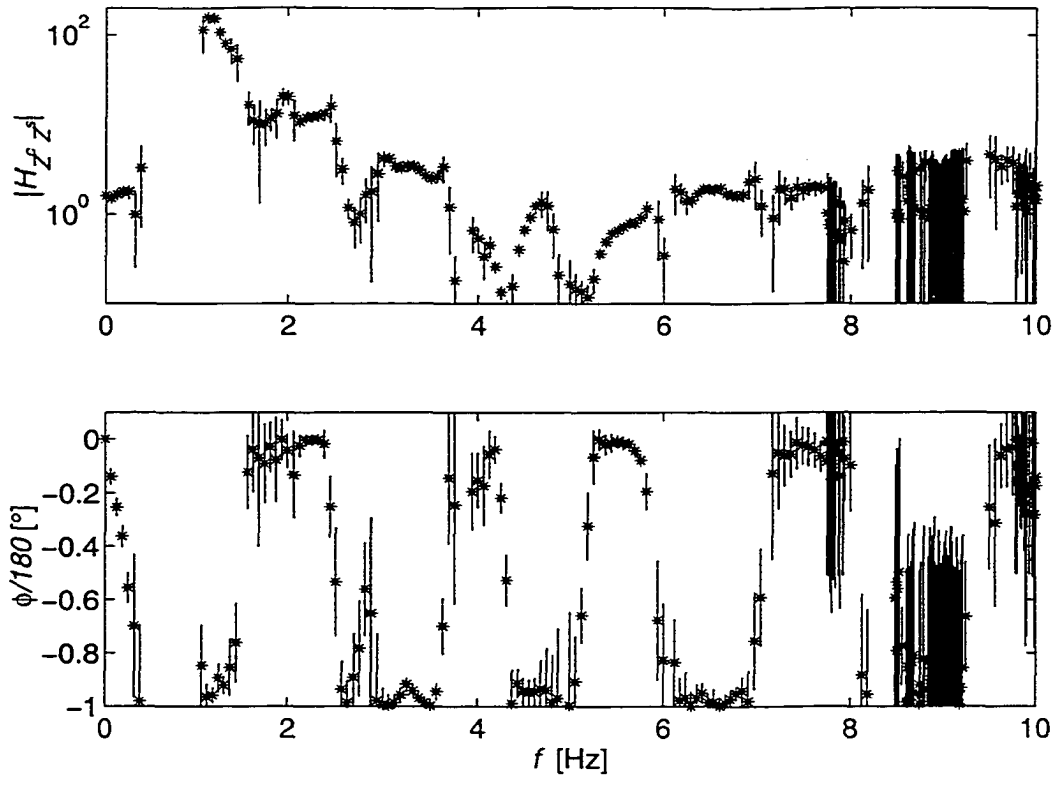

Fig. 12. The magnitude (a) and phase (b) of the transfer function estimated between the vertical ship and cage motions during the 8 snap loads.

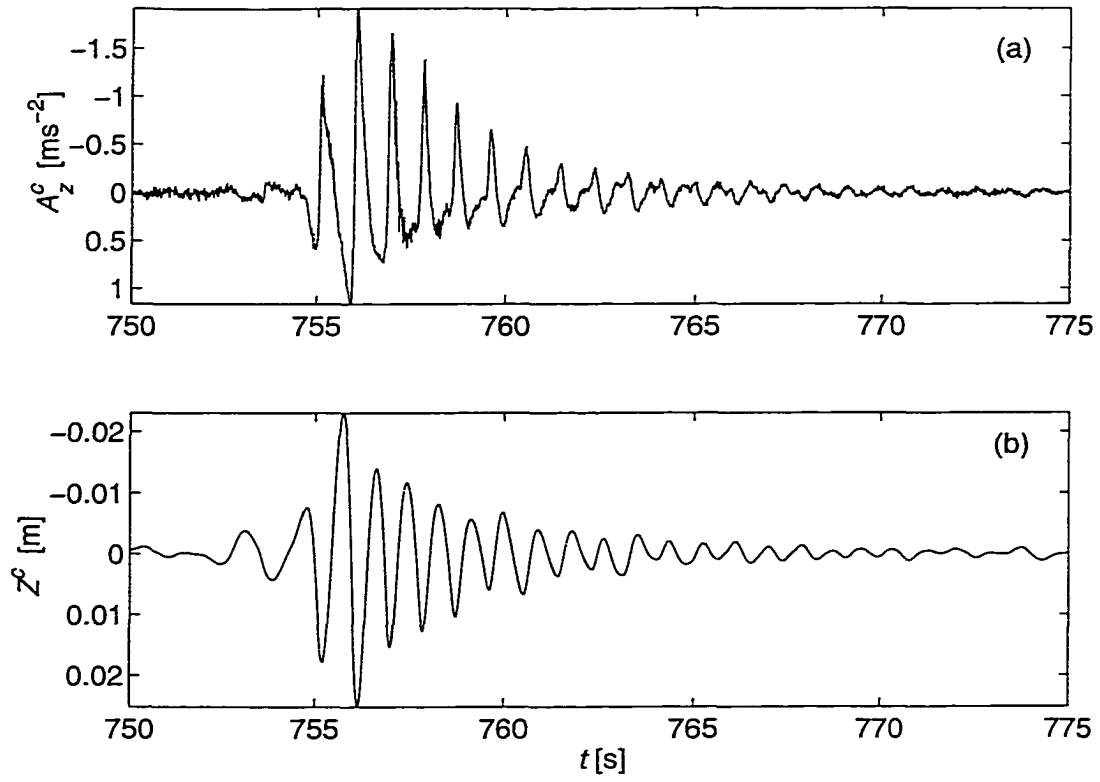

Fig. 13. High–frequency acceleration (a) and position (b) of the cage during a snap load. The motion records were high–pass filtered at 0.8 Hz to remove the low–frequency content. The motion is much larger than for typical operation and occurs predominately at 1.17 Hz (the 2nd harmonic of the natural frequency).

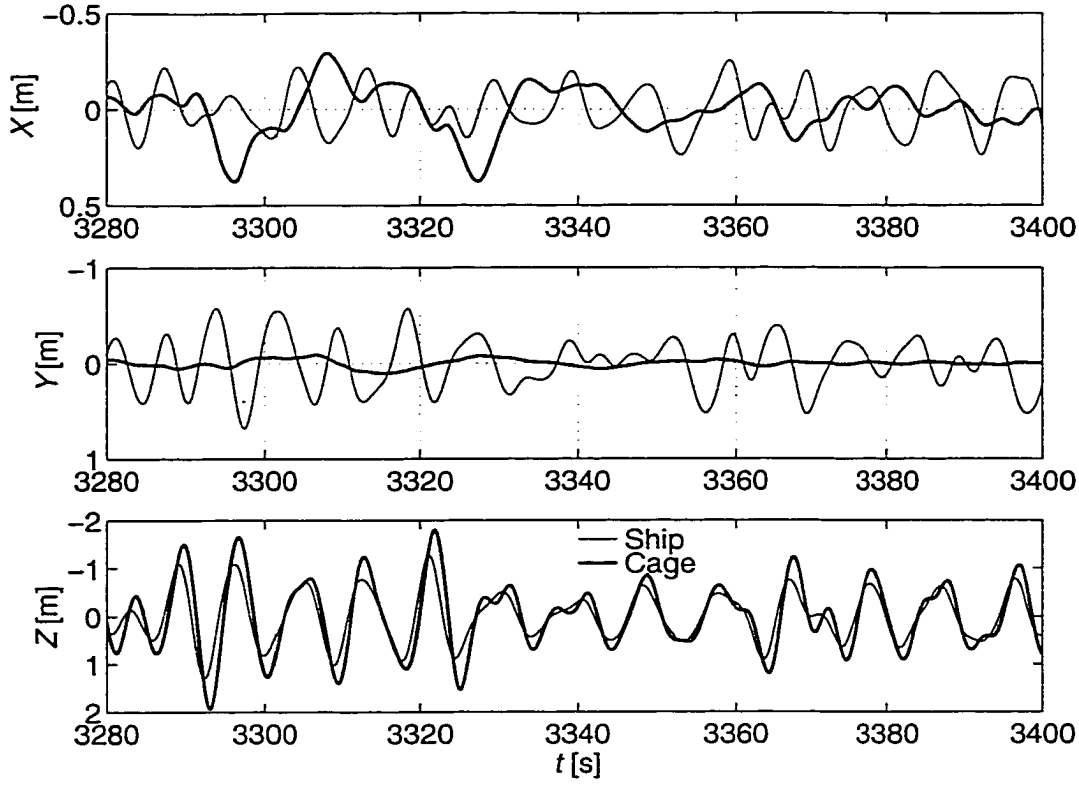

Fig. 14. X (a) and Y (b) and Z (c) positions of the ship and cage for typical operating conditions at 1 730 m. The thin (thick) line is the motions of the ship (cage).

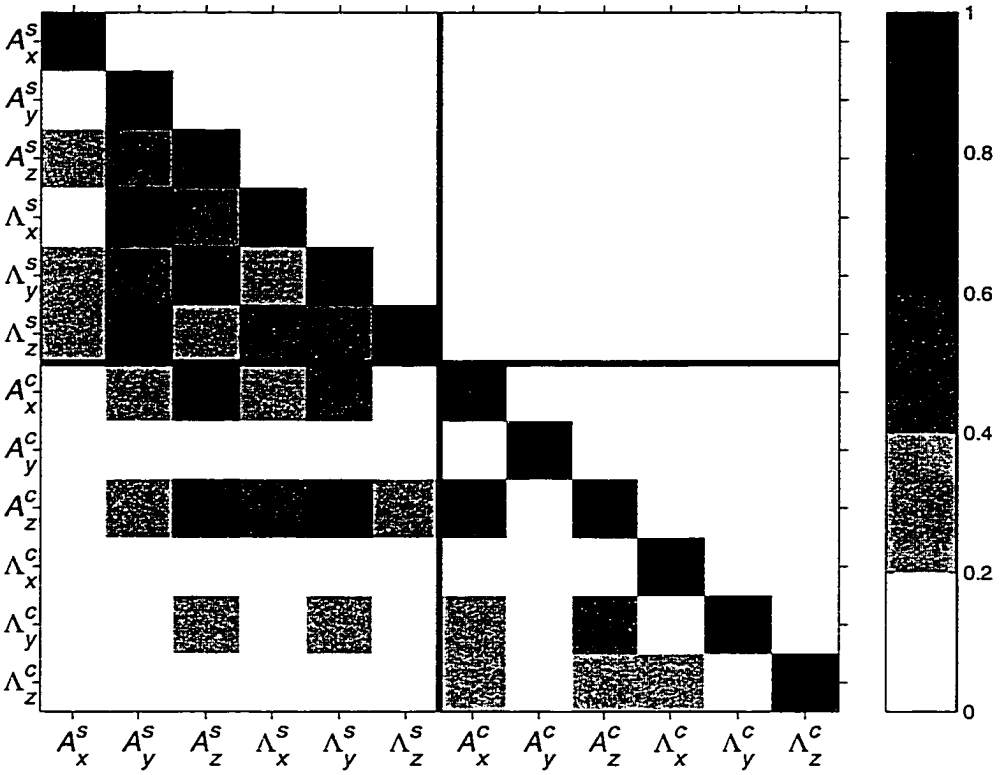

Fig. 15. Matrix of coherencies between all combinations of linear and angular acceleration records of the ship and cage, within the wave–band. The largest coherency is between the vertical accelerations of the ship and cage, $A_z^S - A_z^C$.

Appendix B

The Motion of a Deep–Sea Remotely Operated Vehicle System.

Part 2: Analytical Model

The Motion of a Deep–Sea Remotely Operated Vehicle System. Part 2: Analytical Model

F. R. Driscoll[a,*], R. G. Lueck[b] and M. Nahon[c]

(*In press, Ocean Engineering, 1999*)

[a] Department of Mechanical Engineering and School of Earth and Ocean Sciences, University of Victoria, Victoria, B.C., V8W 3P6
[b]School of Earth and Ocean Research, University of Victoria, Victoria, B.C., Canada, V8W 3P6
[c]Department of Mechanical Engineering, University of Victoria, Victoria, B.C., Canada, V8W 3P6

Abstract

We developed a continuous linear–elastic one–dimensional analytic model that should accurately represent a vertically tethered system subject to surface excitation. Our model accurately predicts: (a) the transfer function between the motion of the ship and cage, (b) the transfer function between ship motion and tension in the tether and (c) the natural frequency and its harmonics of the ROPOS deep–sea ROV system for depths between 0 – 1 765 m up to moderately rough sea conditions. By solving the ship–cage motion transfer function for the onset of zero tension in the tether, we were able to predict the amplitude of ship motion that triggers a snap load. The solution to our model requires only two non–dimensional parameters representing the mass ratio of the cage and tether and the force ratio of drag to tension. The predicted transfer function and natural frequency are not excessively sensitive to the value of these parameters for the ROPOS ROV system.

Keywords: *Tethered marine systems, remotely operated vehicles, ROV, tether, snap loading, cable dynamics, cable modelling.*

* Corresponding author.

1. Introduction

Remotely Operated Vehicles (ROVs) are the work horses of the deep sea industry. ROV systems effectively accomplish tasks in the dangerous high pressure environment of deep water while their human operators remain safely onboard the support ship. In addition to safety issues, ROVs have many advantages over other deep water work systems such as manned submersibles. In particular, ROVs can stay at the underwater work site indefinitely because their power is supplied by the ship, and the crew can be rotated without recovering the vehicle. These advantages are possible because the ship and undersea unit (cage and ROV) are connected by a tether (umbilical cable). The tethers typically consist of a core of electrical and optical conductors used to send power to and communicate with the ROV, surrounded by layers of armour used to support the undersea unit and protect the internal core. While the tether is the ROV's greatest advantage, it is also the greatest disadvantage. Operation in rough seas results in slack tether and large 'snap' loads which can damage the tether amour and the internal conductors. With damaged conductors, communication and power to the vehicle is cut off and the undersea unit becomes inoperable. Also during rough seas conditions, large vertical motions of the cage occur that make vehicle docking and system recovery difficult.

The ship and undersea unit are connected by a long elastic structural member–the tether, which can only sustain tensile loading and has length dependent properties. Clearly, the tether is very complex itself, but the addition of the non–linear characteristics of the cage make intuitive understanding of the system difficult. Thus, knowledge of the

dynamic interaction between the ship and cage is required to effectively build and safely operate ROV systems. Designing systems that operate far from, or at least can survive operation in, resonance requires accurate prediction of the natural frequencies and harmonics. Knowing the effects of ship motion on cage motion and tension in the tether is necessary to allow selection of ships with compatible motion characteristics that will not significantly excite the system so that snap loads result. This knowledge is obtained from experimental measurements and analytic models.

In part 1 of this paper (Driscoll, Lueck and Nahon, 1999 (hereafter DLN)), we presented motion and tension measurements of an ROV system operating at several depths between the surface and 1 765 m, and these yielded several significant insights into the system dynamics. In particular, the natural frequency and harmonics were determined and the natural frequency was found to be within the wave–band (the frequency band that contains 90% of the variance of the vertical acceleration of the ship, 0.1–0.25 Hz). The transfer function between ship and cage motion was also estimated and we found that the vertical cage motion was greater than that of the ship, which is consistent with the system operating at or near the natural frequency. Finally, several snap loads were recorded that exhibited remarkable temporal regularity.

In comparison with experimental measurements, analytic models provide a much more efficient and less costly method of quantifying the characteristics of dynamic systems. Probably one of the greatest advantages of analytic models is that they can be used to test and evaluate the behaviour of a system during the design process. Recent modelling of vertically tethered systems has been done extensively with discrete models

(Niedzwecki and Thampi, 1991, Hover and Yoerger, 1992, Driscoll and Biggins, 1993, and Huang and Vassalos, 1995) and little emphasis has been given to the effectiveness of continuous models. Although discrete models can calculate the response of systems over a much larger range than continuous models, they can be difficult to set up, require large computer resources and take long periods of time to investigate a few specific cases. Continuous models have a smaller range of application but can provided quick and accurate quantification of the dynamic characteristics. During the design process, when time is a significant factor, continuous models excel. Niedzwecki and Thampi, 1988 derived a closed form solution to a set of equations for a heave–compensated, multi–segment drill string. Huang and Vassalos used a simple single degree–of–freedom model to characterise the response of a vertically suspend mass to sinusoidal forcing. Continuous models are not common in recent literature and the validation of discrete and continuous models against data is virtually non–existent. A refreshing example is, Grosenbaugh, 1996, who compared motion and tension measurements of a long vertically tethered surface mooring with a continuous model. The model was accurate and an order of magnitude faster than numerical simulations.

In this paper, we develop a continuous one–dimensional linear–elastic model for a vertically tethered ROV system and find the closed form solution. Expressions for the natural frequency and harmonics, transfer function between ship and cage motion and transfer function between ship motion and tether tension are determined and agree well with those estimated from measurements of the ROPOS ROV system (DLN). We also developed an expression for the tension at all points along the tether which is used to predict the conditions for which snap loading will occur.

2. Analytical Model

Within the range of measurements presented in part 1 (DLN), the system was found to be weakly non–linear and with significant motion occurring only in the vertical direction. Therefore, we developed a continuous one–dimensional linear–elasitc analytic tether model of a caged deep–sea ROV system for vertical motions. Three coupled equations are used to model the system: a hyperbolic partial differential equation for the linear–elastic tether; a displacement function for the A–frame motion; and a second–order differential equation for the cage. Hydrodynamic added–mass and drag are only included in the cage equation where an equivalent linearization technique is applied to the quadratic drag.

2.1. Tether equation

The tether that is suspended vertically below the ship's A–frame can be approximated as an elastic rod when it is taut and therefore is modelled using a hyperbolic equation (Rao Chapter 8, 1990). The strain in the tether is less than 0.004 at the manufacturer's maximum recommended working load and the armour is wrapped around an incompressible core; therefore, the dilation of the tether will be very small and its cross–section is assumed to be constant. Gravitational effects on the tether are large. Since the tether constitutes 75% of the total overboard weight at full depth (5000 m), the static strain varies significantly along the length of the tether and can change by a factor of 4 between the cage and surface. Therefore, gravitational effects are included as a depth depended distributed load applied to the tether. The tangential fluid drag on the tether is

small and ignored. Defining the co–ordinate z as the vertical unstretched position along the tether, positive downward, the general linear–elastic tether equation is:

$$c^2 U_{zz} + K = U_{tt} \tag{1}$$

where the notation P_{XY} denotes differentiation of an arbitrary variable P with respect to X and Y, e.g.:

$$P_{XY} \equiv \frac{\partial^2 P}{\partial x \partial y};$$

and

$$c^2 = \frac{EA}{m}; \qquad K = \frac{g(\rho_C - \rho_W)A}{m};$$

$U(z,t)$ is the local displacement of the tether, t is the time, c is the speed of sound through the tether, E is its equivalent Young's modulus, A is its cross–sectional area, m is its mass per unit length, g is the gravitational acceleration, ρ_C is the density of the tether and ρ_W is the density of sea water.

2.2. A–frame equation

The vertical motion of the A–frame is assumed to be known and is modelled as a prescribed displacement function applied to the upper end of the tether. Assuming the sheave displacement to be harmonic, we write:

$$U(0,t) = Ye^{j\omega t} \tag{2}$$

where ω is the angular forcing frequency [rad s^{-1}]and Y is the amplitude of the displacement.

2.3. Cage equation

The cage is modelled as a point mass attached to the end of the tether, subject to gravitational, buoyancy, drag and tether tension forces. Since the vertical cage motion is weakly non–linear, and is normally distributed, we use an equivalent linearization of the quadratic drag (Caughey, 1963):

$$C_V^* = \left(\frac{2}{\pi}\right)^{\frac{1}{2}} \rho_W C_D A_C (U_t)_{rms}$$

where C_V^* is the cage equivalent linear–viscous drag coefficient; A_C is the cross–sectional area of the cage, C_D is the cage quadratic drag coefficient; and $(U_t)_{rms}$ represents the standard deviation of the cage velocity. Therefore, the differential equation for the cage is:

$$U_{zz}(L,t) = \frac{1}{EA}\left(W_{cg} - C_V^* U_t(L,t) - M U_{tt}(L,t)\right) \tag{3}$$

where W_{CG} is the weight minus buoyancy of the cage; and M is the mass of the cage (including entrained and added mass).

2.4. Non–dimensionalizaton

For generality, it is useful to non–dimensionalize the governing differential equations using:

$$z' = \frac{z}{L} \qquad t' = \frac{c}{L}t \qquad \omega' = \frac{L}{c}\omega \qquad \text{and} \qquad U' = \frac{U}{Y}$$

where L is the unstretched length of the tether. This non–dimensionalization yields equations and a set of solutions that are dependent only on two dimensionless parameters. It will be shown that the non–dimensional natural frequency and the harmonics are independent of L, within the depth range of measurements, and we use this knowledge to accurately estimate c. The resulting non–dimensional form of (1) is:

$$U'_{z'z'} + \beta = U'_{t't'} \tag{4}$$

where

$$U' = U'(z', t') \qquad \text{and} \qquad \beta = \frac{L^2}{Yc^2}\frac{g(\rho_C - \rho_W)A}{m}$$

The non–dimensional form of (2) is:

$$U'(0, t') = e^{j\omega' t'} \tag{5}$$

The non–dimensional form of (3) is:

$$U'_{z'}(1,t') = \frac{L}{EA}\frac{W_{cg}}{Y} - \xi U'_{t'}(1,t') - \zeta U'_{t't'}(1,t') \tag{6}$$

where

$$\xi = \frac{C_V^*}{mc} \qquad \text{and} \qquad \zeta = \frac{M}{mL}$$

and the non–dimensional parameter ξ represents the ratio of drag force on the cage to elastic force in the tether and ζ represents the cage to tether mass ratio.

2.5. The solution

To solve the system of equations, we first assume that U' is the sum of a static displacement v' and a dynamic displacement w', such that $U' = v' + w'$. The static solution is time independent, and thus, all time derivatives are identically zero. The static solution is:

$$v'(z') = -\frac{\beta}{2}(z')^2 + \left(\frac{W_{cg}L}{YEA} + \beta\right)z' \tag{7}$$

In dimensional form, v' is independent of Y, as would be expected of any static solution. The dynamic solution w is assumed to be:

$$w'(z',t') = Fe^{j\omega'(t'+z')} + Ge^{j\omega'(t'-z')} \tag{8}$$

Once equations (7) and (8) are substituted back into (4), we use (5) and (6) to solve for the coefficients F and G and we find that the dynamic solution is:

$$w'(z',t') = \frac{\left(\{\sin\omega' + \sigma\cos\omega'\}\sin\omega' z' + \{\cos\omega' - \sigma\sin\omega'\}\cos\omega' z'\right)e^{j\omega' t'}}{\cos\omega' - \sigma\sin\omega'} \qquad (9)$$

where

$$\sigma = \zeta\omega' - j\xi$$

The dynamic solution in non–dimensional time and space is only a function of ω', ξ and ζ. In the analysis, the most accurate results for $L = 0 - 1\,730$ m were obtained by using $\xi = 0.93$ and $\zeta = 1.78$. These values only differed by 14 and 16.5% from the values that were calculated using empirical data for the drag coefficient and added mass and manufacturer's specification data for the tether.

3. Model Predictions

In this section, we use the analytic model to calculate many of the system characteristics presented in part 1. In particular, the natural frequency and system harmonics predicted by (9) agree with the measured data from part 1. Within the wave–band, the transfer function between ship and cage motion estimated from the data and calculated using the model are very close in magnitude and are almost identical in phase. Using ship motion for input, the model accurately predicts the tension in the tether (at the surface) within the wave–band. Also, the model is used to predict the onset of zero tension in the tether, and thus, the ship motions for which snap loading will occur.

Of course, experimental data will not be available for most applications of our model and therefore exact values of ξ and ζ will not be known; and best estimates will have to be used in analyses. Therefore, if the model is to be useful, it must be robust and stable for variations in ξ and ζ. In the last part of this section, we investigate the sensitivity of the model to variations in ξ and ζ.

3.1. Natural frequency and harmonics

If the natural frequency or any of the harmonics should occur in or near the wave–band, the cage motion will be larger than the motion of the ship. Large motions would likely result in snap loading and make operation difficult. Therefore, the ability to accurately predict these frequencies during a design is important for the development of a safe, reliable and effective system. The natural frequency ω_1' ($2\pi f_1'$) is the smallest value of ω' for which the magnitude of the denominator of (9) is a minimum. The harmonics, ω_2', ω_3' ..., occur at subsequent minima. We cannot directly solve for the minimum because the slope of the denominator is discontinuous at the minima and is therefore not differentiable. However, when:

$$\omega' >> \frac{\xi}{\zeta} \tag{10}$$

we can neglect the imaginary part of σ and the denominator becomes purely real. Neglecting the imaginary part of the denominator is equivalent to ignoring the drag. The natural frequency and harmonics can be found by setting the real part of the denominator to be identically zero:

$$\omega_i' \tan(\omega_i') = \frac{1}{\zeta} \tag{11}$$

Using 1 765 m as a reference, ω_1' is almost equal to the r.h.s. of (10). However, at the second harmonic, ω_2' is 6 times larger than the r.h.s. of (10). We therefore used (9) to calculate the natural frequency and (11) to calculate the harmonics. For clarity and simplicity, we refer only to cyclic frequencies (f_i') for the remainder of this paper. Equations (9) and (11) yielded nearly identical values for each of the harmonics, f_2' and f_3', at each depth investigated, even though, at 5 000 m, $2\pi f_1'$ is only 2.3 times larger than the r.h.s. of (10). This is because the frequency for which the denominator of (9) is a minimum is relatively unaffected by drag, ξ, for the harmonics.

The non–dimensional natural frequency ranges between $f_1' = 0$ at 0 m and $f_1' = 0.16$ at 5 000 m. The harmonics occur at integer multiples of 0.5. They are nearly independent of depth and shift only slightly to higher frequencies with increasing depth (Table 1). At the harmonic frequencies, more motion is transferred between the ship and cage, and therefore, the coherency, Γ^2, between the ship and cage motions at these frequencies will be much larger than at intermediate frequencies. Thus, we use the coherency between the vertical acceleration records of the ship and cage to highlight the properties of the harmonics identified by the model. In particular, when the frequency axis is non–dimensionalized and scaled by 2, the peaks of the coherency for all depths occur at integer values (Fig. 1).

For several depths, Table 1 compares the measured values of the natural frequency, f_1', and the second, f_2', and third, f_3', harmonics against the values calculated using (9) and (11). The calculated and measured values agree remarkably well. The predicted natural frequency is within the 95% confidence interval of the measured 90° phase (DLN). The harmonics predicted by (9) and (11) are almost identical and are within 5% of the measured values. Equation (9) is slightly more accurate. Thus, (9) and (11) provide a simple and accurate method of predicting the natural frequency and its harmonics.

3.2. Transfer function and phase

In the high–frequency band ($f > 1.4$ Hz.), the ship motion is small and does not significantly excite the cage (DLN). Consequently, the error in the estimate of the transfer function is large above 1.4 Hz in the absence of snap loads. Therefore, we restrict our analysis to frequencies within the wave–band, 0.1 to 0.25 Hz, because a high degree of certainty exists for spectral estimates in this range.

In part 1 (DLN), we presented the transfer function estimates between vertical ship and cage acceleration records for depths of 1 730 and 975 m. For both cases, the magnitude of the transfer function estimates were greater than unity and the phase between the motions decreased with increasing frequency in the wave–band. The transfer function between ship and cage motion $H_{Z^S Z^C}(\omega')$, where the first subscript, Z^S (the vertical position of the ship), is the input and the second subscript, Z^C (the vertical

position of the cage), is the output, is found from (9) by simply dividing $w(1,t')$ by $w(0,t')$:

$$H_{z^s z^c}(\omega') = \frac{1}{\cos\omega' - \sigma \sin\omega'} \tag{12}$$

and thus, the phase is:

$$\angle H_{z^s z^c}(\omega') = \gamma = \tan^{-1}\left(\frac{-j\xi}{\cot\omega' - \zeta\omega'}\right) \tag{13}$$

The magnitude of the transfer function, its phase and lag estimated from the data are compared against (12) and (13) in Fig. 2 and 3 for 1 730 and 975 m, respectively. The vertical error bars give the 95% confidence interval of the estimates. The magnitude of the transfer functions calculated using (12) agrees very well with those estimated from the data. For example, at 1730, the calculated magnitude of the transfer function and that estimated from the data differ by at most 10% in the wave–band. The calculated magnitude is slightly less up to 0.18 Hz, after which, it is slightly larger. At 975 m, the agreement is even better with differences only reaching a maximum of 2% within the wave–band. The phase calculated from (13) and estimated from the data agree exceptionally well in the wave–band for all depths measured. In Fig. (2(b)) and (3(b)), we see that the calculated phase is always within the 95% confidence interval of the measurements.

The estimated lag (DLN) agrees very well with the frequency derivative of (13) for all depths (Figs. 2(a) and 3(b)). For 1 730 m, the agreement is good for all

frequencies. At 0.23 Hz, both lags peak and they differ by only 8%. For 975, the agreement is good up to 0.21 Hz. At higher frequencies, the agreement is not as good but the error bars on the measured data are large.

3.3. Tension

If the tension in the tether exceeds the manufacturer's recommended working limit, damage to the structural and internal conductors may result. Therefore, predicting the tension in the tether for any given sea condition is important because it provides a quantitative criterion for the selection of a tether. In this section, we use the solution to our model to develop an expression to calculate the tension at any location along the tether. Then using the prescribed motion of the ship (5), we calculate the transfer function between the ship motion and the tension in the tether. We use this transfer function to predict the frequencies and amplitudes of vertical ship motion for which the tether goes slack and snap loading is likely.

The tension in the tether is proportional to the strain in the tether. Therefore, the tension at any location in the tether is:

$$T = \frac{EAY}{L} U'_z \tag{14}$$

We define the non–dimensional tension as:

$$T' = \frac{L}{YEA} T \tag{15}$$

Substituting $U'_z = v'_z + w'_z$ into (14), we see that the tension is the sum of a static tension T'_{stat} and a dynamic tension T'_{dyn}, such that $T' = T'_{stat} + T'_{dyn}$. The static tension is:

$$T'_{stat} = (1 - z')\beta + \frac{W_{cg} L}{YEA} \tag{16}$$

For operation at 1 730 m, the static tension at the surface calculated using (16) and that measured are very close and are 82 157 and 82 530 N respectively. The dynamic tension is:

$$T'_{dyn} = \frac{\omega'\left(\{\sin\omega' + \sigma\cos\omega'\}\cos\omega' z' - \{\cos\omega' - \sigma\sin\omega'\}\sin\omega' z'\right)e^{j\omega' t'}}{\cos\omega' - \sigma\sin\omega'} \tag{17}$$

The transfer function between the ship motion and the tension in the tether is calculated by dividing (17) by the prescribed ship motion (5). Since the tension was only measured at the surface, we validate (17) by comparing the calculated transfer function at that point,

$$H_{Z^S T^S} = T'_{dyn}(\omega')\big|_{z'=0} e^{-j\omega' t'} = \frac{\omega'(\sin\omega' + \sigma\cos\omega')}{(\cos\omega' - \sigma\sin\omega')}, \tag{18}$$

against the measured transfer function. The measured transfer function is compared against (18) in Figs. 4 and 5 for 1 730 and 975 m, respectively. Again, the vertical error bars give the 95% confidence interval of the estimates. For all depths, the estimated and calculated transfer functions agree very well for frequencies up to 0.2 Hz in the wave–band, but deviate at higher frequencies. The maximum difference is 16% at 0.25 Hz for 1 730 m and this difference decreases with decreasing operating depth. At 975 m, the

maximum difference is only 10% and the calculated transfer function agrees, within the 95% confidence interval, with all measurements within the wave–band.

Snap loading is preceded by the tension going to zero and slack developing in the tether. Although the model is only valid when the tether is taut, it can be used to predict the ship motion for which the tension in the tether approaches zero. Therefore, we use (5) and (17) to predict the amplitudes and frequencies for which the tether will go slack at the cage. The tension at the cage is the sum of the static and dynamic tension at $z' = 1$:

$$T' = \frac{W_{cg} L}{YEA} + H_{Z^S T^C} e^{j\omega' t'} \tag{19}$$

and

$$H_{Z^S T^C} = \frac{\omega' \sigma}{\cos\omega' - \sigma \sin\omega'} \tag{20}$$

where $H_{Z^S T^C}$ is the vertical ship position–cage tension transfer function. The critical amplitude at which the tether tension (19) goes to zero is given by:

$$Y_{CR} = \frac{\dfrac{W_{cg} L}{EA}}{\left| \dfrac{\omega' \sigma}{\cos\omega' - \sigma \sin\omega'} \right|} \tag{21}$$

Lines of zero tension, Y_{CR}, are plotted in Fig. 6 in the frequency range of 0 to 0.4 Hz for operating depths of 930 and 1 730 m. Snap loads are predicted to occur when the amplitude of surface displacement, Y, exceeds the critical value. The amplitude for

which the tension is zero decreases with increasing frequency to a minimum near the natural frequency. The vertical motion of the cage is normally distributed, and therefore, an estimate of Y that contains 99% of the measured amplitudes (in the wave–band) can be calculated using:

$$Y = 2.5\sqrt{\int C_z^S d\omega}$$

where C_z^S is the spectrum of the vertical displacement of the ship and the integration is done over the wave–band. Indeed Y did exceed the lines of zero tension over a small range at higher frequencies in the wave–band (Fig. 6) — the tether remained taut for most sea conditions; however, in a few cases during extreme motions, Y did exceed the lines of zero tension, slack developed and snap loads resulted.

3.4. Sensitivity

Only two non–dimensional variables, ξ and ζ are needed in our model to characterise any vertically tethered system and determine the associated transfer functions, natural frequency and harmonics. If motion/tension data are not available (e.g. in the design process), values for ξ and ζ can be calculated using estimates of the tether stiffness, cage drag coefficient, rms vertical velocity, tether mass per unit length, and the mass of the cage (including entrained water). Using this method, precise values of ξ and ζ will not be known. If small changes in ξ and ζ result in large changes in the model predictions, the utility of the model would be limited. Therefore, our model must yield reasonably accurate results for small variations in ξ and ζ if it is to be considered a

useful tool. We calculated the relative changes in natural frequency, its harmonics and the magnitude and phase of the transfer functions to variations of ξ and ζ of up to $\pm 25\%$ around their optimal values. We did this by calculating:

$$\frac{1}{X}\left(\frac{\partial X}{\partial \xi}\right)d\xi \qquad\qquad \frac{1}{X}\left(\frac{\partial X}{\partial \zeta}\right)d\zeta$$

where X is any function of interest. The phase of the transfer function was close to zero at lower frequencies and to avoid large unrepresentative values for the relative change, we calculated the change of phase for variations of ξ and ζ.

Sensitivities of the natural frequency and its harmonics were calculated using (9) and (11), respectively (Table 2). The largest percent change of the frequencies predicted by (9) was 17% at 5 000, but this corresponds to a change in magnitude of only 0.017 Hz. The largest variation at any depth was only 0.05 Hz. Equation (11) was only slightly affected by variations of ξ and ζ. Clearly, the calculated values of the natural frequency are insensitive to variations in ξ and ζ, and thus, (9) and (11) provide good estimates the natural frequency and its harmonics.

For operating depths of 975 and 1 730 m, Figs. 7 and 8 present the sensitivity of the transfer function $H_{z^s z^c}(\omega')$ between the vertical motion of the ship and cage to variations in ξ and ζ. Scaling both the frequency and vertical axes in proportion to $L^{0.5}$ yields a sensitivity to the mass ratio, ζ, that is independent of depth. A similar result is obtained for the sensitivities to the force ratio, ξ, by scaling only the frequency axis in

proportion to $L^{0.5}$. Within the wave–band, the magnitude is most sensitive to variations in ξ while the change in phase is most sensitive to variations in ζ. In the wave–band, $\pm 25\%$ variations in either parameter yield a maximum change in the magnitude and phase of $H_{z^s z^c}(\omega')$ of only 33% and 20° at 1 730 m, respectively. Therefore, we conclude that a reasonably accurate prediction of the magnitude and phase can be obtained using "rough" estimates of ξ and ζ. An interesting phenomenon can be seen in Fig. 7(b) where the sensitivities are identically zero at 0.22 Hz (0.31 Hz) for depths of 1 730 m (975 m). The phase is independent of ξ at these frequencies. A similar result occurs between 0.21 and 0.23 Hz (0.3 and 0.35 Hz) for 1 730 m (975 m) where the magnitude of the transfer function is only slightly sensitive to variation in ζ (Fig. 8(a)).

The sensitivity of the magnitude of the transfer function between ship displacement and tension at the surface, $\left|H_{z^s T^c}\right|$, is also independent of depth when the frequency is scaled in proportion to $L^{0.5}$ for variations of ξ and ζ and when the sensitivity is scaled by $L^{0.5}$ for variations of ζ. The maximum change of the transfer function was 28 and 35% for variations in ξ and ζ, respectively (Fig. 9). At 0.16 Hz (0.21 Hz) and between 0.26 and 0.3 Hz (0.35 and 0.4 Hz) the magnitude of the transfer function is independent of ξ and only slightly sensitive to changes in ζ, respectively for 1 730 m (975 m) operation.

4. Discussion and Conclusion

The merit of any analytic model is its ability to predict the response of the modelled system to specified inputs and to quantify system characteristics. We developed a continuous linear–elastic one–dimensional model to describe the behaviour of vertically tethered systems. Boundary conditions are a prescribed displacement at the surface (usually imparted by surface waves) and a force balance at the bottom end of the tether (tension, weight, drag and mass acceleration). Our model gives ROV designers and operators a quick and inexpensive tool to estimate cage motions, tension in the tether, the natural frequency and harmonics of the system and many other characteristics at all operating depths for a given vertical motion of the ship. We validated our model by comparing the model output against measurements of a real ROV system (the ROPOS deep–sea ROV system) and found that: (a) predicted values of the natural frequency differed by at most 10% and were within the 95% confidence interval of the measured values; (b) measured and calculated values of the harmonics differed by at most 5%; (c) the magnitude of the calculated transfer function, $\left|H_{z^s T^c}\right|$, between the motion of the ship and cage differs from that estimated from the data by at most 10% within the wave–band and the depth range 0 – 1 726 m; (d) the calculated phase of $H_{z^s T^c}$ is always within the 95% confidence interval of the measurements; and (e) the maximum difference between the measured and calculated magnitude of the transfer function of ship motion and tension in the tether (at the surface) is only 16%. Our model is accurate but it has limitations. The drag acting on the cage is quadratic, but it is linearized for a "steady" amplitude of vertical motion. Thus, our model is not appropriate for non–stationary motions. Also, the model is invalid for a slack tether, and so, it does not apply to a snap

load. However, our model can be used to predict the minimum amplitude of surface motion that leads to zero tension and the onset of a snap load. Discrete models are not limited by either these conditions.

Any model should be robust and stable with respect to variations in its parameters. The solution to our model is a single non–dimensional equation that depends on two non–dimensional parameters which represent the force ratio of drag to tension, ξ, and the mass ratio of the cage and tether, ζ. We calculated the sensitivity of our model to these parameters and found that: (a) the natural frequency predicted by (9) is insensitive to variations in ξ and ζ; (b) the harmonics predicted by (11) are nearly independent of ξ and ζ; and (c) the transfer functions between the motion of the ship and cage and between the motion of the ship and tension in the tether are only moderately sensitive to variations in ξ and ζ.

For comparison with the parameters of the ROPOS ROV system ($\xi = 0.93$ and $\zeta = 1.78$), the parameters for a more streamlined and massive platform (a piston coring tool) and a less streamlined platform (a water sampling rosette) are $\xi = 0.46$ and $\zeta = 2.50$; and $\xi = 1.27$ and $\zeta = 1.9$,respectively for $L = 1\ 730$ m. These values are reasonably close (within a factor of 2) to those for the ROPOS system, and therefore, each of these systems will have similar dynamic characteristics — motion amplification at the underwater platform, frequency dependent lag and natural frequencies close to the wave–band. Because the ratio of ξ to ζ for the piston coring tool is less than for the ROPOS system, the natural frequency and its harmonics are more accurately predicted by

(11) than for the ROPOS system. In the extreme case of a streamlined body suspended by a stiff tether, $\xi \approx 0$ and (11) provides exact values for the natural frequency and its harmonics.

The tether length, L, and the speed of tensile waves, c, provide the non–dimensionalization of frequency and time. The harmonics of the natural frequency are nearly independent of ξ to ζ and occur at integer multiples of $c(2L)^{-1}$ (see Fig. 1). Although, most parameters of a tether (mass per unit length, diameter, etc.) are usually available, the tensile stiffness, EA (used to calculate c), may be unavailable or only poorly determined. The stiffness, EA, can be determined by force–strain measurements using specialised equipment. The non–dimensionalization offers an alternative approach. Impulsive loading of the tether (e.g. suddenly stopping the winch) generates a tension (strain) wave. This tension wave is lightly damped, travels along the tether at a speed c and is reflected at its terminations (the ship and cage) (DLN). The speed of the tensile waves, c, is independent of the tension in the tether and can be estimated from the time between successive tension maxima (spikes) at the surface.

When the non–dimensional parameters ξ and ζ cannot be estimated using experimental measurements, they can be estimated using the tether stiffness, cage drag coefficient, rms vertical velocity, tether mass per unit length, and the mass of the cage (including entrained water). Can we accurately estimate ξ and ζ using information available during the design process? Using empirical data for the drag coefficient and added mass, the tether manufacturer's specification data and the measured rms vertical cage velocity, we initially estimated values of $\xi = 1.06$ and $\zeta = 2\,520L^{-1}$ which differ by

only 14 and 16.5% from the values that give the best agreement with the measured transfer function between the vertical motions of the ship and cage. The uncertainty stems mainly from the estimation of entrained mass, tether stiffness and, to a lesser extent, the drag coefficient. (When data for the cage velocity is not available, it can be estimated by iterative use of the model). Had we used the initial estimates of ξ and ζ, our predictions for the natural frequency, f_1', and its harmonics, f_2' and f_3', the magnitude and phase for the transfer function between the motion of the ship and cage and the magnitude of the transfer function between ship motion and tension in the tether (at the surface) would have differed by only 3%, 0.9%, 0.3%, 14%, 15° and 19%, respectively, from the real system at 1 730 m.

Acknowledgements

We would like to thank Jim McFarlane and the staff of International Submarine Engineering (ISE) for their continual support and assistance in this project. F.R. Driscoll was financially supported by scholarships from the Natural Science and Engineering Research Council (NSERC), the Science Council of British Columbia (SCBC) and ISE. This work was partially supported by the US Office of Naval Research under contract N00014–93–1–0362 and NSERC .

References

Caughey, T.K. 1963. Equivalent linearization techniques. *Journal of the Acoustic Society of America* **35.** 1706–1711.

Driscoll F.R. and Biggins L. 1993. Passive damping to attenuate snap loading on umbilical cables of remotely operated vehicles. *IEEE Oceanic Engineering Society Newsletter* **28**, 17-22.

Driscoll, F.R., Lueck, R.G., and Nahon, M. 1999. The motion of a deep–sea remotely operated vehicle. Part 1: motion observations. *Submitted to Ocean Engineering.*

Grosenbaugh, M.A. 1996. On the dynamics of oceanographic surface moorings. *Ocean Engineering.* **32**, 7–25.

Hover, F.S. and Yoerger, D.R. 1992. Identification of low–order dynamic models for deeply towed underwater vehicle systems. *International Journal of Offshore and Polar Engineering.* **2**, 38–45.

Huang, S. and Vassalos, D. 1995. Chaotic heave motion of marine cable–body systems. *Proceedings of the ISOPE–Ocean Mining Symposium*, Tsukuba, Japan. 83–90.

Niedzwecki, J.M. and Thampi, S.K. 1988. Heave Compensated Response of Long Multi–segment Drill Strings, *Applied Ocean Research.* **10**, 181–190.

Niedzwecki, J.M. and Thampi, S.K. 1991. Snap loading of marine cable systems. *Applied Ocean Research.* **13**, 210–218.

Rao, S.S. 1990. *Mechanical Vibrations*. Addison–Wesley Publishing Company, New York.

Table 1. The calculated and measured natural frequency (f_1') and its second (f_2') and third (f_3') harmonics for several depths.

Depth		Measured	Predicted by (9)	Predicted by (11)
631	f_1'	-	0.067	0.070
	f_2'	0.49	0.51	0.51
	f_3'	0.96	1.01	1.01
975	f_1'	0.088	0.080	0.085
	f_2'	0.51	0.52	0.52
	f_3'	0.98	1.01	1.01
1378	f_1'	0.092	0.092	0.099
	f_2'	0.51	0.52	0.52
	f_3'	1.00	1.01	1.01
1730	f_1'	0.10	0.099	0.11
	f_2'	0.52	0.53	0.53
	f_3'	1.01	1.01	1.01
5000	f_1'	-	0.13	0.16
	f_2'	-	0.56	0.57
	f_3'	-	1.04	1.04

Table 2. Percent changes in the predicted natural frequency and its second and third harmonic for ± 25% variations in the non–dimensional parameters ξ and ζ.

Depth		+25% ξ	-25% ξ	+25% ζ	-25% ζ
631	f_1'	-2.4	1.9	-9.2	12.8
	f_2'	-	-	-0.4	0.6
	f_3'	-	-	-0.1	0.2
975	f_1'	-3.7	2.8	-8.7	11.7
	f_2'	-	-	-0.6	1.0
	f_3'	-	-	-0.2	0.3
1378	f_1'	-5.1	3.8	-8.1	10.6
	f_2'	-	-	-0.8	1.3
	f_3'	-	-	-0.2	0.4
1730	f_1'	-6.4	4.6	-7.6	9.9
	f_2'	-	-	-1.0	1.5
	f_3'	-	-	-0.3	0.4
5000	f_1'	-17.0	10.1	-5.1	6.2
	f_2'	-	-	-2.0	3.0
	f_3'	-	-	-0.7	1.1

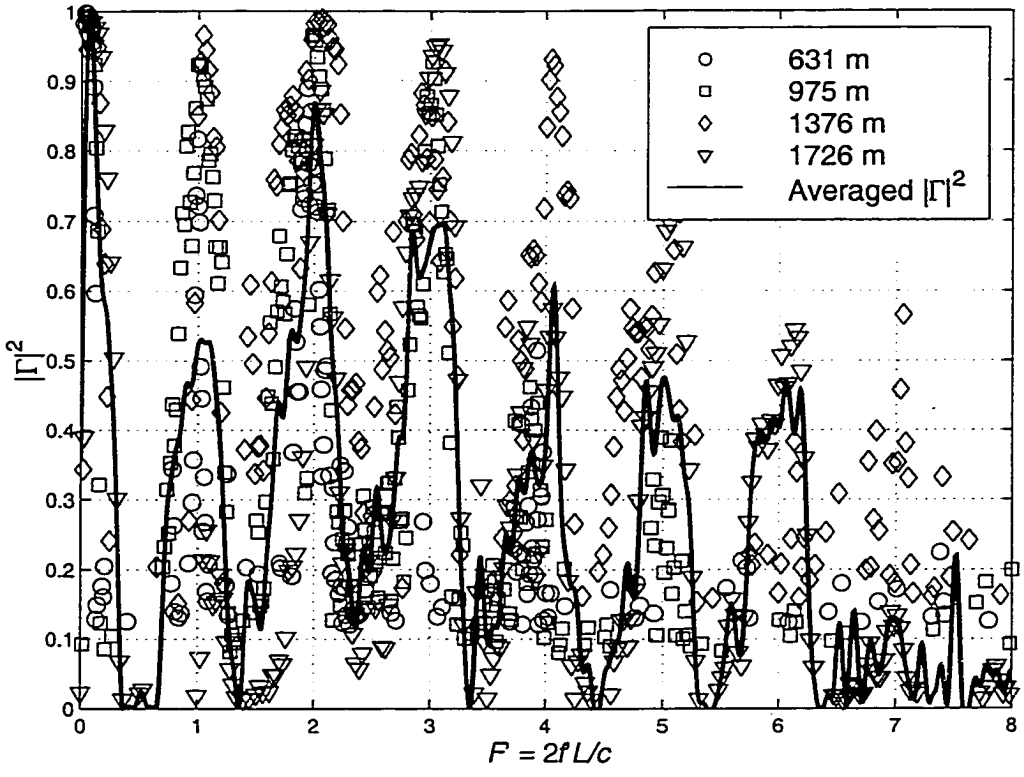

Fig. 1. Coherency, Γ^2, between the vertical acceleration records of the ship and cage for several depths as a function of frequency (non-dimensionalized by depth and the speed of tensile waves in the tether).

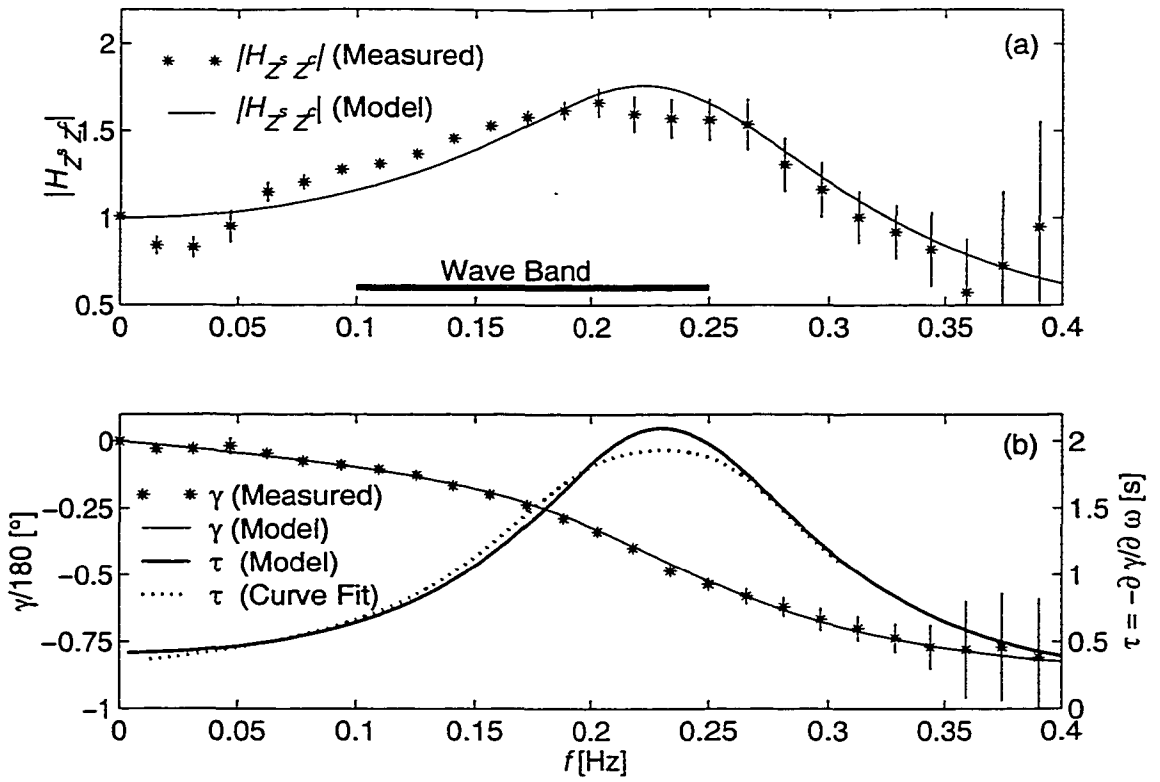

Fig. 2. The magnitude (a) and phase (b) of the transfer function between ship and cage motions estimated from the data (stars) and calculated by our model (thin solid lines) for operation at 1 730 m. The time–lag between the ship and cage acceleration (right axis) estimated from the data (thick dots) and calculated by our model (thick solid line) are also shown in (b).

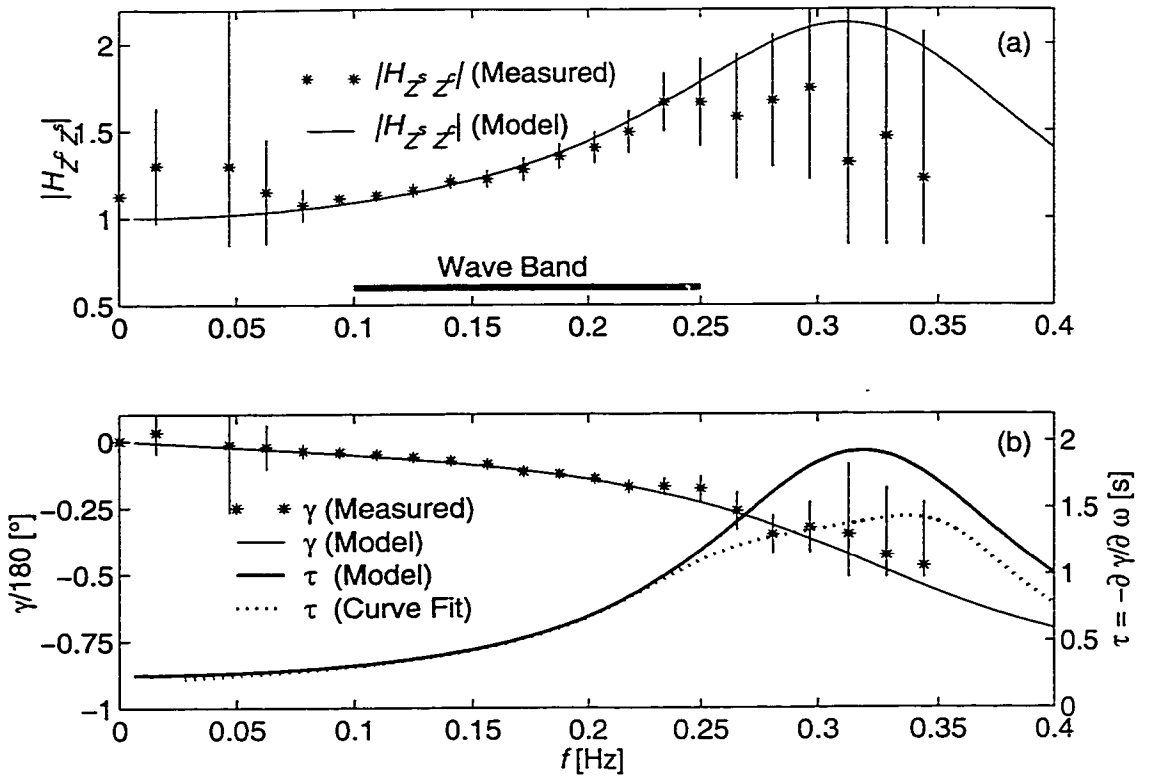

Fig. 3. Same as Fig. 2, but for 975 m depth.

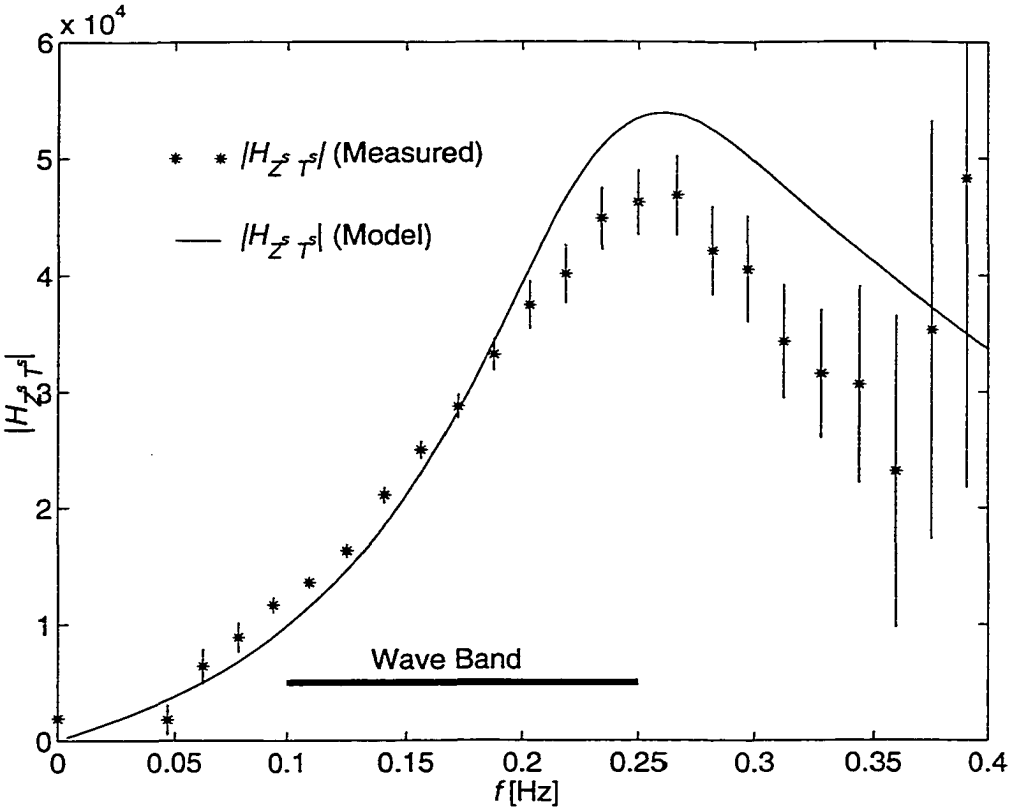

Fig. 4. The magnitude of the transfer function between ship motion and tension in tether (at the ship) estimated from the data (stars) and calculated by our model (solid line) for operation at 1 730 m.

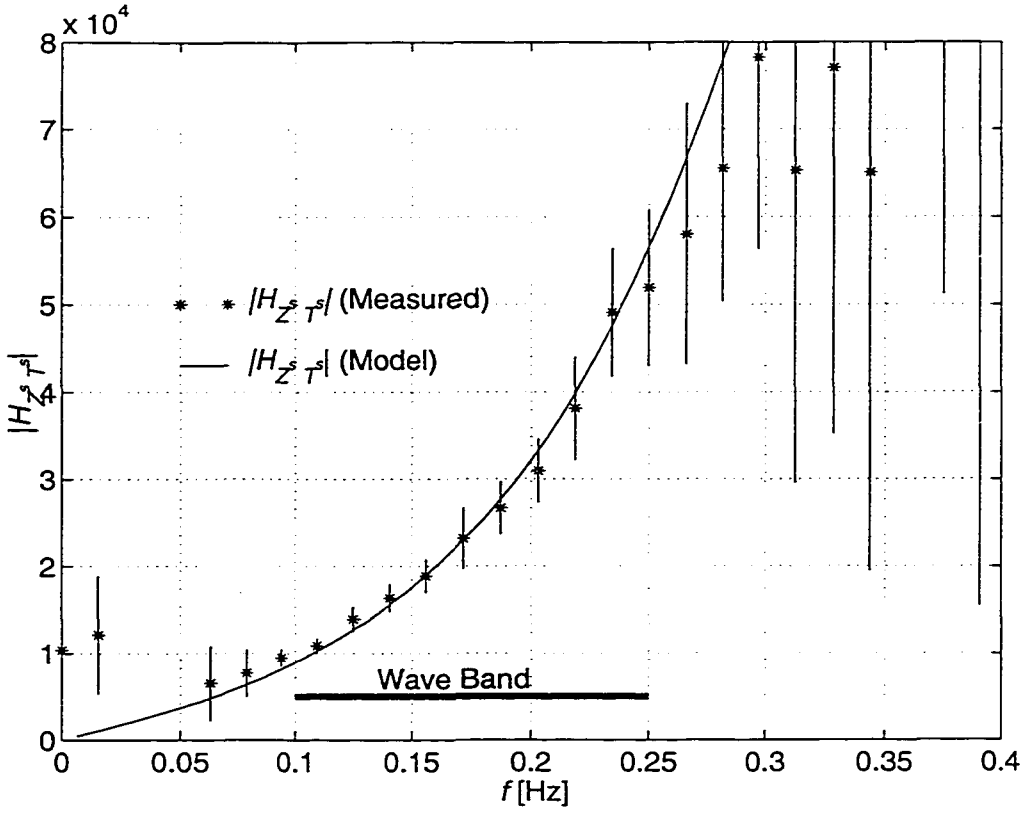

Fig. 5. Same as Fig. 4, but for 975 m depth.

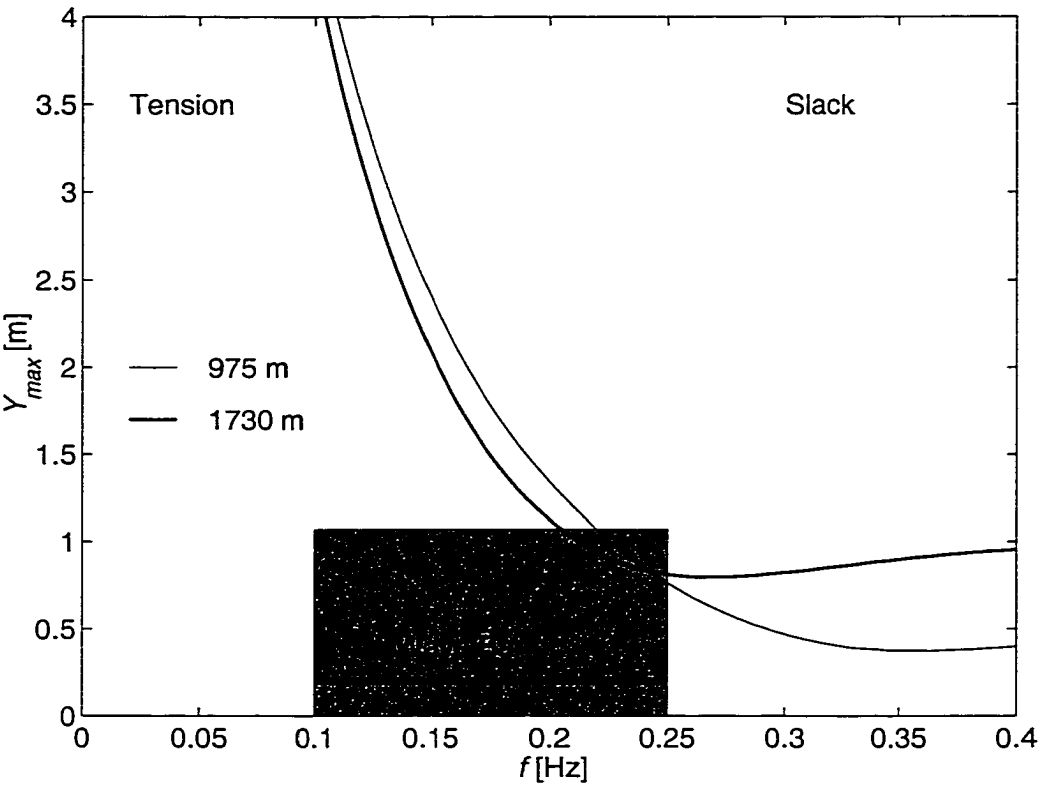

Fig. 6. Amplitude and frequency of ship motion at which the tether will go slack. The tether is taut (slack) in the region to the left (right) of the solid lines. The shaded square contains 99% of the measured amplitude, Y, in the wave–band.

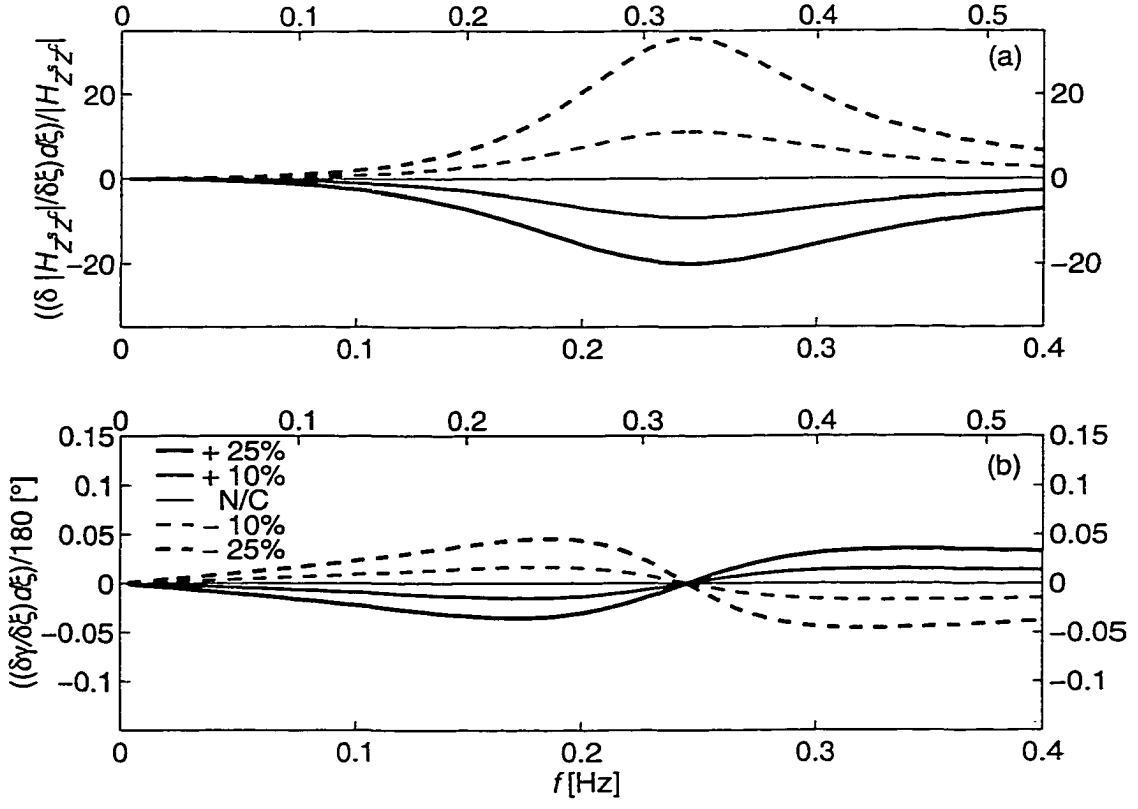

Fig. 7. Sensitivities of the magnitude (a) and phase (b) of the transfer function between ship and cage motion to changes in the non–dimensional variable ξ for operating depths of 975 (upper and right axes) and 1 730 m (lower and left axes).

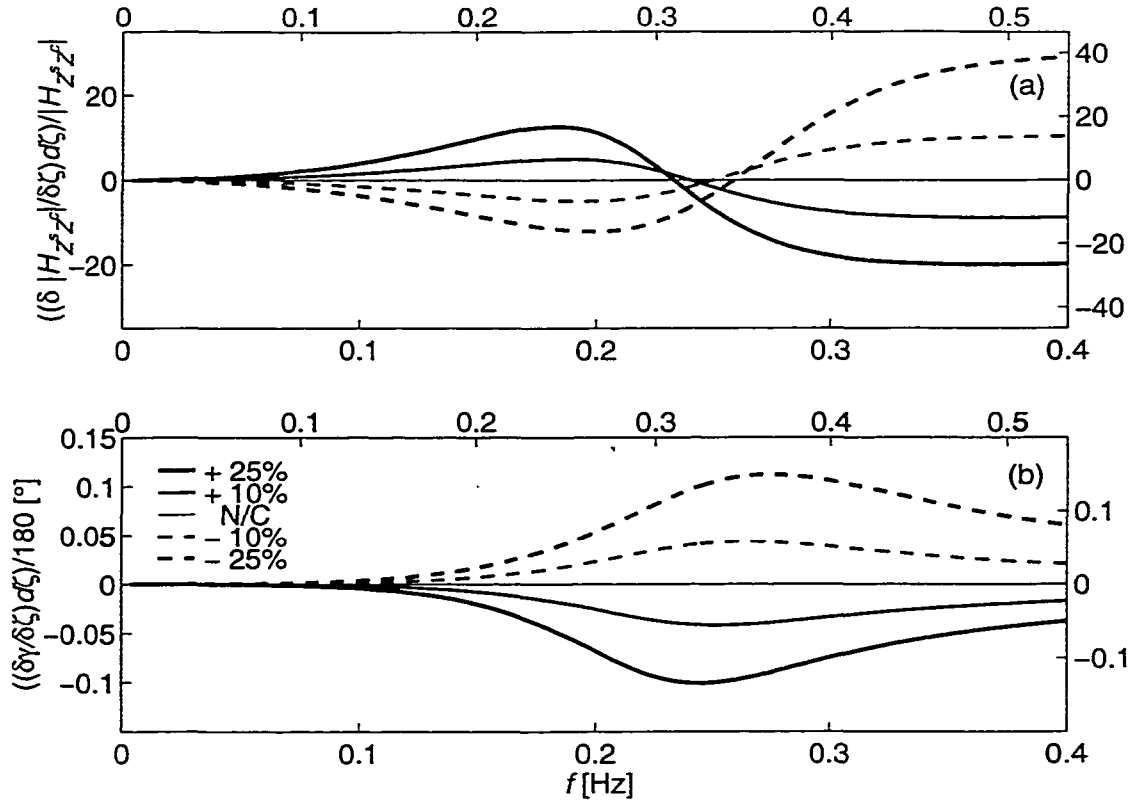

Fig. 8. Sensitivities of the magnitude (a) and phase (b) of the transfer function between ship and cage motion to changes in the non–dimensional variable ζ for operating depths of 975 (upper and right axes) and 1 730 m (lower and left axes).

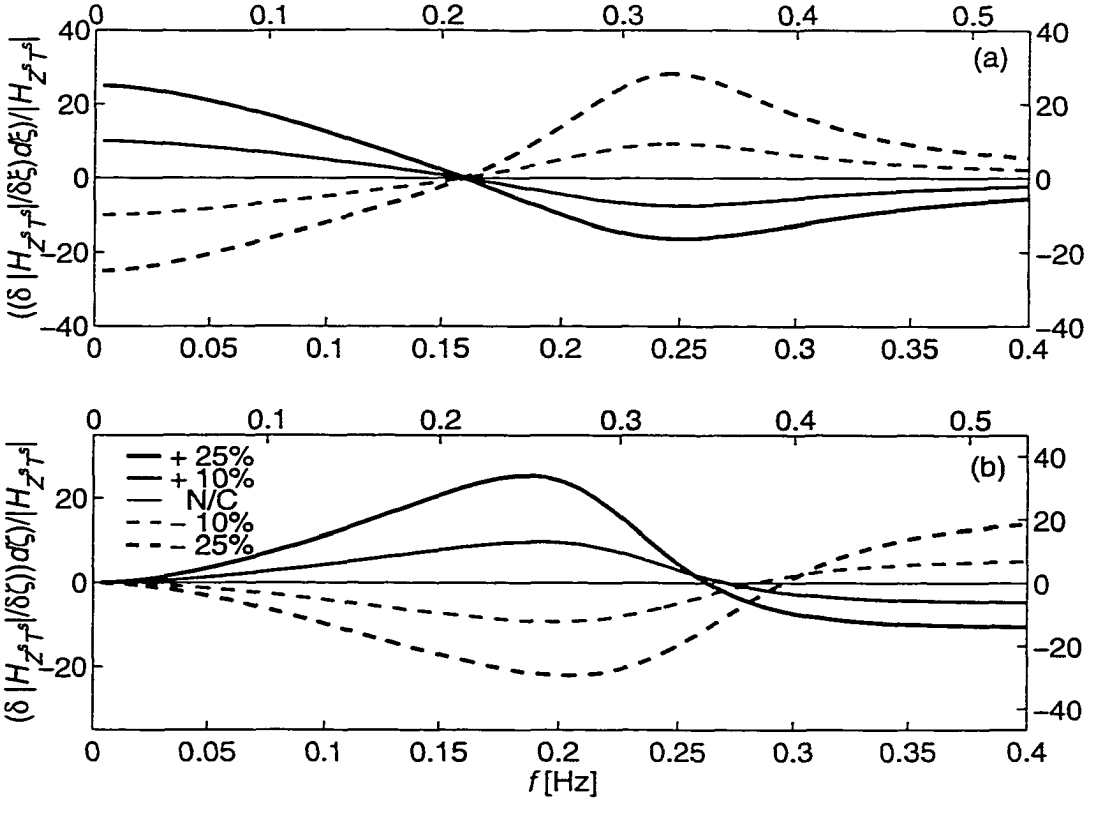

Fig. 9. Sensitivities of the magnitude of the transfer function between ship motion and tension in the tether (at the ship) to changes in the non–dimensional variable ξ (a) and ζ (b) for operating depths of 975 (upper and right axes) and 1 730 m (lower and left axes).

Appendix C

Development and Validation of a Lumped–Mass Dynamics Model of a Deep Sea ROV System

Development and Validation of a Lumped–Mass Dynamics Model of a Deep–Sea ROV System

F. R. Driscoll

Departments of Mechanical Engineering and School of Earth and Ocean Sciences, University of Victoria, Victoria, B.C., Canada. V8W 3P6

R. G. Lueck

Centre for Earth and Ocean Research, University of Victoria, B.C., Canada. V8W 3P6

M. Nahon

Department of Mechanical Engineering, University of Victoria, Victoria, B.C., Canada. V8W 3P6.

(*Submitted to Applied Ocean Research*)

We develop a one–dimensional finite–element lumped–mass model of a vertically tethered caged ROV system subject to surface excitation. Data acquired during normal operation at sea are used with a Least–Squares technique to estimate the coefficients required by the model. Our model correctly predicts a) the motion of the cage and the tension in the tether at the ship, b) the spectrum of cage acceleration in the wave–band, c) the transfer function between the vertical motion of the ship and cage, and d) the natural frequency of the system and its harmonics. A simple model of the wake of the cage was added to our simulation and this reduced the error in the calculated motion and tension by almost a factor of 2 and brought the calculated transfer function within the 95% confidence interval of the measurements. By increasing ship motion slightly, our model accurately reproduced eight snap loads and their non–linear characteristics – a regularly spaced series of rapid increases in the records of the acceleration of the cage and tension at the ship — that occurred during the measurements used for validation.

Key Words: Tethered marine systems, finite element analysis, offshore engineering, Remotely Operated Vehicle, snap loading, cable modelling.

INTRODUCTION

Caged remotely operated vehicles (ROVs) are robots that effectively operate in the dangerous high–pressure environment of deep water while their human controllers remain safely aboard the support ship (Figure 1). The tether connecting the ship and cage provides the ROV with the ability to stay at the underwater work site indefinitely and allows real–time communication with the ROV. However, the tether also couples the ship motion to the cage, and, as a result, these systems do not operate in rough seas. Rough seas cause slack tether, large snap loads and erratic cage motion[1] which damage the tether and its internal electrical and optical conductors. The resulting degradation reduces the life of the tether and endangers the recovery of the ROV. Many other vertically tethered systems are dynamically similar to caged ROVs, including CTDs (conductivity temperature and depth measuring platforms), drill strings, water sampling rosettes, tethered equipment being lowered to the ocean floor, and piston coring tools. Reliable tools are needed to predict the behaviour of vertically tethered systems so that designers can minimise motions and tensions and users can know which sea states will produce snap loads. In this paper, we develop a finite–element lumped–mass model of a vertically tethered caged ROV system and use it to predict the cage motion and tension in the tether for prescribed ship motion.

Two tools are available to predict the response of vertically tethered systems — continuous (closed-form analytic) and discrete models. Continuous models can be used to accurately calculate many of the dynamic characteristics of tethered systems, including motion and tension spectra, transfer functions, natural frequency and its harmonics, and

the onset of slack in the tether [2–4]. However, continuous models have limitations. Equivalent linearization techniques are used to approximate the quadratic drag for steady amplitudes which enables closed form solutions and frequency–domain analysis [3–5]. Thus, these models are not appropriate during unsteady wave conditions. Continuous models are also invalid for a slack tether, which is the precursor to snap-loads, and it is difficult (if not impossible) to solve the differential equations governing a tether when its properties change along its length. Discrete models are not constrained by the limitations of continuous models and they are valid for a wider range of operating conditions and system configurations. Niedzwecki and Thampi[6] developed a discrete multi–segment lumped–paramter representation of a drill string connecting a ship to a subsea package and used it to investigate snap loading. They reproduced many of the snap load and motion characteristics that were observed by Driscoll *et al*[1] for a real system, namely, a repeating pattern of rapidly increasing tension during snap loads and vertical motion at the platform that was greater than at the ship.

The predicted behaviour can be sensitive to the model coefficients, such as added mass[6], and choosing representative values is difficult because many components are complex and asymmetric (armoured/faired tether, ROV cages and Conductivity Temperature and Depth measuring platforms). For example, Yoerger *et al*[7] found that the normal drag coefficient of a long vertical tow cable is amplified well above the value for a rigid cylinder and that it depends on operating conditions. Therefore, coefficients must be calibrated using measured data to obtain confidence in a model. Additionally, discrete models are approximations to real systems, and therefore, validation against real data is essential in proving their accuracy and reliability. In our literature search, we found one

work that calibrates coefficients of a deep towed vehicle using data[7] and one that compares results of a discrete model of a towed system against its actual motion[8]. However, no work was found that uses data to calibrate and validate discrete models of vertically tethered systems.

In this paper, a finite–element lumped–mass model of a vertically tethered ROV system is developed by applying Galerkin's method to a continuous representation of the tether. Motion and tension measurements of the ROPOS ROV system[1] are used to accurately determine values for the model coefficients. In particular, a least-squares technique is used to estimate the drag coefficient and mass (including added and entrained mass) of the ROV cage. The vertical motion of the top element is prescribed with actual ship motion and our model is validated by comparing the calculated and measured motion of the cage and tension in the tether. A simple representation of the wake of the cage is also developed and its addition improves model accuracy. Finally, we compare the predicted and actual response during snap loads.

DISCRETE MODEL

For a typical deep–sea ROV system operating in the absence of time varying currents or large horizontal excursions of the support vessels, the ship and cage are only coupled vertically[1]. The displacement of the cage due to surge, sway, roll, pitch and yaw motions is small compared to the vertical scale O(1:1000) of the tether and such motions are not effectively transmitted by the tether. Therefore, a one–dimensional model is sufficient to represent a caged ROV system. For modelling purposes, the system is broken down into three individual sub–systems: the support ship with its A–frame, the

tether, and the cage and ROV. We use a finite–element lumped–mass model to represent the tether, a displacement function to prescribe the ship motion and a second order differential equation to represent the cage and ROV unit. The model is developed using a single inertial reference frame located at the mean sea surface, with downward displacements defined as positive.

Tether model

The tether is a long elastic structural member that can only sustain tensile loads and may have length–varying properties. We represent the tether as a long elastic cylinder that is suspended directly below the ship's A–frame. Defining s as the vertical unstretched co–ordinate along the tether, the balance of forces (per unit length) at any point in the tether is[9]:

$$\frac{\partial T}{\partial s} + W + F = ma \tag{1}$$

where

$$W = (\rho_c - \rho_w)Ag \tag{2}$$

is the *in situ* weight (per unit length), $T(s)$ is the tension in the tether, $F(s)$ is the hydrodynamic force, m is the effective mass (per unit length including entrained water), a is the inertial acceleration, g is the gravitational acceleration, $A(s)$ is the cross–sectional area of the tether, $\rho_c(s)$ is the density of the tether and ρ_w is the density of sea water. The added mass forces are zero for flow tangent to a cylinder[10], and therefore,

$F(s)$ is only composed of drag forces. The hydrostatic pressure induces circumferential and radial stress and a depth dependent axial strain in the amour strands of the tether[11]. The ratio of the standard deviations of the strain induced by the tension to the strain induced by the pressure at any point in the tether is 1000 because the tether only oscillates short vertical distances (< 3 m). Thus, hydrostatically induced axial strain is considered constant in time and it is neglected in our analysis. Assuming the water is stationary in the far field, $F(s)$ is[12]:

$$F(s) = -\frac{1}{2}\rho_w D(\varepsilon + 1) C_{DT} \dot{U} \left| \dot{U} \right| \tag{3}$$

where ε is the local strain in the tether, $D(s)$is the diameter of the tether, C_{DT} is the tangential drag coefficient, ($\dot{}$) represents a time derivative and $\dot{U}$ is the velocity of the tether. The relationship between tension and axial strain is:

$$T(s) = EA\varepsilon \tag{4}$$

where E is the effective Young's modulus of the tether.

We chose a finite–element implementation because it is versatile and can model the complicated non–linear characteristics of vertically tethered systems. For example, we can quickly assemble complex models of multi–component systems connected by tethers with different and length dependent properties because elemental tether equations are developed from a generalised linear-elastic tether subject to unspecified boundary conditions. Components, such as ROV cages, weights/floats, and intermediate platforms

can be easily added because they are each represented as a point mass and the hydrodynamic, gravitational and buoyancy forces acting on them are described by one differential equation.

The tether is discretised by first dividing it into N segments (elements) which have the same properties as the continuous tether. The end points of each element are the nodes of the system. Each element i is of length l_i and has an associated body–fixed reference frame attached to the upper node with the z axis pointing downward along the element. The top of the tether is attached to the ship's A-frame. To facilitate the finite–element derivation, the location of any point p in element i is defined using a coupled set of reference and elastic co-ordinates[13]:

$$z_i^p = Z + s_i^p + u_i^p \tag{5}$$

where Z is the position of the top, node 1, of the tether in the inertial frame, s_i^p is the constant length position vector from node 1 to a point p along the undeformed tether and u_i^p is the cumulative elastic displacement of the tether up to point p. We use an elemental trial solution, $\tilde{u}_i^p$[14], to approximate the elastic displacement, u_i^p:

$$u_i^p \approx \tilde{u}_i^p(s,t;\delta) = \sum_{j=1}^{n} \delta_i^{(j)}(t)\phi_{i.j}(s) \tag{6}$$

where $\phi_{i.j}(s)$ is a shape function and $\delta_i^{(j)}(t)$ is a time–dependent coefficient (yet to be defined). Each tether element has only one degree of freedom and a linear shape function

is sufficient to approximate the elastic displacement of any point p in element i, that is $n = 2$ and

$$\phi_{i,1}(s) = \frac{s_i^{(2)} - s}{s_i^{(2)} - s_i^{(1)}} \qquad \phi_{i,2}(s) = \frac{s - s_i^{(1)}}{s_i^{(2)} - s_i^{(1)}} \qquad \delta_i^{(1)} = u_1^{(1)} \qquad \delta_i^{(2)} = u_i^{(2)} \tag{7}$$

where $(\cdot)_i^{(1)}$ and $(\cdot)_i^{(2)}$ represent the upper and lower nodes of element i, respectively. The finite–element equations are obtained by applying Galerkin's method of weighted residuals[14] to the force balance equation of each element. Knowing that ρ_c and A are uniform or change very slowly ($\frac{l_i}{\rho_c}\frac{\partial \rho_c}{\partial s} << 1$ or $\frac{l_i}{A}\frac{\partial A}{\partial s} << 1$) along an element and that the strain in the tether is small ($\varepsilon << 1$), the elemental equations of element i are:

$$\frac{m_i l_i}{2}\begin{bmatrix}\ddot{Z}\\ \ddot{Z}\end{bmatrix} + m_i l_i \begin{bmatrix}1/3 & 1/6\\ 1/6 & 1/3\end{bmatrix}\begin{bmatrix}\ddot{u}_i^{(1)}\\ \ddot{u}_i^{(2)}\end{bmatrix} + \frac{E_i A_i}{l_i}\begin{bmatrix}1 & -1\\ -1 & 1\end{bmatrix}\begin{bmatrix}u_i^{(1)}\\ u_i^{(2)}\end{bmatrix} = \begin{bmatrix}f_i^{(1)}\\ f_i^{(2)}\end{bmatrix} + \begin{bmatrix}\beta_i^{(1)}\\ \beta_i^{(2)}\end{bmatrix} \tag{8}$$

where E_i is the effective Young's modulus of the tether and $\dot{s}_i = \ddot{s}_i = 0$. The hydrodynamic, gravitational and buoyancy forces at upper and lower nodes are:

$$f_i^{(1)} = 1/2\,(m_i - \rho_w A_i) g l_i - 1/2\,\rho_w D_i C_{DT}^i l_i \left(1/3\,(\dot{Z} + u_i^{(1)})\left|\dot{Z} + \dot{u}_i^{(1)}\right| + 1/6\,(\dot{Z} + \dot{u}_i^{(2)})\left|\dot{Z} + \dot{u}_i^{(2)}\right| - 1/12\,(\dot{u}_i^{(1)} - \dot{u}_i^{(2)})\left|\dot{u}_i^{(1)} - \dot{u}_i^{(2)}\right|\right)$$

$$f_i^{(2)} = 1/2\,(m_i - \rho_w A_i) g l_i - 1/2\,\rho_w D_i C_{DT}^i l_i \left(1/6\,(\dot{Z} + \dot{u}_i^{(1)})\left|\dot{Z} + \dot{u}_i^{(1)}\right| + 1/3\,(\dot{Z} + \dot{u}_i^{(2)})\left|\dot{Z} + \dot{u}_i^{(2)}\right| - 1/12\,(\dot{u}_i^{(1)} - \dot{u}_i^{(2)})\left|\dot{u}_i^{(1)} - \dot{u}_i^{(2)}\right|\right)$$

where D_i is the diameter of the tether and the boundary conditions for the continuity of strain between nodes of connecting elements at the upper and lower nodes, respectively are:

$$\beta_i^{(1)} = E_i A_i \frac{\partial \tilde{u}}{\partial s} \phi\left(s_i^{(1)}\right)_{i,1}$$

$$\beta_i^{(2)} = E_i A_i \frac{\partial \tilde{u}}{\partial s} \phi\left(s_i^{(2)}\right)_{i,2}.$$

Ship model

The vertical motion of the ship is assumed to be known and is treated as a prescribed displacement function applied to the upper end (first node) of the tether, $Z = Z_S(t)$. Because the motion of the first node is prescribed, measured (actual) ship motion data can be used as input. Thus, our model can be validated by directly comparing the calculated cage motion and tension in the tether against the actual values for the same ship motion.

Cage and ROV model

The cage and ROV are represented as a single point mass that is attached to the lower end of the tether and subject to the forces of gravity, buoyancy, drag and tension. The force balance at the cage is:

$$(M_{CG} + M_{ROV})(\ddot{Z} + \ddot{u}_N^{(2)}) + \frac{1}{2}\rho_w A_C C_D (\dot{Z} + \dot{u}_N^{(2)})\left|\dot{Z} + \dot{u}_N^{(2)}\right| = W_{CG} + W_{ROV} - T(L) \qquad (9)$$

where M_{CG} and M_{ROV} are the effective mass (including entrained and added mass) of the cage and ROV, respectively, C_D is the drag coefficient of the cage, A_C is the horizontal cross–sectional area of the cage, W_{CG} and W_{ROV} are the weight less buoyancy of the cage and ROV, respectively, and $T(L)$ is the tension in the tether at the cage termination. When the ROV is out of the cage, M_{ROV} and W_{ROV} are set to zero.

Model assembly

The N tether elements are assembled end–to–end and joined at their node points. Nodes are numbered consecutively from the top node, 1, to the bottom node, $N+1$. The second time derivative of the prescribed ship motion is the acceleration of node 1. The tether is contiguous at each node point ranging between 2 and N; therefore, the trial functions of connected elements points must be identically equal at connecting nodes. Additionally, continuity requires the strain boundary conditions of connected elements to be equal and opposite at coincident end point; therefore, the boundary forces, $\beta_i^{(2)}$ and $\beta_{i+1}^{(1)}$ cancel when the elemental equations are assembled. We include the cage and ROV by adding their mass to that of node $N+1$ and applying the forces acting on them to that node. The boundary condition at the bottom end of the tether is equal to (9). We replace the consistent–mass matrix with a lumped–mass matrix to uncouple the acceleration terms[15]. The set of N second order differential equations that govern the motion of the vertically tethered system are:

$$\ddot{Z} = \ddot{z}_1 = \ddot{Z}_S(t) \tag{10}$$

$$M\ddot{z} + Ku = f \tag{11}$$

where the lumped–mass matrix, $M \in R^{N\times(N+1)}$, is:

$$M = \frac{1}{2}\begin{bmatrix} 0 & m_1 l_1 + m_2 l_2 & 0 & \cdots & 0 & 0 \\ 0 & 0 & m_2 l_2 + m_3 l_3 & \cdots & 0 & 0 \\ \vdots & \vdots & \vdots & \ddots & \vdots & \vdots \\ 0 & 0 & 0 & \cdots & m_{N-1} l_{N-1} + m_N l_N & 0 \\ 0 & 0 & 0 & \cdots & 0 & m_N + 2M_{CG} + 2M_{ROV} \end{bmatrix}$$

the stiffness matrix, $K \in R^{N\times(N+1)}$, is:

$$K = \begin{bmatrix} -\frac{E_1 A_1}{l_1} & \frac{E_1 A_1}{l_1} + \frac{E_2 A_2}{l_2} & -\frac{E_2 A_2}{l_2} & \cdots & 0 & 0 \\ 0 & -\frac{E_2 A_2}{l_2} & \frac{E_2 A_2}{l_2} + \frac{E_3 A_3}{l_3} & \cdots & 0 & 0 \\ \vdots & \vdots & \vdots & \ddots & \vdots & \vdots \\ 0 & 0 & 0 & \cdots & \frac{E_{N-1} A_{N-1}}{l_{N-1}} + \frac{E_N A_N}{l_N} & -\frac{E_N A_N}{l_N} \\ 0 & 0 & 0 & \cdots & -\frac{E_N A_N}{l_N} & \frac{E_N A_N}{l_N} \end{bmatrix}$$

the external force matrix, $f \in R^{N\times 1}$, is:

$$f = \begin{bmatrix} f_1^{(2)} + f_2^{(1)} \\ f_2^{(2)} + f_3^{(1)} \\ \vdots \\ f_{N-1}^{(2)} + f_N^{(1)} \\ f_N^{(2)} + f_{CG} \end{bmatrix} \qquad f_{CG} = W_{CG} + W_{ROV} - \frac{1}{2}\rho_w A_C C_D (\dot{Z} + u_N^{(2)})\left|\dot{Z} + u_N^{(2)}\right|$$

and the position, $z \in R^{N\times 1}$, and displacement, $u \in R^{N\times 1}$, vectors are, respectively:

$$z = \begin{bmatrix} z_1 \\ z_2 \\ z_3 \\ \vdots \\ z_N \\ z_{N+1} \end{bmatrix} = \begin{bmatrix} Z \\ Z + s_2^{(1)} + u_2^{(1)} \\ Z + s_3^{(1)} + u_3^{(1)} \\ \vdots \\ Z + s_N^{(1)} + u_N^{(1)} \\ Z + s_N^{(2)} + u_N^{(2)} \end{bmatrix} \qquad u = \begin{bmatrix} 0 \\ z_2 - s_2^{(1)} - Z \\ z_3 - s_3^{(1)} - Z \\ \vdots \\ z_2 - s_N^{(1)} - Z \\ z_{N+1} - s_N^{(2)} - Z \end{bmatrix}$$

where $s_1^{(1)}$ and $u_1^{(1)}$ are zero.

Numerical implementation

The N second order differential equations given by (10) and (11) are rewritten as $2N$ first order differential equations, thus allowing the use of a conventional ODE integration routine. We use a Runge-Kutta fourth-fifth order numerical integration routine with adaptive step size which takes small time steps during periods of rapid change and large time steps when changes are slow[16]. This method provides good accuracy with only moderate computational effort.

CALIBRATION

The utility of any dynamic model lies in its ability to accurately predict the response to specified input. We collected data for the ROPOS ROV system while it operated at depths of up to 1 730 m and use these data to accurately determine the unknown coefficients, to verify manufacturer's specifications and to validate our numerical model. ROPOS is a large ROV that dives to 5 000 m, and is attached to the cage by an umbilical tether. The cage itself weighs 49 000 N in air and has dimensions of 2.1 m × 3.4 m × 4.2 m (WLH) and is connected to the ship by a triple armoured tether

that is 0.03 m in diameter, 4 200 m long and weighs 30.5 Nm^{-1} in air. The motion was measured at the ship's A–frame directly above the sheave that supports the tether (and thus, at the first node), and at the cage. The tension in the tether was measured at the sheave on the A–frame. For all measurements used, the ROV was out of the cage, and thus, M_{ROV} and W_{ROV} are set to zero.

Values for most of the model's coefficients are difficult to determine. The cage is a three–dimensional bluff body with two planes of symmetry and complex geometry. Its drag coefficient, C_D and added mass (included in M_{CG}) cannot be accurately determined using empirical values of coefficients for bodies of simple geometry. The linear stiffness, EA, of the tether is difficult to estimate because the tether consists of an inner core of several different materials surrounded by layers of armour strands that are counter–helically wound. Thus, we use experimental data to determine accurate values of the coefficients.

We determined the weight less buoyancy of the tether, W (per unit length), and cage, W_{CG}, from a least–squares linear fit of tension to depth for the range of 218 to 1 730 m. Tether deployment was halted (steady length) for each measurement. The slope W and offset W_{CG}, (Table 1) agreed well with the manufacturer's specifications. The mass of the tether is approximated by its dry mass plus the mass of the water entrained into the void space between the strand of armour. The wet mass is 2% larger than the dry mass (Table 1).

The mass and drag coefficients of the cage are determined by expressing (9) as:

$$W_{CG} - T(L) = M_{CG}(\ddot{Z} + \ddot{u}_{N+1}^{(2)}) + \frac{1}{2}\rho_w A_C C_D (\ddot{Z} + \dot{u}_N^{(2)})\left|\dot{Z} + \dot{u}_N^{(2)}\right| \qquad (12)$$

We did not measure $T(L)$ but we do know that it is well approximated by $T(0)$ for $L \leq 100$ m. For $L \geq 100$ m, the phase and magnitude of $T(L)$ and $T(0)$ are different[1] and therefore records for these greater depths cannot be used. Equation 12, is linear in the unknown coefficients; therefore, a least–squares fit to the records from 28 and 32 m depth provides values and 95% confidence internals of $M_{CG} = 7\,750 \pm 160$ kg and $C_V^{CG} = \frac{1}{2}\rho_w A_C C_D = 8\,150 \pm 170$ kgm^{-1}. The statistical error is less than 1% but the different values for the two depths imply a bias and systematic error of 2% and we use this larger value as our confidence interval.

The axial stiffness, EA, is given by (DLN–2):

$$EA = mc^2 \ . \qquad (13)$$

where c is the speed of strain waves along the tether. As will be shown in the discussion (Figure 6), echoes of a snap load are spaced at constant intervals equal to the travel time of a strain wave through the length of tether, and thus they provide a very precise measure c for large L. A second measure of c is provided by the higher order natural frequencies which are spaced at intervals of $0.5c / L$ Hz. Both methods yield identical values of $c = 3870$ ms^{-1}. Using this value in (13) we find that the axial stiffness is $EA = 45.5 \pm 1.4 \times 10^6$ N.

VALIDATION

Our model is validated by directly comparing the real and simulated motion of the cage and tension in the tether for the same forcing at the top node. We validated the model for several depths, but for brevity we will focus on operation at 1 730 m. Numerical results are calculated using 50 elements and the estimated coefficients (Table 1). The motion of node 1 is prescribed by a 5 000 s time series of ship motion that was *not* used to estimate the coefficients.

The model provides a very good approximation of the actual displacement of the cage (Figure 2). The displacement of the cage is about 50% greater and lags behind that of the ship. This particular section of data has a large range of amplitudes and includes a snap load which starts at $t = 627$ s. The larger amplitudes are underestimated by the model and the snap (sudden change of acceleration at the cage) was not reproduced. Quantitatively, the standard deviation of the difference between the simulated and measured position of the cage (tension at the ship) is $\sigma_{diff}^{Z^C} = 0.11$ m ($\sigma_{diff}^{T^S} = 4\,000$ N) and the ratio of $\sigma_{diff}^{Z^C}$ ($\sigma_{diff}^{T^S}$) to the rms of the measured values is 0.12 (0.28).

The spectra (the distribution of variance with frequency) of the real and simulated vertical cage acceleration are compared for the same 5 000 s record of ship motion (Figure 3). The model with wake is addressed in the discussion. The frequency domain analyses will focus on the *wave–band* that extends from 0.1 to 0.25 Hz because this band contains 90% of the variance of ship motion. The real and simulated spectra agree well within the wave–band at 1 730 m — the largest difference is 13% at 0.14 Hz and the

spectra are equal at 0.175 Hz. For $L = 975$ m (not shown) the real and simulated spectra are almost identical and the largest difference is only 7% at 0.14 Hz. Above 1 Hz, significant excitation is only produced by the impulsive snap loads and no wave excitation is transferred to the tether because the large inertia and length of the ship low–pass filter the short (high–frequency) waves.

The cage is a bluff body, subject to quadratic drag, and thus produces variance at odd harmonics of the fundamental frequency of excitation, 0.15 Hz (the peak of the spectrum in Figure 3). The third and fifth harmonics are evident at 0.44 and 0.73 Hz (Figure 3). Our model over predicts the variance at those frequencies; however, the system remains weakly non–linear[1] because the harmonics only contributed a small fraction to the total variance. For example, at 1 730 m, the variance at the harmonics provided only 4.6 and 0.3% of the total variance of the cage acceleration.

The transfer function estimate (TFE) provides a measure of the motion amplification and phase difference between the ship and cage and it is estimated using:

$$H_{z^s z^c} = \frac{C_{z^s z^c}}{C_{z^s z^s}}$$

where $C_{z^s z^c}$ is the cross–spectrum of ship–displacement, Z^S, and cage–displacement, Z^C, and $C_{z^s z^s}$ is the auto–spectrum of Z^S. We restrict our analysis of the TFE to the wave–band (0.1 – 0.25 Hz) because the error in the real TFE is large and the modelled cage response is not significant at higher frequencies. At 1 730 m, agreement between the real and simulated TFE is good up to 0.2 Hz at 1 730 m and the largest difference in

magnitude is only 8% at 0.13 Hz. The model over predicts the cage response at the higher frequencies within the wave. The simulated phase is always slightly larger than the real phase and the maximum difference is 15° at 0.2 Hz (near the middle of the wave–band). These discrepancies are attributed, in part, to the assumption of a constant drag coefficient and a constant added mass of the cage which is not completely accurate for oscillatory flow around a bluff body. This issue is addressed in the discussion. At 975 m, the magnitude and phase of the TFE agree exceptionally well — the largest differences are 0.05 (4%) at 0.19 Hz and 10° at 0.25 Hz.

The depth dependent natural frequencies, f_n, provide another characteristic to validate our model. The predicted and observed first natural frequency (indicated by the first 90° phase shift of $H_{z^s z^c}$ (Figure 4)) agree within 7%. Although very little excitation occurs above 1 Hz, the model exactly predicts the second, third, and fourth natural frequencies at 1.17, 2.24 and 3.36 Hz (Figure 3).

SENSITIVITY

During the design process, the model coefficients are not accurately known; therefore, our model output must be reasonably insensitive to variations of its coefficients to be a useful design tool. Nine coefficients are used in our model: N, L, M_{CG}, m, C_V^{CG}, C_{DT}, W_{CG} W, and EA where L is the deployed length of tether. The tether drag can be ignored because the ratio of tether–to–cage drag is 0.06. Gravitational and buoyancy forces only affect the static solution, and the dynamic response of the system in the wave–band is independent of the number of elements used when $N > 5$ (this will be

addressed in the Discussion). Thus, only five coefficients affect the dynamic response of the model: L, M_{CG}, m, C_V^{CG}, and EA. In previous work[4], we have shown that the non-dimensional transfer function between ship and cage motion is only a function of two non–dimensional parameters, namely:

$$\frac{C_V^{CG}}{mc}, \qquad \frac{M_{CG}}{mL}$$

when the frequency is non–dimensionalized with:

$$\omega' = L\sqrt{\frac{m}{EA}}\omega = \frac{L}{c}\omega$$

where ω' is the non–dimensional frequency. Therefore, there are only three independent parameters that characterise the dimensional response and we only need to examine the dependence of the model on C_V^{CG}, M_{CG}, and EA. We do this by calculating the relative changes in the magnitude and the absolute changes of the phase of the transfer function between vertical motions of the ship and cage for variations of C_V^{CG}, M_{CG}, and EA, of $\pm$ 15% about their nominal values (Figures 5). The sensitivities of the TFE to EA look similar to those of M_{CG} but the magnitude and phase do not scale. The dotted line is the difference between the real and calculated TFE (using the nominal coefficient values) and is addressed in the Discussion.

In the mid to upper wave band ($0.15 \leq f \leq 0.25$ Hz), the changes in the TFE are, at most, of the same order as the changes in the coefficients and the magnitude is most

sensitive to C_V^{CG} while the phase is most sensitive to EA. In the lower wave–band, ($f <$ 0.15 Hz) the magnitude and phase of $H_{z^s z^c}$ are not sensitive to of EA, M_{CG}, and C_V^{CG}. Therefore, reasonably accurate predictions of the magnitude and phase of the transfer function can be obtained using "rough" estimates of EA, M_{CG}, and C_V^{CG}. As in our continuous model[4], the sensitivities of the phase are zero at 0.25 Hz (0.22 Hz in^4) and the phase is independent of M_{CG}; and between 0.22 and 0.23 Hz (0.21 and 0.23 in^4) the magnitude of $H_{z^s z^c}$ is only slightly sensitive to variations in C_V^{CG}. Also notable is that the signs of the sensitivities are preserved between our continuous and finite–element models.

The bounds of uncertainty for the estimated values of M_{CG}, C_V^{CG} and EA are less than 5% and thus all their probable values are contained within the ±15% sensitivities. At most frequencies in the wave–band, the difference between the real and calculated TFE (the dotted line in Figure 5) is much larger than the ±15% sensitivities; therefore, the model results cannot be significantly improved with realistic changes in M_{CG}, C_V^{CG} and EA. Additionally, because the sensitivities change sign (either in magnitude and phase) at different frequencies (not coincident with the error) we cannot expect that changes in M_{CG}, C_V^{CG} and EA will improve the predictions at all frequencies within the wave–band.

DISCUSSION

Calculations were significantly reduced by replacing the consistent–mass matrix with the lumped–mass matrix which uncouples the acceleration terms in the elemental equations. We also calculated the motion of the cage and tension at the ship using the

consistent–mass representation with 50 elements and the same 5 000 s record of ship motion. Results from the two representations are identical. Noticeable differences only occur when a small number of elements (< 5) is used. For example, predictions of the second harmonic of the natural frequency differ by 0.26 and 0.06 Hz for a two element and a three element model, respectively.

The run time of our simulation increases quadratically with the number of elements and, therefore, we want to use as few elements as possible. In our model, the mass of each element is "lumped" at its nodes and, as a result, the mass distribution and (therefore) the accuracy of the static results increases with increasing elements. However, the dynamic motion of the cage and tension at the ship were found to be nearly independent of the number of elements for predictions within the wave–band. Thus, the practical considerations for the lower bound of N are as follows. The prediction of zero tension (snap loads) depends on the total (static + dynamic) tension in the tether and, therefore, a fine element break–up is required. An N–element model can only predict up to N natural frequencies and the accuracy of the predicted values increases by increasing N.

We have characterized the hydrodynamic forces on the cage in terms of a drag coefficient multiplied by the speed and velocity. Although this formulation is common practice, there are several reasons to be suspicious. The velocity of the cage is unsteady and it is both positive and negative. For steady external (far from the body) flows, the drag coefficient changes with changing speed because of variations in the point of boundary layer separation and the pattern of recirculation over the body and in its wake.

The boundary layer and wake of an accelerating body that has reached a given speed are never the same as those over the same but non-accelerating body at that speed. In addition, the boundary layer during acceleration is not the same as during deceleration (for the same speed). The motion history becomes an important factor in determining the drag forces on the body. These and many other aspects of unsteady flow past bluff bodies (mainly cylinders) are discussed in Sarpkaya and Isaacson[17].

The inertial forces on the cage have been represented by its acceleration multiplied by its effective mass. This, too, is common practice but this formulation obscures the physics of unsteady flow around bluff bodies and only makes sense if the relative rate of change of velocity is small and the drag coefficient is not sensitive to small changes in Reynolds number. The notion of added mass becomes simplistic when the relative change of velocity is large and when the velocity changes direction because the history of the flow becomes important. For example, the added mass can momentarily become negative when vortices detach from the body during acceleration and very large when they reattach during deceleration. A key parameter of oscillatory flow is the ratio of amplitude of travel to the length scale of the body and this ratio was always less than 0.6 for the cage examined here. In this parameter range, the notion of added mass is reasonable for cylinders[17] and the good predictions of the discrete model indicate that this notion is also judicious for the ROPOS cage. The concept of an added mass will be less effective for larger ratios of amplitude to length scale. Thus, we cannot expect hydrodynamic forces on the cage to be represented, with complete accuracy, by a single drag coefficient and a single added mass.

The sensitivity analysis indicates that differences between measured and modeled motions cannot be explained by parameter uncertainty. The differences may be due to the limitations of the concept of single drag coefficient and a single added mass. To test this notion, we added a simple wake model that makes some account of the history of motion. Our objective is to motivate additional work on the unsteady forces on bluff bodies attached to tethers rather than to promote this particular model. We assume that, at each time step, the water directly behind the cage (on its lea side) has the same velocity as the cage. We track the position of these water parcels and assume that their momentum decays exponentially with time. When a water parcel overtakes the cage (typically when the cage decelerates) we add an additional force to the lea side that is proportional to the velocity difference between the cage and this parcel. The decay time for momentum is 2.9 s and was chosen by trial and error. The corresponding length scale is 2.9 m for typical speeds and is comparable to both the height of the cage and the maximum amplitude of motion.

Including the wake model significantly improves the results of our model for operation at 1 730 m. The standard deviation of the difference between the calculated and measured position of the cage (tension in the tether) is improved by a factor of 1.6 (1.8) and it is $\sigma_{diff}^{Z^C} = 0.07$ m ($\sigma_{diff}^{T^S} = 2\,200$ N) vs 0.11 m (4 000 N) for the model without wake. The new ratio of $\sigma_{diff}^{Z^C}$ ($\sigma_{diff}^{T^S}$) to the rms of the measured values is 0.08 (0.16) (Figure 3). The calculated and real spectrum and transfer function (both magnitude and phase) between ship and cage motion are nearly identical, and the agreement in the upper wave–band is notably improved (Figure 3). The error in the magnitude (phase) of the

TFE is reduced from 0.12 (15°) to 0.07 (7°), respectively. Surprisingly, addition of the wake model reduces the non–linearity of the predicted response and brings the predicted spectrum of acceleration at the third and fifth harmonic of the fundamental frequency of excitation into close agreement with the measured spectrum. Similar improvements were found for an operation depth of $L = 975$ m.

Motion during a snap load is non–linear and different from that during normal operation. Large and rapid downward displacements of the ship produce slack tether at the cage. A snap load results when the tether is re–tensioned because the velocities of the tether and cage are different. The induced strain wave travels along the tether with speed c and it is reflected at its ends (the ship and cage). This results in a series of rapid changes of cage acceleration (jerks) and tension at the ship and these changes are spaced at intervals equal to the round trip travel time of strain waves[1].

Snap loads occurred in less than 1% of the motion cycles in the 5 000 s record we used to validate our model. Such threshold conditions are very difficult to predict because they require the numerical model to be very precise. Without the wake model, our simulation underestimated the large displacement and did not reproduce the slack tether — the minimum tension was 10 000 N. With the inclusion of the wake model, the calculated motion only slightly underestimated the large vertical displacement and the tension in the tether at the cage approached zero. However, zero tension was still not achieved and snap loads were not predicted. Therefore we increased the ship motion by 10% so that slack tether would result and we could investigate the response of our model to this condition. Under these conditions, our model reproduced the observed snap loads

and the associated acceleration and tension profiles (Figure 6). The rapid changes of acceleration and tension aligned with the measured values and agreed in magnitude. Most notable is that the slope of the real and calculated acceleration is nearly identical at the first jerk. We therefore conclude that our discrete model inherently has the ability to produce characteristics associated with snap loads. A more realistic representation of the drag and added mass could improve the prediction of slack tether so that threshold conditions of snap loading could be better predicted.

CONCLUSIONS

We developed a one–dimensional finite–element lumped–mass model of a caged remotely operated vehicle system using a coupled set of reference and elastic co-ordinates. The elastic displacements were approximated with a linear trial solution. Using Galerkin's method, we discretised the equation for the balance of forces at any point in the tether and assembled the resulting elemental equations to obtain the finite–element equations of motion for the system. The resulting model is a function of only nine coefficients: N, L, M_{CG}, m, C_V^{CG}, C_{DT}, W_{CG} W, and EA, when tether has constant properties along its length.

Values of the model coefficients were estimated using motion and tension measurements of the ROPOS ROV system. Although many of the coefficients are readily estimated, it is very difficult to determine accurate values of the mass, M_{CG}, and drag coefficient, C_V^{CG}, of the cage and the stiffness of the tether, EA. A least–squares method was used to determine values for M_{CG} and C_V^{CG} to an accuracy of 2% of their real values.

The stiffness, EA, was determined to 3% accuracy using the speed of tensile waves in the tether, c, which was estimated from the time of successive tension maxima during a snap load. These methods are useful because they only used data acquired during normal operation of the ROV system and did not require any special procedures.

We prescribed the vertical motion of the top node using measurements of ship motion and validated our model by comparing the output against the corresponding measurements of cage motion and tension at the ship. Our model accurately predicts a) the motion of the cage and the tension in the tether, b) the spectrum of cage acceleration in the wave–band, c) the transfer function between the vertical motion of the ship and cage, and d) the natural frequency and harmonics of the system.

Sensitivities to the three independent parameters of the model indicate that the mismatch between the simulated and real motion cannot be significantly improved by adjusting the values of those parameters. However, inclusion of a simple wake model improved the agreement between the real and calculated results by almost a factor of 2. Eight snap loads also occurred in the measurements used to validate our model; however, these were only threshold occurrences. Using the wake model and increasing the ship motion by 10%, our model predicted the observed snap loads and accurately reproduced their characteristics — rapid increases in the acceleration/tension record that are spaced at regular intervals equal to the travel time of the strain wave along the length of deployed tether.

ACKNOWLEDGEMENTS

We would like to thank Jim McFarlane and the staff of International Submarine Engineering (ISE) for their continual support and assistance in this project. We would also like to thank Inna Sharf for sharing her expertise in finite–element modelling and Nedjib Djilali for sharing his expertise in fluid dynamics. F.R. Driscoll was financially supported by scholarships from the Natural Science and Engineering Research Council (NSERC), the Science Council of British Columbia (SCBC) and ISE. This work was partially supported by the US Office of Naval Research under contract N00014–93–1–0362 and NSERC .

REFERENCES

1. Driscoll F.R., Lueck R.G. and Nahon N., The motion of a deep–sea remotely operated vehicle system. Part 1: motion observations, *Ocean Engineering,* in press, (1999).

2. Hover, F.S., Grosenbaugh, M.A., and Triantafyllou, M.S., Calculation of dynamic motions and tensions in towed underwater cables. *IEEE Journal of Oceanic Engineering*, **19** (1994), 449-457.

3. Grosenbaugh, M.A. On the dynamics of oceanographic surface moorings, *Ocean Engineering*, **32** (1996) 7–25.

4. Driscoll F.R., Lueck R.G. and Nahon N., The motion of a deep–sea remotely operated vehicle system. Part 2: analytic model, *Ocean Engineering*, in press, (1999).

5. Caughey, T.K., Equivalent linearization techniques, *Journal of the Acoustic Society of America*, **35** (1963) 1706–1711.

6. Niedzwecki, J.M. and Thampi, S.K., Snap loading of marine cable systems, *Applied Ocean Research*, **13** (1991) 210–218.

7. Yoerger, D.R. Grosenbaugh, M.A. Triantafyllou M.S. and Burgess, J.J., Drag forces and flow–induced vibrations of a long vertical tow cable — Part 1: steady–stead towing conditions, *Journal of Offshore Mechanics and Arctic Engineering*, **113** (1991) 117-127.

8. Hover, F.S. and Yoerger, D.R., Identification of low–order dynamics models for deeply towed underwater vehicle systems, *International Journal of Offshore and Polar Engineering*, **2** (1992) 38-45.

9. Ablow, C.M. and Schechter, S. 1983, Numerical simulation of undersea cable dynamics, *Ocean Engineering*, **10** (1983) 443–457.

10. Newman, J.N., *Marine Hydrodynamics*, The MIT Press, Cambridge Massachusetts, 1989.

11. Sparks, C.P., The influence of tension, pressure and weight on pipe and riser deformations and stresses, *Transactions of the ASME*, **106** (1984) 46-54.

12. Folb, R. and Nelligan, J.J., Hydrodynamic Loading on Armoured Towcables, DTNSRDC report 82/116, 1983.

13. Shabana, A.A., *Dynamics of Multibody Systems*, John Wiley & Sons, New York, 1989. pp. 470

14. Burnett, D.S., *Finite Element Analysis From Concepts to Applications*, Addison-Wesley Publishing Company, Don Mills, Ontario, 1987. pp. 844

15. Logan, D.L., *A First Course in the Finite Element Method*, PWS-KENT Publishing Company, Boston, 1992, pp. 662

16. Press,W.H., Teukolsky, S.A., Vetterling, W.T. and Flannery, B.P., *Numerical recipes in C, second edition*, Cambridge University Press, Cambridge, 1992.

17. Sarpkaya, T. and M. Isaacson, 1981, *Mechanics of wave forces on offshore structures*. Van Nostrand Reinhold, New York, pp. 651

18 Robigou, V., *Journal of Geophysical Research Letters*, **20** (1993), Cover Page

Coefficient	Value
m	3.01 ± 0.06 kg m^{-1}
W	25.4 ± 0.5 N m^{-1}
W_{CG}	$43\,200 \pm 1000$ N
EA	$45.5 \pm 1.4 \times 10^6$ N
C_{DT}	0.02
C_V^{CG}	$8\,150 \pm 170$ kg m^{-1}
M_{CG}	7750 ± 160 kg

Table 1: Values of the model coefficients estimated using motion and tension measurements of the ROPOS ROV system.

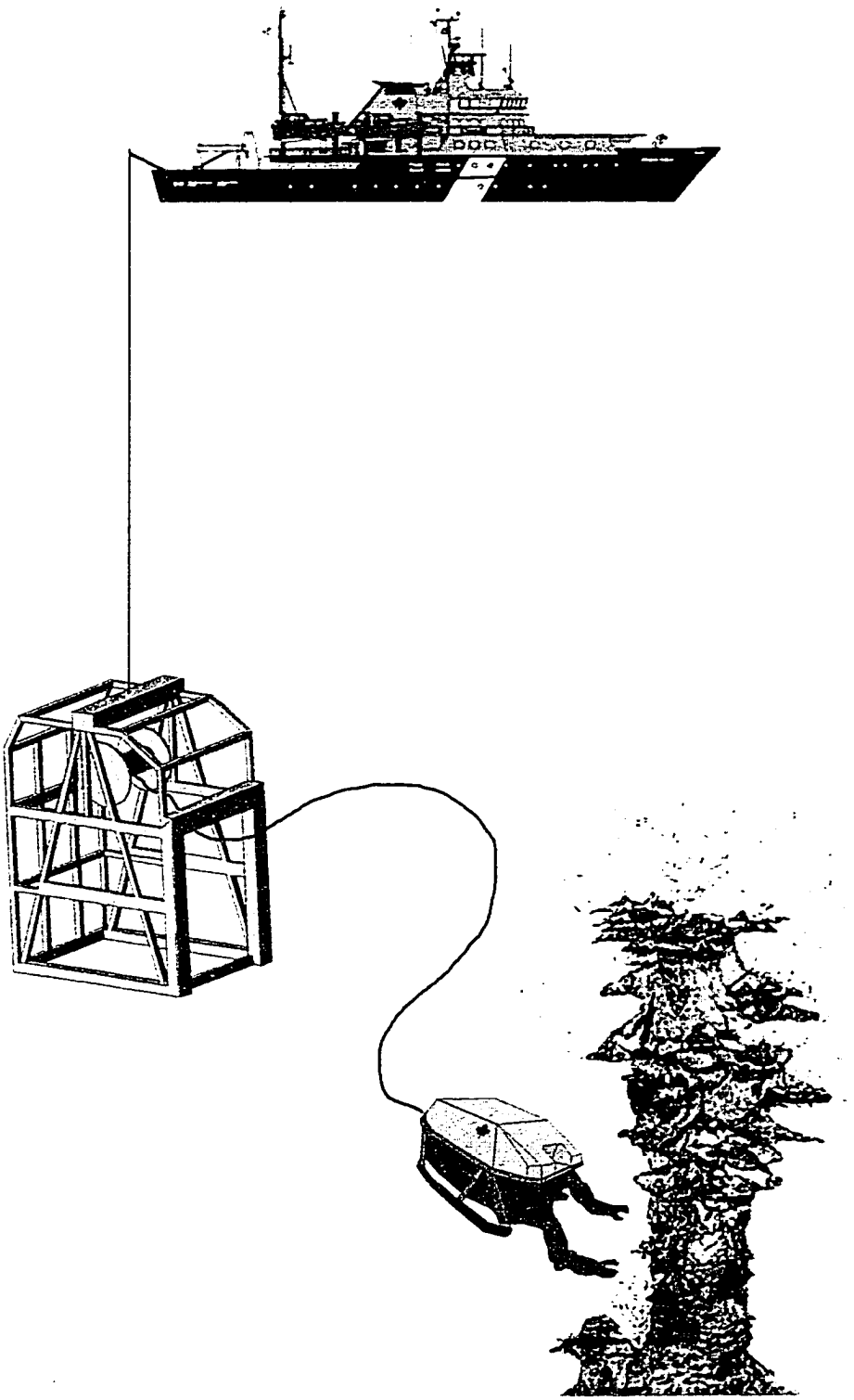

Fig 1. Diagrammatic representation of the ROPOS ROV system consisting of a support ship (C.S.S. John P. Tully), winch, umbilical tether, cage and vehicle. ROPOS is investigating the actively-venting sulfide structure Godzilla[18]

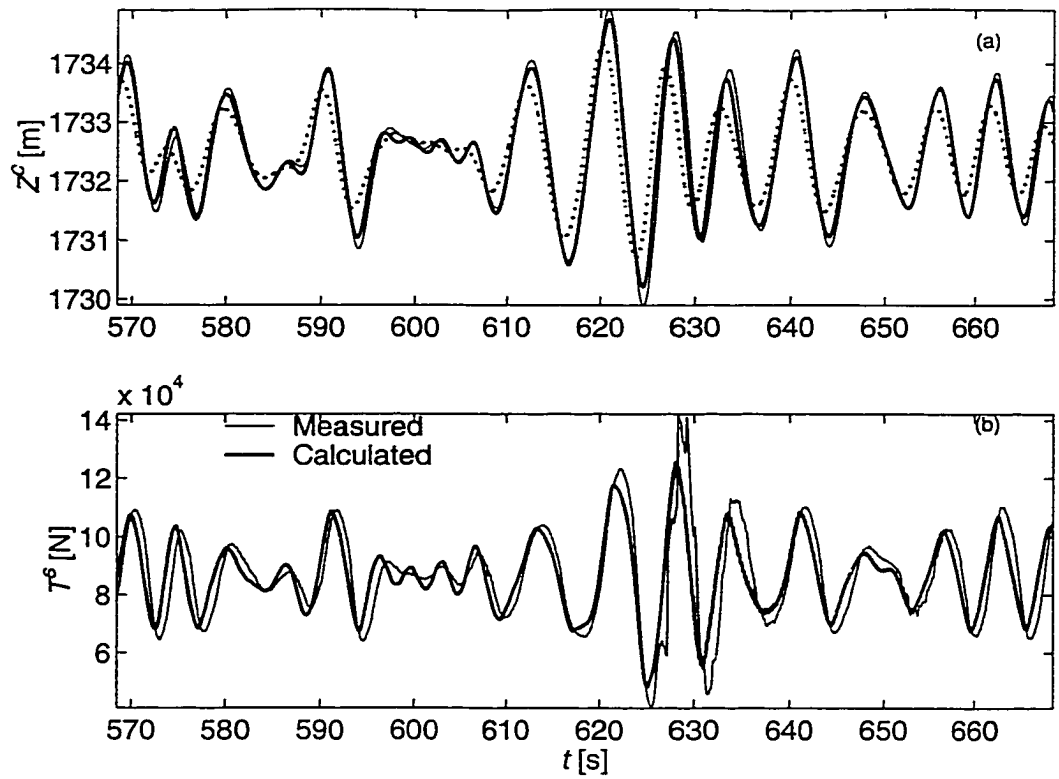

Fig 2. Short time series of calculated (thick line) and measured (thin line) cage motion and tension in the tether for the system at 1 730 m. The ship motion (dotted line) is included for comparison.

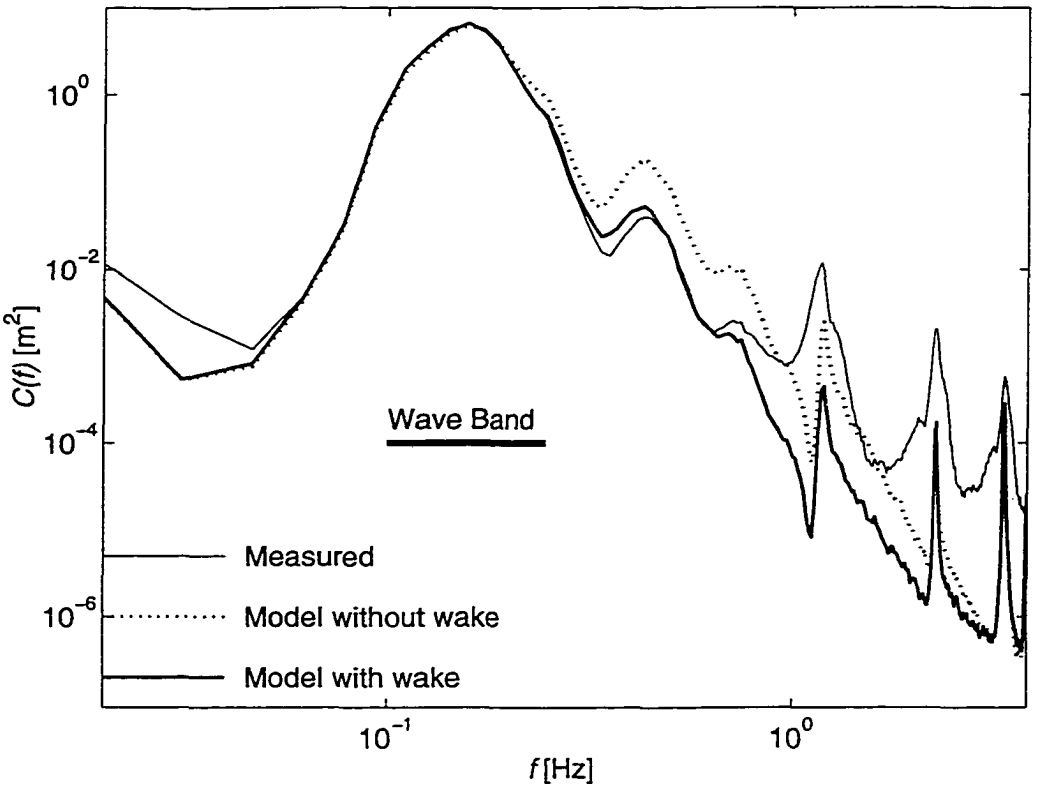

Fig. 3. Spectra of actual (thin solid line) and model calculated (dotted line – without wake, thick solid line – with wake) vertical acceleration records of the cage at a depth of 1 730 m. The arrows are the 3rd and 5th harmonic of the peak cage motion and the natural frequency.

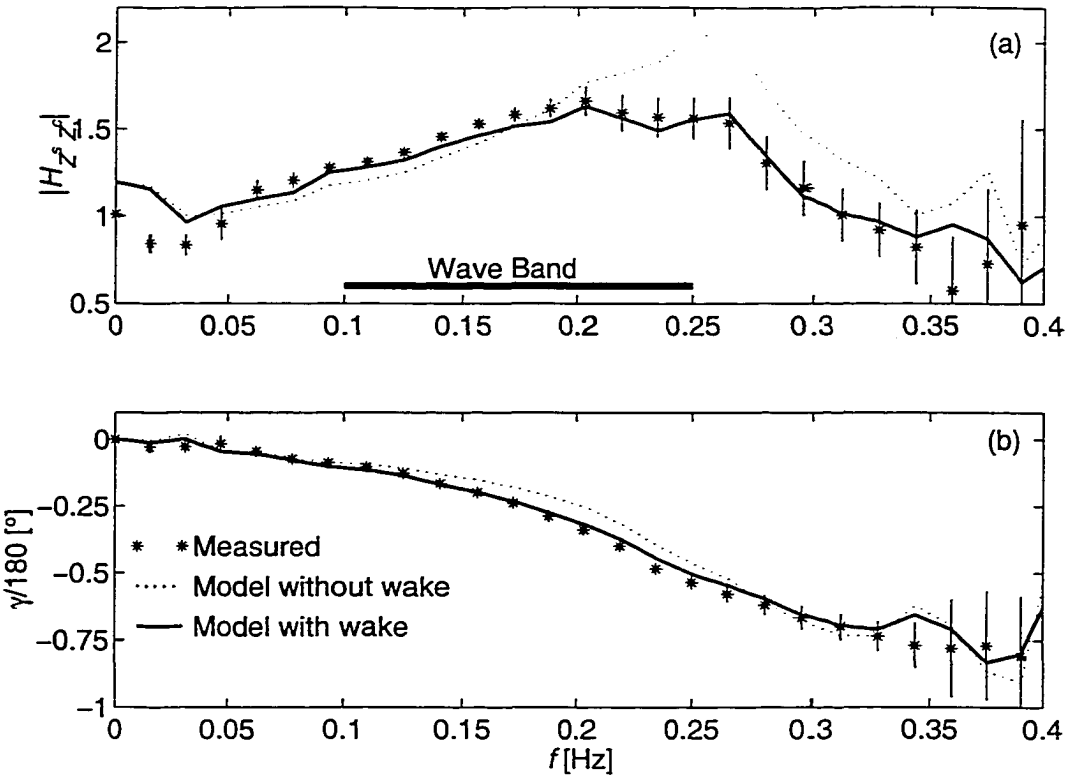

Fig. 4. Magnitude (a) and phase (b) of the actual (stars) and calculated (dotted line – without wake, solid line – with wake) transfer function estimate between the ship and cage motion at a depth of 1 730 m.

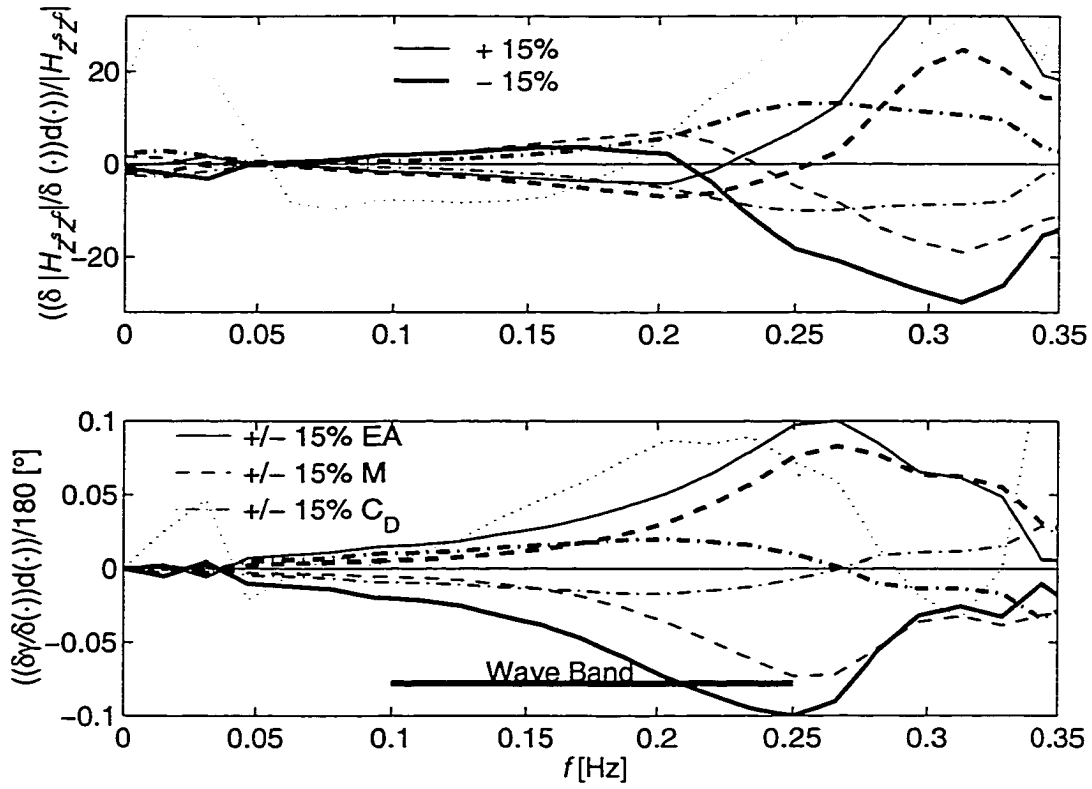

Fig. 5. Sensitivities of the magnitude (a) and the phase (b) of the transfer function between ship and cage motion to changes in M_{CG} (thin solid line), C_V^{CG} (dashed line), and EA (thick solid line) for operating depth of 1 730. The dotted line is the difference between the actual and simulated TFE.

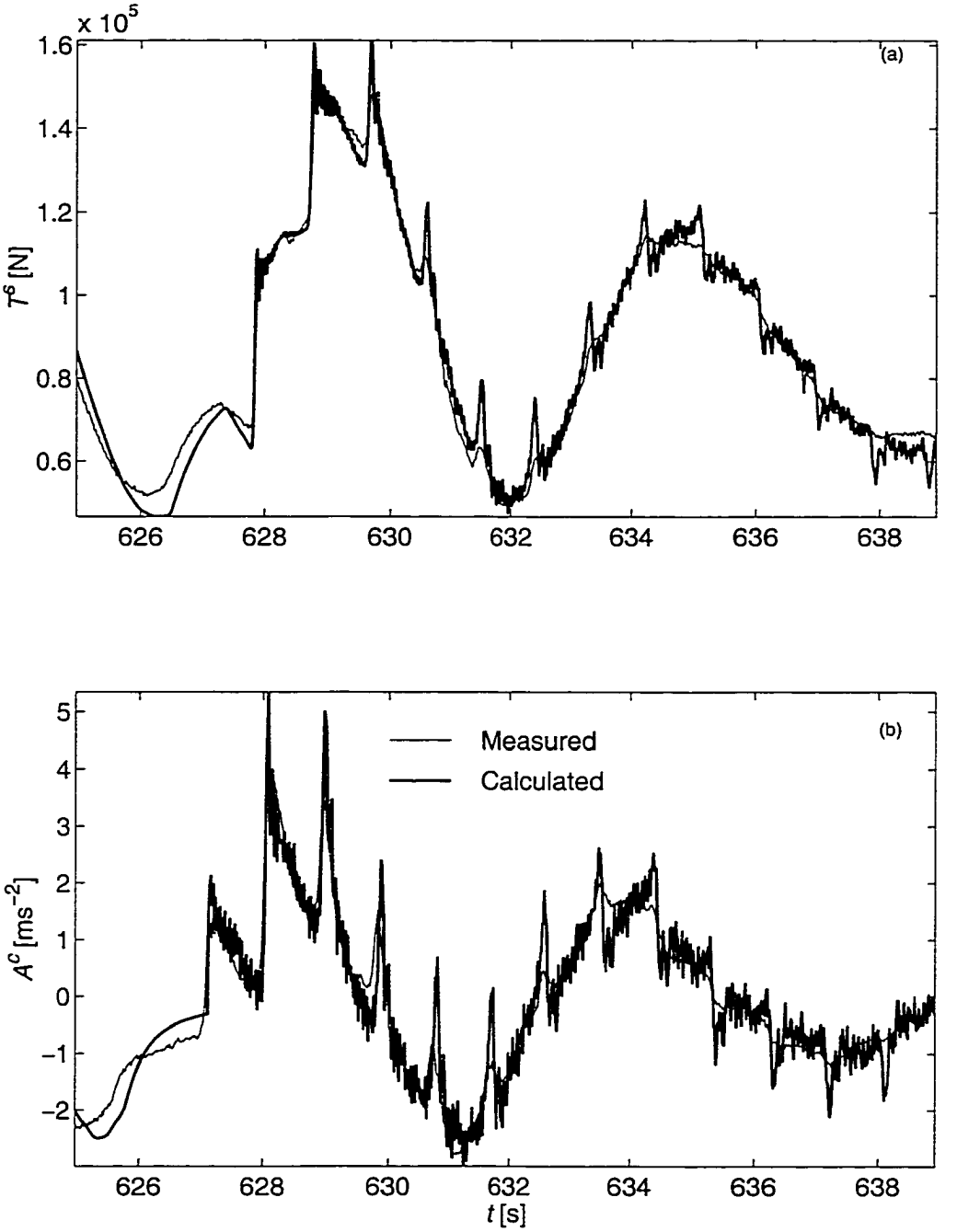

Fig. 6. Measured (thin line) and calculated (thick line) records of the tension in the tether at the A–frame (a) and acceleration of the cage (b) during a snap load.

Appendix D

A Comparison of Ship–Mounted and Cage–Mounted Passive Heave Compensation Systems

A Comparison of Ship–Mounted and Cage–Mounted Passive Heave Compensation Systems

Frederick R. Driscoll

Department of Mechanical Engineering and School of Earth and Ocean Sciences, University of Victoria, P.O. Box 3055, Victoria, British Columbia, V8W 3P6, Canada, tel: (250) 721-6080, fax: (250) 721-6051, rdriscol@uvic.ca

Meyer Nahon

Department of Mechanical Engineering, University of Victoria, Victoria, , P.O. Box 3055, Victoria, British Columbia, V8W 3P6, Canada, tel: (250) 721-6040, fax: (250) 721-6051, mnahon@uvic.ca

Rolf G. Lueck

Centre for Earth and Ocean Research, University of Victoria, , P.O. Box 3055, Victoria, British Columbia, V8W 3P6, Canada, tel: (250) 721-8918, fax: (250) 721-6195, rlueck@uvic.ca

(*Submitted to the Journal of Offshore Mechanics and Arctic Engineering*)

Tethered marine systems experience large tensile loads in their tether when operating in rough seas. Heave compensation systems can be used to reduce these loads and increase the safe operating sea states. In this work, a discrete representation of a passive heave compensator is developed and added to a finite–element model of a deep sea ROV system to investigate the performance of ship–mounted and cage–mounted compensation systems. Numerical simulations are performed for operating depths ranging from 3 280 *to* 16 400 *ft* (1 000 *to* 5 000 *m*) *and a range of compensator stiffnesses. Both ship and cage–mounted systems reduced the natural frequencies, rms cage motion and rms tension, and extended the operating sea state of the ROV. During extreme seas, the cage–mounted compensator eliminated all snap loads. However, the compensator's characteristics must be carefully chosen because a poorly designed compensator can exacerbate operational problems.*

1 Introduction

A remotely operated vehicle (ROV) can remain at its underwater work site indefinitely and can effectively and interactively accomplish tasks in dangerous environments while its human operators remain safely onboard the support ship. These advantages over autonomous underwater vehicles and manned submersibles are possible because an umbilical cable connects the ROV to the support ship. Typical tethers consist of outer layers of steel or kevlar armour that house an inner core of electrical and optical conductors that are used to power and communicate with the ROV. Operation in rough seas results in slack cable and snap loading which can damage the tether's structural armour and its internal conductors. This degradation reduces the life of the cable and endangers the recovery of the ROV (Driscoll et al., 1999a and Niedzwecki and Thampi, 1991) and it interrupts communication and power which renders the vehicle inoperable. When caged (or clumped mass) ROV systems operate in rough seas, large vertical displacements of the cage can occur. In most cases, the ROV is attached to the cage by a slack neutrally buoyant tether, and it remains vertically stationary in the water while the cage oscillates. This makes docking difficult, if not impossible. If the cage and vehicle collide during a docking attempt, structural damage can result to both units. In this paper we investigate the ability of two different systems to alleviate these problems: a semi–active ship–mounted and a passive cage–mounted compensation system.

The operational problems of deep–sea ROV systems in rough seas are dangerous and expensive. Thus, any heave compensation system which could alleviate these problems would be of great benefit. For example, during an experiment in which we

measured the ship and cage motion and the tension in the tether to validate our numerical model (Driscoll *et al*, 1999a), the system operation was severely limited by rough weather. In particular, during a two week interval at sea only five hours of useful operation were logged; the main umbilical tether had to be re–terminated because the optical conductors were broken by many snap loads; and the tether connecting the cage and ROV was sheared during a docking attempt due to the large vertical motion of the cage. In subsequent analysis, we determined that this uncompensated deep–sea ROV was in resonance at depths greater than 4750 ft (1450 m) and the resulting cage motion was greater than that of the ship (Driscoll *et al.* 1999a and 1999b). Ideally, an effective heave compensation device should reduce the vertical motion of the cage to make docking of the ROV easier, eliminate snap loading and decrease the rms and peak tension in the tether. If these benefits are achieved, heave compensation will increase the operating range and operating life of the ROV system.

Much effort has been focussed on the effective design of actively controlled heave compensation systems to reduce the heave motion and dynamic tension of drill string and tethered systems (Korde, 1998, Kerstein, 1986, Bennet and Forex, 1997 and Gaddy, 1997). For active systems to work well, the dynamic characteristics of the overboard system must be well known to chose appropriate values of the depth dependant gains. Additionally, active systems are complex and require significant support equipment. Recently, a few works have looked at passive ship–mounted heave compensation systems because of their simplicity. Both Hover et al. (1994) and Niedzwecki and Thampi (1988) presented excellent analyses of passive systems. Hover investigated a ship–mounted system for a deeply towed body by varying the values of the compensator's linear

stiffness and damping over a range of sea states at a single operating depth. Niedzwecki and Thampi used a lumped parameter model to investigate a ship–mounted pneumatic system with linear stiffness for a large hard rock drilling base suspended by a series of drill strings. In both of these works, the authors found that appropriate values of compensator stiffness must be chosen or the motion and tension at the end of tether may be increased in specific sea states. The potential benefits of a system mounted on the undersea platform have been overlooked and we did not find any work that investigates the effectiveness of a cage mounted system.

In this paper, a lumped parameter heave compensation element is developed and included in our existing finite–element lumped–mass model (Driscoll *et al.*, 1999c) to investigate the effectiveness of ship–mounted and cage–mounted pneumatic heave compensation systems. A passive design is used at the cage; while a semi–active design is needed at the ship to adjust for the depth dependent static tension in the tether. We investigate the attenuation of the cage motion and tension in the tether (at the A–frame) for a range of operating depths and compensator travel.

2 Design of heave compensators

ROVs are sophisticated multifaceted systems and a heave compensation system would add an additional level of complexity. To minimise this, we focussed our analysis on a passive design because of its simplicity. Passive systems are virtually autonomous requiring little, if any, external support. They have few components, all of which are relatively simple and easy to maintain. By comparison, semi–active and actively controlled systems must be supported by external equipment including computers,

sensors, data acquisition systems, motors, compressors, and hydraulic systems and may also require human intervention. Because of their complexity, these systems can be expensive and difficult to maintain.

The overboard weight less buoyancy of an ROV system can increase by several times between surface and its maximum depth of operation (e.g. by a factor of 4 for the ROPOS ROV system (Remotely Operated Platform for Oceanographic Science) an International Submarine Engineering Hysub 5000, ISE 1998). Therefore, a ship–mounted system must be strong and it must compensate for the changing weight less buoyancy of the overboard system using some level of active control. By contrast, a cage–mounted compensator only supports the weight less buoyancy of the cage and it can be completely passive because the static tension at the cage termination is constant. Thus, if a cage–mounted system is effective, it is a desirable alternative to a ship–mounted heave compensation system.

For this investigation, we chose a ram–tensioner utilising a pneumatic spring as our heave compensation mechanism (Fig. 1). On the high pressure side, the spring is connected to a constant volume accumulator and the low pressure side is evacuated. The unequal pressure acting on the opposing faces of the piston creates a force that balances the inertial, hydrodynamic and gravitational forces of the supported system. In static equilibrium, the piston is stationary, approximately mid way between its end stops. When the ship heaves up (down), tension in the tether increases (decreases) and the piston moves toward the high (low) pressure end which increases (decreases) the pressure and feeds tether out (in). This has two benefits: it reduces the motion of the supported system

and thereby, the dynamic loading (inertial and hydrodynamic forces) in the tether is also reduced. The end stops (not shown in Fig. 1) are large springs of equal stiffness and when the compensator is fully retracted, the outer spring brings the tension to zero. A linear damping mechanism is also used in conjunction with the pneumatic spring.

The tension-displacement curves of the pneumatic spring are determined by modelling the thermodynamic compression and expansion. The pneumatic spring cycles at wave frequencies (0.1 to 0.25 Hz) and the gas temperature only changes by 10% over ambient for the maximum change in volume investigated. Thus, the operation of the spring is well approximated by an adiabatic relationship because compression and expansion are fast enough that heat transfer is negligible. The irreversible (friction)–to–reversible work ratio is very small — 1:200 for a typical cycle and the spring is considered to be isentropic. Thus, the thermodynamic relationship governing the compression and expansion of our pneumatic spring, using an ideal gas, is (Moran and Shapiro, Chapter 6, 1992):

$$PV^n = \text{constant} \tag{1}$$

where P is the pressure, V is the volume of the gas contained in the spring, and n is the ratio of specific heats of the gas. An accumulator is used to increase the volume of the system in order to obtain the desired tension–displacement characteristics of the spring. Its volume is determined by specifying the tension range of the compensator. If we specify the median tension to be the supported weight, W_T, and the extreme tension just

prior to hitting the end stops to be $W_T \pm kW_T$, we find from (1) that the accumulator volume must be:

$$V_R = \frac{A_P \Delta_T}{\left(\frac{1+k}{1-k}\right)^n - 1} \tag{2}$$

where k is specified as a fraction of W_T, A_P is the area of the piston, and Δ_T is the total compensator travel. The non–linear tension–displacement relationship of the compensator is given by:

$$T_{HC} = \frac{W_T(1+k)}{\left(\left(\frac{1+k}{1-k}\right)^{\frac{1}{n}}\left(1-\frac{\delta}{\Delta_T}\right)+\frac{\delta}{\Delta_T}\right)^n} + C_{pd}\dot{\delta} \tag{3}$$

where the first and second terms are the stiffness and damping components of the tension, respectively, δ is the compensator displacement (line pay out), C_{pd} is the linear damping constant, and $(\dot{})$ represents a time derivative. The tension–displacement curve due to the first term of (3) is non–linear and its slope represents the heave compensator's stiffness. This relationship is shown in Fig. 2 for $k = 0.2$ and $k = 0.4$. For constant k, the stiffness (slope of the tension–displacement curve) increases with decreasing Δ_T. Conversely, for a given value of Δ_T, the effective stiffness will increase with increasing k. Because the tension increases non–linearly with increasing compensator displacement, the static equilibrium position is not located at $\Delta_E = 0.5\Delta_T$ but rather at:

$$\Delta_E = \frac{(1+k)^{\frac{1}{n}} - \left(\frac{1+k}{1-k}\right)^{\frac{1}{n}}}{\left(1-\left(\frac{1+k}{1-k}\right)^{\frac{1}{n}}\right)}\Delta_T . \tag{4}$$

For example, we find that if $k = 0.4$ and $n = 1.4$, then $\Delta_E = 0.67\Delta_T$. The system pressure at static equilibrium is determined by $P_{eq} = A_P W_T$.

3 Dynamics Simulation

In previous work, we developed a finite–element lumped–mass model of an ROV system without heave compensation (Driscoll et al., 1999c) and it was validated against experimental measurements. For example, Fig. 3 shows a comparison of model and experimental results for the vertical position of the cage and the tension in the tether at the ship. Thus, we only provide here a brief overview of that model. The model is developed using a single inertial reference frame located at the mean sea surface, with downward displacements defined as positive. The vertical motion of the A–frame is assumed to be known and is modelled as a prescribed displacement function applied to the upper end of the tether. The tether is broken down into several visco–elastic elements which are connected at their node points (end points, Fig. 4). The mass (including entrained water) of each element is "lumped" equally at its node points. Applied at each node are the forces due to the viscous drag, internal strain, internal damping, weight, and buoyancy that act on/in the connecting elements. The tension–strain relationship of each element is assumed to be linear. The first node of the cable is attached to the A–frame and its motion is therefore prescribed. The cage is modelled as a point mass attached to

the last node of the tether and is subject to gravitational, buoyancy, and viscous drag forces.

The formulation of this discrete–element lumped–mass representation allows a compensation device to be easily incorporated into our model as an additional element inserted at any location. For this work, we insert a compensator element at either the top or bottom element, to represent either a ship–mounted or a cage–mounted compensation system, respectively. The effect of the compensator is modelled as a force applied to the connecting nodes. The discretized force equation for a compensator element i with a pneumatic spring and a linear damper is:

$$f_{HC}^{(1)} = \frac{W_T(1+k)}{\left(\left(\frac{1+k}{1-k}\right)^{\frac{1}{n}}\left(1-\frac{z_i^{(2)}-z_i^{(1)}}{\Delta_T}\right)+\frac{z_i^{(2)}-z_i^{(1)}}{\Delta_T}\right)^n} + C_{pd}\left(\dot{z}_i^{(2)}-\dot{z}_i^{(1)}\right) \tag{5}$$

and

$$f_{HC}^{(2)} = -f_{HC}^{(1)} \tag{6}$$

where $z_i^{(1)}$ and $z_i^{(2)}$ are the vertical location of the upper, $^{(1)}$, and lower, $^{(2)}$, nodes of the compensator element i, respectively. The mass of the compensator is lumped with the mass of either the cage or the ship, for cage–mounted and ship–mounted configurations, respectively.

The complete model consists of $N+1$ nodes, where N is the number of elements. The motion of each node point is governed by a second order differential equation. Since the motion of the first element is prescribed, the system is completely described by a set of N simultaneous second order differential equations. The temporal response is calculated by rewriting the N second order equations as a set of $2N$ first order equations and using a fourth-fifth order Runge–Kutta technique with adaptive step size to numerically integrate this initial value problem (Press et al., 1992).

4 Results – Normal Operating Conditions

We investigate the ship–mounted and cage–mounted pneumatic heave compensation systems for the ROPOS (Remotely Operated Platform for Oceanographic Science) ROV system. ROPOS is a deep sea ROV system (an International Submarine Engineering Hysub 5000 (ISE, 1998)) which is capable of diving to 16 400 ft (5 000 m). The cage weighs 11,000 lbf (49 000 N) in air and has dimensions of $6.9 \times 11.2 \times 13.8$ ft ($2.1 \times 3.4 \times 4.2$ m) (WLH). The tether has three layers of steel armour, is 1.17 in (3 cm) in diameter, weighs 2.1 lbf/ft (30.5 Nm^{-1}), and has a maximum working load and breaking strength of 45 000 lbf (200 000 N) and 123 5000 lbf (550 000 N), respectively.

Our finite–element model is used to evaluate the performance of the pneumatic heave compensation systems at three different depths, 3 280, 8 200, and 16 400 ft (1 000, 2 500 and 5 000 m) which span the operating range of the ROPOS ROV system in caged mode. For each of these depths, separate analyses are performed for the compensator

located at the cage and at the ship. The motion of the top node is prescribed with ship motion which we measured during field operation (Driscoll *et al*, 1999a).

In this investigation the stiffness of the compensators is specified by choosing values for the range of travel, Δ_T, and the tension range of the compensator, k. Only two values of k are used: one for the cage and one for the ship. In each case, the value of k is determined by:

1. calculating the response of the uncompensated system;

2. determining the average standard deviation of the tension in the tether at the A–frame and at the cage for all three depths;

3. setting k so the tension range of the compensator is ± one "average" standard deviation of the tension at the mounting location.

This results in $k = 0.2$ for ship–mounting and $k = 0.4$ for cage–mounting. The stiffness of the compensator is varied by investigating a wide range of travel of the compensator Δ_T = 10 to 65.6 ft (3 to 20 m) at each of the two mounting locations and three operating depths. For each set of Δ_T and k, we use the value of damping constant, C_{pd}, that minimises the rms motion of the cage at mid operating depth.

4.1 Time Domain Results

Both the ship–mounted and cage–mounted systems attenuate the deviations of the tension and the vertical cage motion about their mean (Fig. 5). The ship–mounted system

provides slightly better reduction of both tension and displacement. Large downward displacements of the ship produce slack tether at the cage in the uncompensated system. A snap load results when the tether is re–tensioned because the velocities of the tether and cage are different. Between 620 and 635 s, a snap load occurs in the uncompensated system (evident from the spiky tension record in that region). In all compensated cases investigated, the snap load is eliminated and the tension during that time interval is markedly reduced.

A measure of the effectiveness of the compensation systems is provided by the rms reduction ratio. For a new signal X and the original signal Y, the rms reduction ratio is:

$$R = \frac{\sigma_X}{\sigma_Y}$$

where σ_X and σ_Y are the standard deviation of X and of Y, respectively. For a compensator to be effective, R must be less than one, and smaller values of R indicate greater attenuation. We chose the rms reduction ratio because it provides an average measure of the effectiveness of the heave compensated systems over the range of simulated ship motions. However, depending on the specific emphasis, other criteria such as the reduction of extrema may be more appropriate. For the tension range, k, specified, the ship–mounted compensation systems is slightly more effective than cage–mounted systems — most values of the rms reduction ratios of the vertical motion of the cage, R_{Z^c}, and tension in the tether at the ship, R_{T^s} for the ship–mounted systems are less than

the corresponding values for the cage–mounted systems (Fig. 6). The greatest attenuation in cage motion is achieved for the 8 200 ft (2 500 m) cases.

At all depths except 16 400 ft (5 000 m), the effectiveness of the ship and cage mounted compensators increase with decreasing compensator stiffness — values of R_{Zc} and R_{Ts} decrease with increasing compensator travel, Δ_T. However, returns are diminishing because $d^2R_{Zs}/d\Delta_T^2$ and $d^2R_{Ts}/d\Delta_T^2$ are both positive. As a result, R_{Ts} itself begins to increase when $\Delta_T > 16.4$ ft (5 m) with cage–mounted compensation at 16 400 ft (5 000 m) and this will be addressed in the discussion. At all other depths, $dR_{Ts}/d\Delta_T < 0$. The tether did not go slack in any of the compensated cases investigated and no snap loads are predicted. In fact, the minimum tension in the tether at the cage increases with increasing Δ_T and increasing operating depth.

4.2 Frequency Domain Results

The spectra of cage acceleration and the transfer function between ship and cage motion provide a measure of the attenuation of cage motion at different frequencies. Due to space limitations, we only present the frequency domain information for the ROV at 8 200 ft (2 500 m) and $\Delta_T = 16.4$ ft (5 m). The variance of the vertical acceleration of the cage is much smaller for the compensated systems than for the uncompensated system (Fig. 7(a)). The variance preserving spectra with a linear vertical scale (Fig. 7(b)) clearly show that the compensated systems significantly reduce cage motion within the wave–band — the narrow frequency band between 0.1 and 0.25 Hz that contains 90% of the variance of ship motion. Again we see that the ship compensator is slightly more

effective than the cage–mounted compensator. In the other cases at different depths and different values of Δ_T, the spectra are very similar and the variance decreased with increasing Δ_T.

The transfer function between ship and cage motion, $H_{z^s z^c}(f)$, is a measure of the motion transferred between the ship and cage at different frequencies. When $|H_{z^s z^c}(f)| > 1$, the motion transferred at that frequency is amplified, when $|H_{z^s z^c}(f)| < 1$, the motion transferred is attenuated. As is evident in Fig. 8(a), motion amplification occurs through most of the wave–band for the uncompensated system. As well, $|H_{z^s z^c}(f)|$ of the uncompensated system is asymmetric about the system's first natural frequency, f_1 — the frequency at which the phase between forcing and response first passes through 90° (Fig. 8(b)). Also, the magnitude of the transfer function peaks at a slightly lower frequency than f_1 and decreases much more rapidly on the high frequency side of the peak frequency than on the low frequency side. Because of this asymmetry, more motion is transferred from the ship to the cage for frequencies below f_1 than for frequencies above f_1.

Addition of the passive heave compensation systems is equivalent to inserting an elastic member between either the ship and tether, or the cage and tether, which reduces the stiffness of the system and its natural frequencies. The resulting asymmetry of $|H_{z^s z^c}(f)|$ increases and it peaks at a much lower frequency than for the uncompensated case (Fig. 8(a)). For both ship and cage–mounted compensators at a depth of 8 200 ft

(2 500 m) and Δ_T = 16.4 ft (5 m), $\left|H_{z^s z^c}(f)\right|$ peaks below the wave–band and is less than one through most of the wave–band (Fig. 8(a)). The response remains similar at other depths with a slight improvement for shallower operation. The other variants investigated (i.e. other values of Δ_T) are also effective and reduced $\left|H_{z^s z^c}(f)\right|$ within the wave–band.

Although the peak of the transfer function at a depth of 8 200 ft (2 500 m) and Δ_T = 16.4 ft (5 m) is outside the wave band, it is larger than that for the uncompensated system and it is within the frequency range of swell (fully developed surface ocean waves), between 0.02 and 0.12 Hz. This implies that the system's response to swell will increase with the addition of either heave compensation system.

4.3 Compensator Travel

The heave compensator's range of travel, Δ_T, must be sufficient so that the piston does not hit its end stops during normal operation. If the piston collides with its upper end stop, the system may be impulsively loaded, similar to a snap load. With our choice of k, the piston in either compensator never reaches its upper or lower travel limits (Fig. 9) during typical operating conditions. However, for a smaller total range of travel, Δ_T = 9.8 ft (3 m), both ship and cage–mounted compensators use their full range of travel and the pistons will likely collide with their end stops if the sea state increases. At the other extreme when the total range of travel is large, Δ_T = 65.6 ft (20 m), the compensators use only a fraction of Δ_T. If this is true for the maximum operating sea conditions, the range of travel should be reduced while maintaining the desired stiffness. This is done by

appropriately choosing the minimum and maximum operating tension of the compensators. An interesting phenomenon occurs as Δ_T increases: the total range the cage–mounted compensator travels (Fig. 9(c)) increases while that of the ship–mounted compensator asymptotically approaches 11.5 ft (3.5 m). This point is addressed further in the discussion.

5 Results – extreme operating conditions

Storms can develop in short periods of time and rapidly increase sea conditions. An ROV system can take many hours to recover when working at full depth. It is therefore necessary to ensure that a heave compensation system does not exacerbate operating problems when the sea state unexpectedly increases above a specified maximum. To simulate storm sea states, we increase the record of ship motion by a factor of two and three. The significant A–frame displacement, S_A, is defined here as the average amplitude of the 25% largest displacements, analogous to the classical definition of significant wave height. The measured displacement of the A–frame used has S_A = 7.2 ft (2.2 m), and the records amplified by factors of two and three have S_A = 14.4 ft (4.4 m) and S_A = 21.7 ft (6.6 m), respectively. We then evaluate the ship and cage–mounted compensators with Δ_T = 16.4 ft (5 m) because these give a good compromise between performance, complexity and size in the prior results.

Under these conditions, the uncompensated system suffers from many snap loads at 8 200 ft (2 500) m (Fig. 10) with increasing severity for the larger ship motion, S_A = 21.7 ft (6.6 m) (Fig. 11). By including heave compensation, snap loading is

eliminated for S_A = 14.4 ft (4.4 m) and the pneumatic compensator never reaches its end stops. For S_A = 21.7 ft (6.6 m), slack regularly develops in the tether at the cage termination and the compensators hit their end stops. The cage–mounted compensator is compliant so subsequent re–tensioning is gradual and snap loads are not produced (Fig. 12). Rapid re–tensioning and snap loads do occur in the ship compensated system. However, in comparison to the uncompensated system, the time interval of slack is smaller and therefore, the relative velocity between the cage and tether and the resulting "snap" are reduced. When the compensators hit their upper end stops the system is impulsively loaded and rapid increases in tension, analogous to a snap load, develop, but are less in magnitude than the uncompensated snap loads. More weight is supported by the ship–mounted compensator than the cage–mounted system and thus, the jerks in the ship compensated system are larger when collisions with the end stops occur. By decreasing the compensator's stiffness while keeping Δ_T constant at 16.4 ft (5 m) we find that the compensator hit the end stop with higher velocity than for compensators with higher values of the stiffness. This results in larger impulsive loads.

6 Discussion

An effective heave compensation system must reduce the rms motion of the undersea platform and the rms tension in the tether at all operating depths and during typical sea states. Also, effective systems should operate well in extreme sea states. Values for the stiffness and damping parameters of passive compensation systems cannot be changed during operation. Therefore, if passive systems are to be effective, values of

parameters must be chosen to achieve the best balance between performance during normal operation (depth and sea state) and extreme sea states.

Our results show that both ship and cage compensated systems are effective in the operating range of 3 280 (1 000) to 16 400 ft (5 000 m). The best reduction in cage motion and tension in the tether is achieved for the mid operating depth of 8 200 ft (2 500 m). This occurs for two reasons. First, the damping is optimised for this depth. Second, the uncompensated system is in resonance and the variance of vertical motion transferred to the cage is maximised at this depth — the spectral peak of ship motion, the natural frequency, and the frequency of the peak of the transfer function between ship and cage motion all align. Effectively, this is a worst case scenario for the uncompensated system. At 3 280 (1 000) and 16 400 ft (5 000 m), the first natural frequency and peak the of the transfer function of the uncompensated system shift to higher and lower frequencies, respectively, which reduces the motion of the cage and tension in the tether. Addition of the heave compensators shifts the peak of the transfer function to below the wave–band for all depths between 3 280 (1 000) and 16 400 ft (5 000 m) and resonance never occurs. Thus, the largest reduction in motion and tension due to compensation occurs at 8 200 ft (2 500 m) because this is when the motion of the cage is the largest in the uncompensated system.

Intuitively, one would think that the effectiveness of any compensation system would improve by decreasing the compensator's stiffness. Taken to the limit, an infinitely compliant system would achieve a constant tension system and keep the cage stationary by uncoupling the ship and cage. However, this is not necessarily true. For example, at

16 400 ft (5 000 m), when Δ_T of the cage mounted compensator is increased above 16.4 ft (5 m) (the stiffness is decreased), R_{Ts} begins to increase, even though f_1 and R_{Zc} continue to decrease (Fig 6). To understand this phenomenon, there are three locations that must be investigated, the ship, the bottom end of the tether and the cage. As the stiffness of the cage–mounted compensator decreases, the ship and bottom end of the tether begin to oscillate in phase while the cage begins to oscillate out of phase. Also, the rms motion of the bottom end of the tether increases above the rms cage motion of the uncompensated system. As the relative motion between the bottom end of the tether and the cage increases, the minimum and maximum travel of the compensator and tension in the tether also increase (Fig 9 and 6, respectively). This phenomenon results because the second natural frequency is moving into the wave–band and thereby exciting the second natural mode of the system.

In addition to exciting higher natural modes, compliant (less stiff) compensators may also suffer during severe sea states. For example, compliant compensators travel larger distances at higher velocities than stiff compensators. Consequently, for similar Δ_T, compliant systems are more likely to hit their end stops and do so with a higher velocity. These collisions impart large impulsive loads to the system. Thus, compliant compensators will require a large range of travel to ensure they do not reach their end stops in rough sea states or when their second natural mode is excited. Clearly, a compliant system does not provide the best balance between performance during normal and extreme operation.

For a reasonable range of total travel and stiffness ($\Delta_T \leq 19.7$ ft (6 m)) that achieves a good balance between normal operation (depth and sea state), and extreme sea states, both cage–mounted and ship–mounted systems achieve similar attenuation of cage motion and the tension in the tether (by approximately a factor of 2). Our results show that if the stiffness and damping characteristics are appropriately chosen, both systems attenuate the motion of the cage and tension in the tether and eliminate snap loading for all operating depths. Thus, the ROV system can operate in rougher seas with less damage to the tether and cage. However, in extreme seas, the cage–mounted system performs better and eliminates all snap loads while the ship–mounted system does not.

Perhaps the greatest advantage of the cage–mounted system is its simplicity. When mounted on the ship, any compensation system will require adjustment during deployment/recovery to counteract the increasing/decreasing overboard weight of the tether. Thus, the ship–mounted system will require external input and adjustment which would render it much more complicated than the cage–mounted compensator. In the case of the ROPOS ROV system, the overboard weight increases by a factor of 4 when the system is lowered from the surface to its maximum operating depth. Thus, the ship–mounted system would also have to be built to withstand forces that are four times greater than for a cage–mounted unit. The cage–mounted compensator has the advantage of a constant mean load, and requires no adjustment. Because the cage–mounted system is autonomous and simpler in design, it is less likely to fail and will require less maintenance. By contrast, the design of a cage–mounted system would have to deal with issues of survivability at great depths. Nevertheless, we believe that the cage is a better

location for mounting a passive compensation system since it would provide similar performance in a much simpler form.

7 Conclusions

In this paper, we compared the performance of ship–mounted and cage–mounted pneumatic compensation systems for the ROPOS ROV. The compensation systems were investigated over the range of operating depths of the ROV systems, and for a range of compensator displacements (and stiffness). The ship and cage–mounted compensation systems proved effective at reducing the rms cage motion and rms tension at the ship. The best results are achieved at an operating depth of 8 200 ft (2 500 m) with the most compliant compensators. For all but the maximum operating depth, 16 400 ft (5 000 m), the effectiveness of the compensators increased with increasing range of travel, Δ_T. At 16 400 ft (5 000 m), the second natural frequency of the system of the cage compensated system was brought closer to, and eventually into, the wave–band as Δ_T was increased. Thus, the rms reduction ratio of the tension began to increase with increasing Δ_T and the cage motion became out of phase with the ship motion. During extreme seas, snap loading did not occur for the cage compensated system even though the tether went slack. Conversely, snap loading did occur in the ship compensated system in extreme seas and the entire overboard system was jerked (albeit much more mildly than without a compensation system) when the upper end stop was reached.

The reduction in the cage motion and tension in the tether (by approximately a factor of 2) were similar for the ship and cage–mounted compensation systems in all

cases investigated. Although the ship mounted system was slightly more effective, we believe that the cage mounted system would be a better choice because of its simplicity and operation in extreme seas.

Acknowledgements

The authors gratefully thank Jim McFarlane and the staff of International Submarine Engineering (ISE) for their continual support and assistance in this project. F.R. Driscoll was financially supported by the Natural Sciences and Engineering Research Council (NSERC), the Science Council of British Columbia (SCBC) and ISE. This work was also supported by the Office of Naval Research under contract N00014-93-1-0362 and NSERC.

References

Bennett, P. and Forex, S., 1997, "Active heave: the benefits to operations as seen in the north sea," Proceedings of the SPE/IADC Drilling Conference, pp. 207-217.

Driscoll F.R., Lueck R.G., and Nahon M., 1999a, "The motion of a deep–sea remotely operated vehicle system. Part 1: motion observations," Ocean Engineering, in press.

Driscoll F.R., Lueck R.G., and Nahon M., 1999b, "The motion of a deep–sea remotely operated vehicle system. Part 2: analytic model," Ocean Engineering, in press.

Driscoll, F.R., Lueck, R.G., and Nahon, M., 1999c, "Development and Validation of a Lumped–Mass Dynamics Model of a Deep–Sea ROV System," Submitted to Applied Ocean Research.

Gaddy, D.E., 1997, "Ultradeep drillship will react to heave with electric–heave compensating draworks," Oil & Gas Journal, July, pp. 68

Hover, F.S., Grosenbaugh, M.A., and Triantafyllou, M.S., 1994, "Calculation of dynamic motions and tension in towed underwater cables," IEEE Journal of Oceanic Engineering. Vol. 19, pp. 449–457.

ISE 1998, International Submarine Engineering Hysub 5000, 1734 Broadway Street, Port Coquitlam, B.C., Canada, V3C 2M8, web page, http://www.ise.bc.ca/rov.html#hys5000.

Kirstein, H., 1986, "Active heave compensation systems on board vessels and offshore rigs," Marine Technology, Vol 17, pp. 59-61.

Korde, U.A., 1998, "Active heave compensation on drill–ships in irregular waves," Ocean Engineering, Vol. 25, pp. 541-561.

Mellem T., 1979, "Surface handling of diving bells and submersibles in rough sea," Proceedings of the Offshore Technology Conference, Houston, Texas, pp. 1571–1580.

Moran, J.M. and Shapiro, H.N., 1992, "Fundamentals of Engineering Thermodynamics," John Wiley & Sons, Inc. pgs 804.

Niedzwecki, J.M., and Thampi, S.K., 1988, "Heave compensated response of long multi-segment drill strings," Applied Ocean Research, Vol. 10, pp. 181-190.

Niedzwecki, J.M., and Thampi, S.K., 1991, "Snap loading of marine cable systems," Applied Ocean Research, Vol. 13, pp. 210–218.

W.H. Press, S.A., Teukolsky, W.T., Vetterling, and B.P. Flannery, et al, 1992, "Numerical Recipes in C," Cambridge University Press.

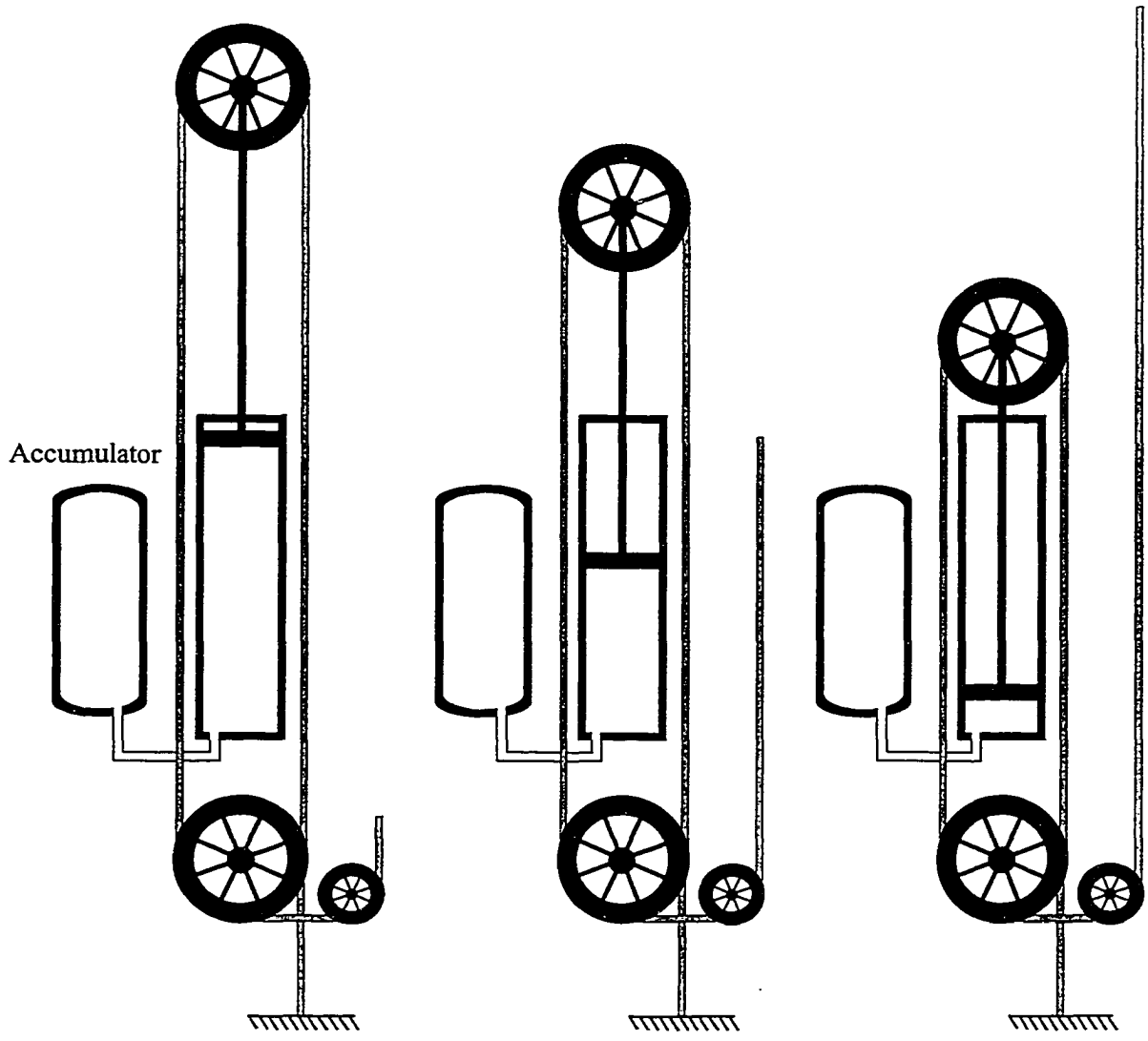

Fig.1. Diagrammatic representation of a cage mounted heave compensation system at full extension, half extension and full retraction.

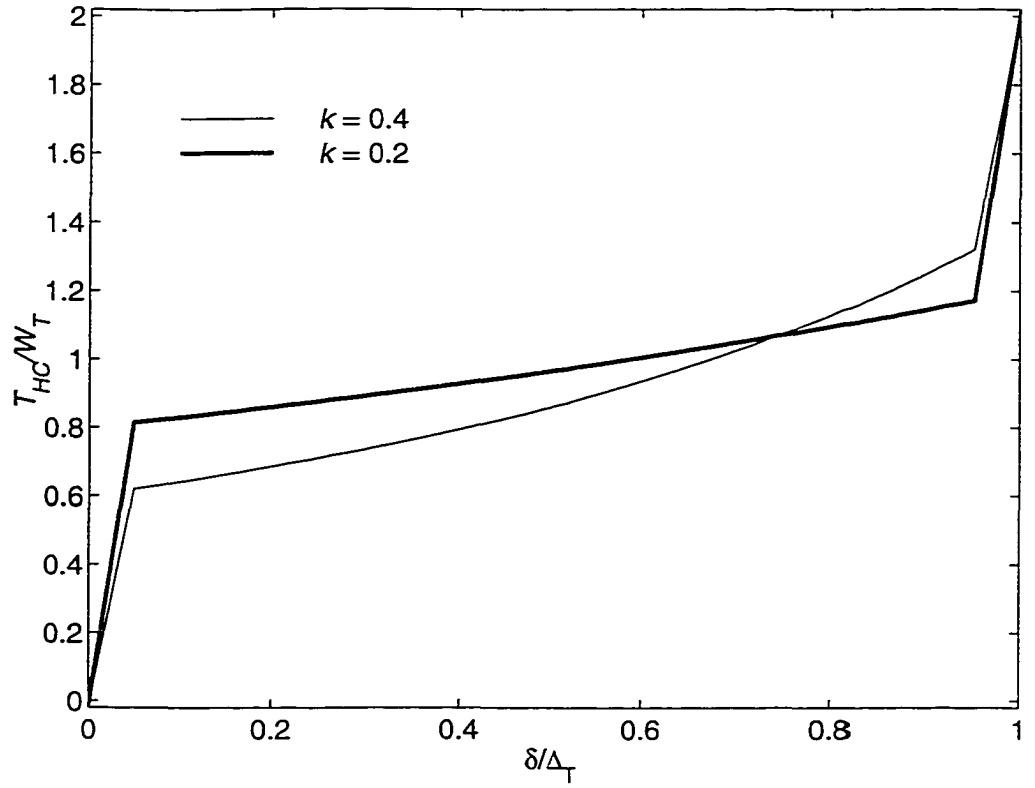

Fig. 2. The spring force versus compensator displacement for the cage–mounted pneumatic passive compensator for $k = 0.2$ (think line) and $k = 0.4$ (thin line).

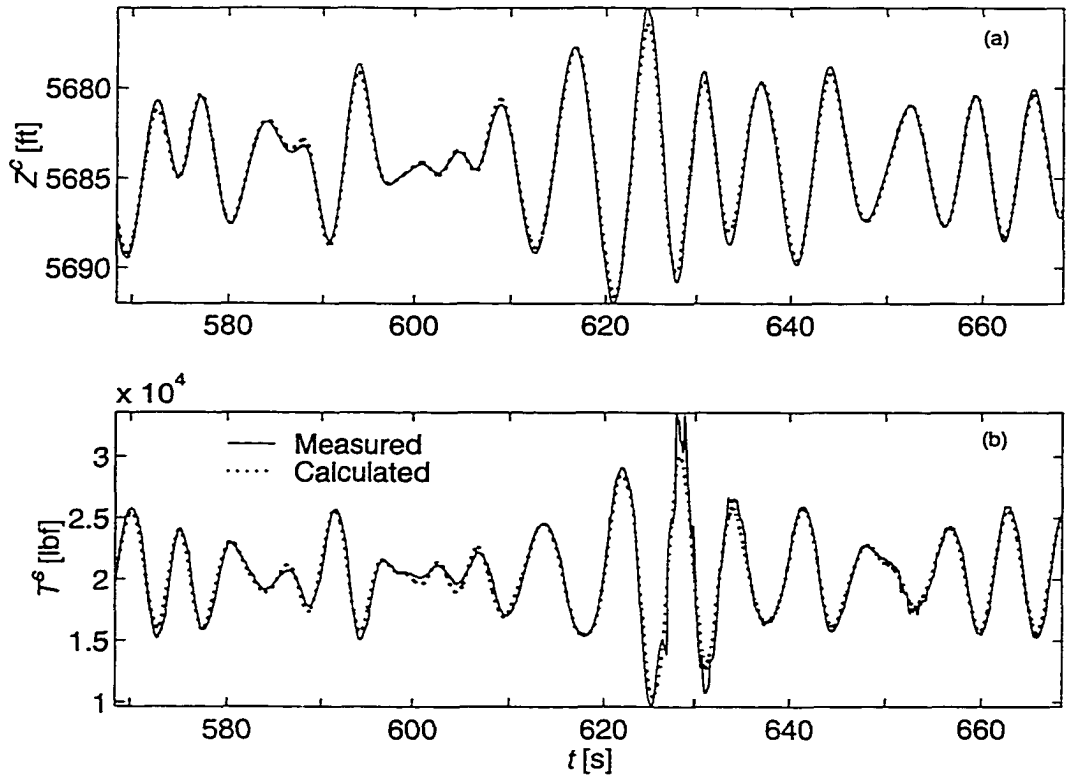

Fig. 3. The measured (solid line) and model calculated (dashed line) position of the cage (a) and tension in tether at the ship (b). To make viewing more intuitive, the y–axis of (a) has been flipped.

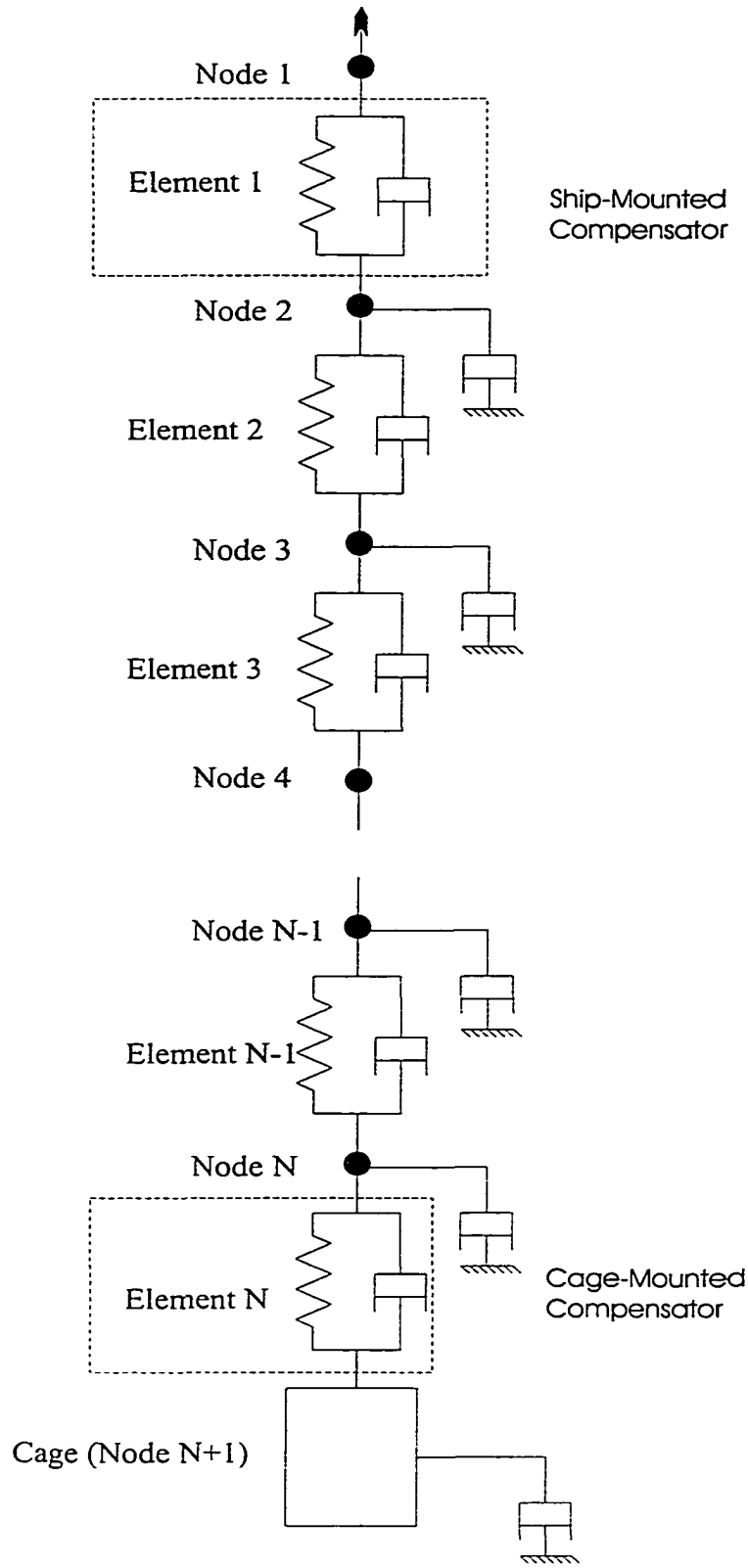

Fig. 4. Diagrammatic representation of the finite–element lumped–mass model. The compensators (when included) are represented by the elements enclosed by the dashed lines.

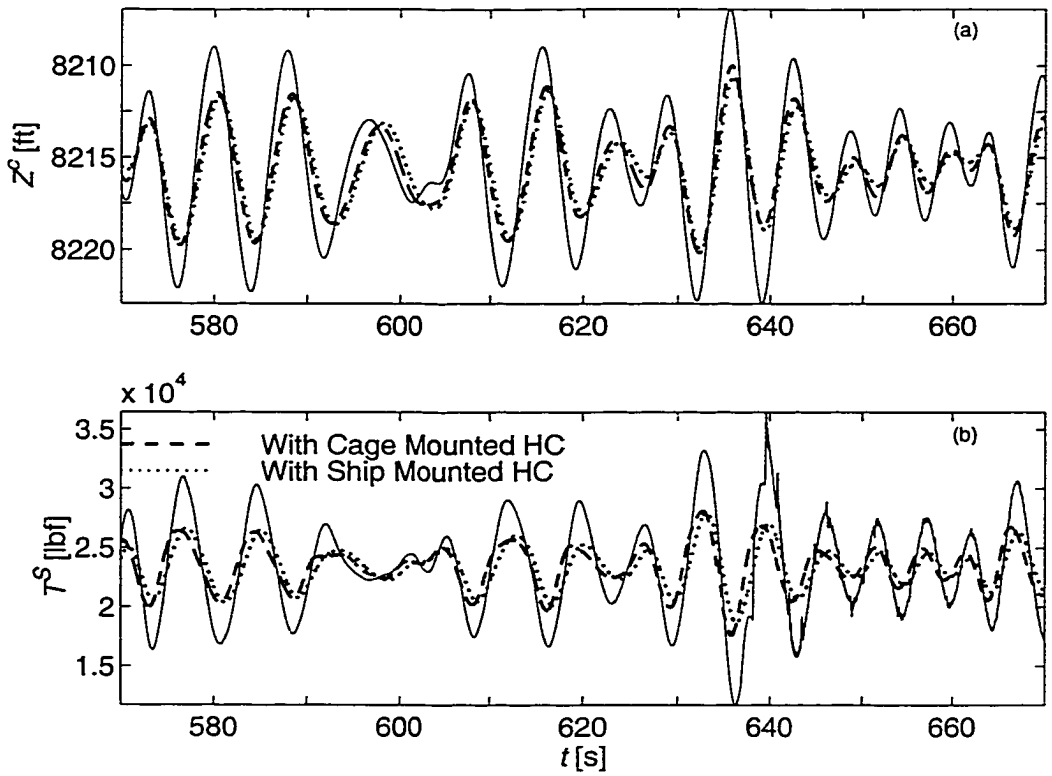

Fig. 5. Short time series of the cage motion (a) and tension in tether at the ship (b) for the uncompensated system, for the system with ship–mounted compensation and for the system with cage–mounted compensation

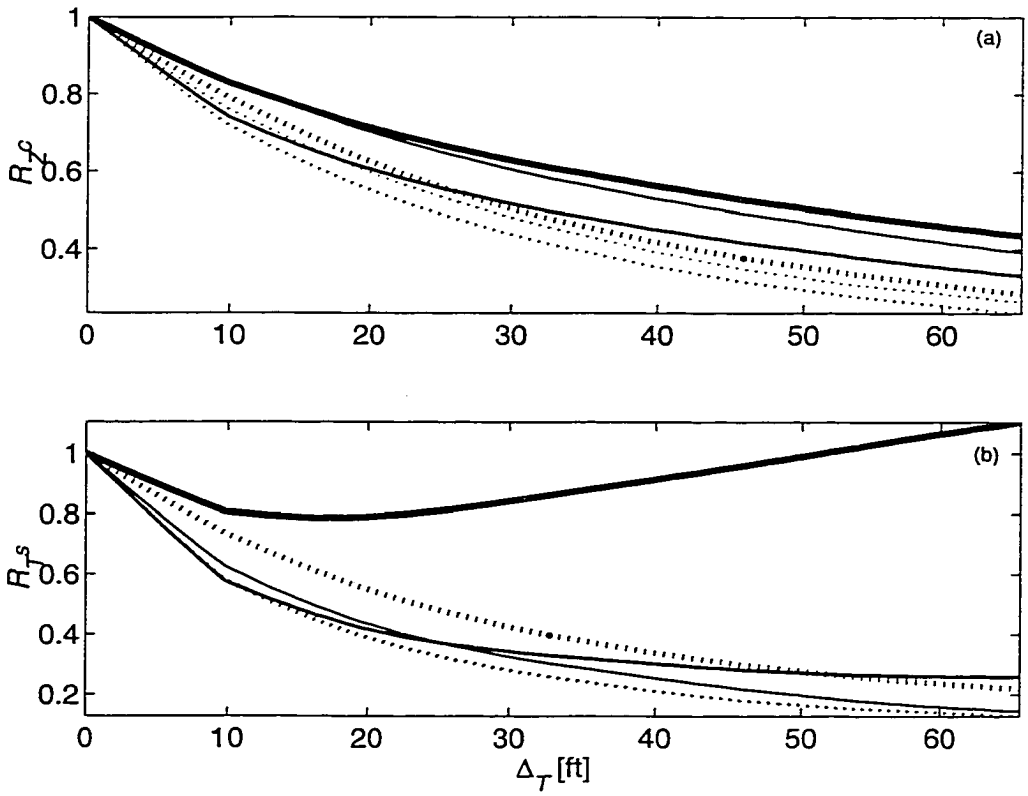

Fig. 6. The rms reduction ratio for the position of the cage (a) and the tension in the tether at the ship (b) are plotted for ship–mounted (dashed lines) and cage–mounted (solid lines) compensation systems.

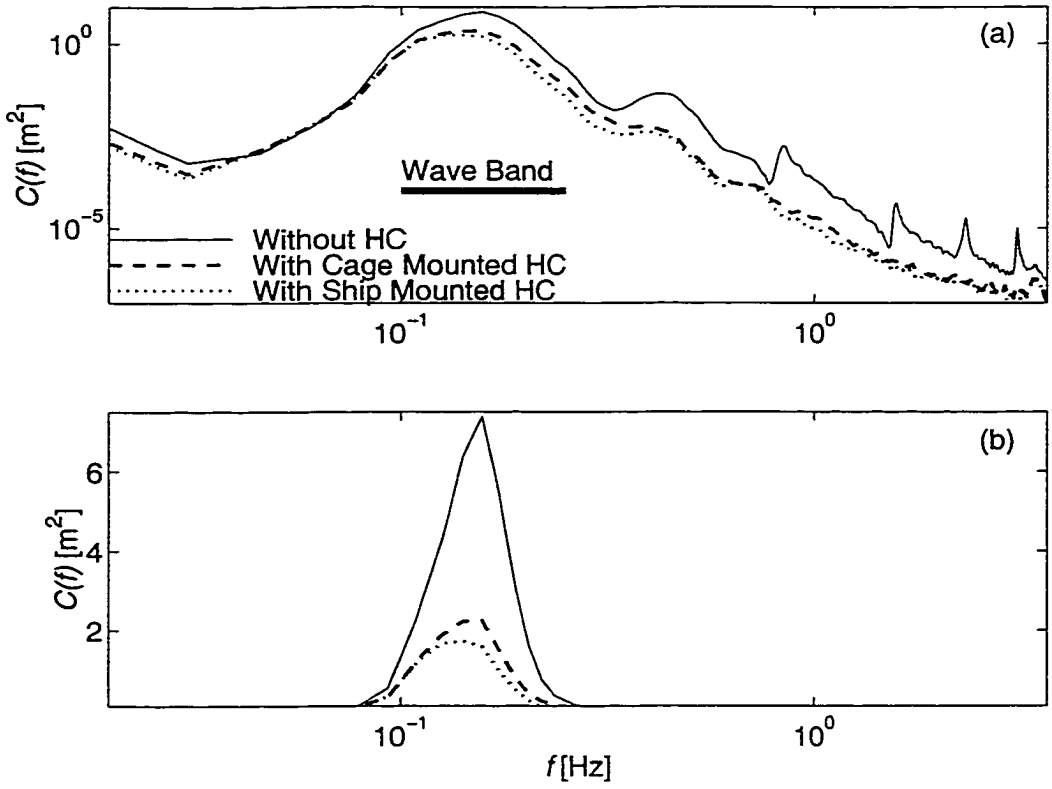

Fig. 7 Spectra (a) and variance preserving spectra (b) of the acceleration of the cage at a depth of 8 200 ft (2 500 m). Values for the uncompensated system (solid line), the cage–mounted (dashed line) and ship–mounted (dotted line) compensated systems Δ_T = 16.4 ft (5 m) are overlaid for comparison.

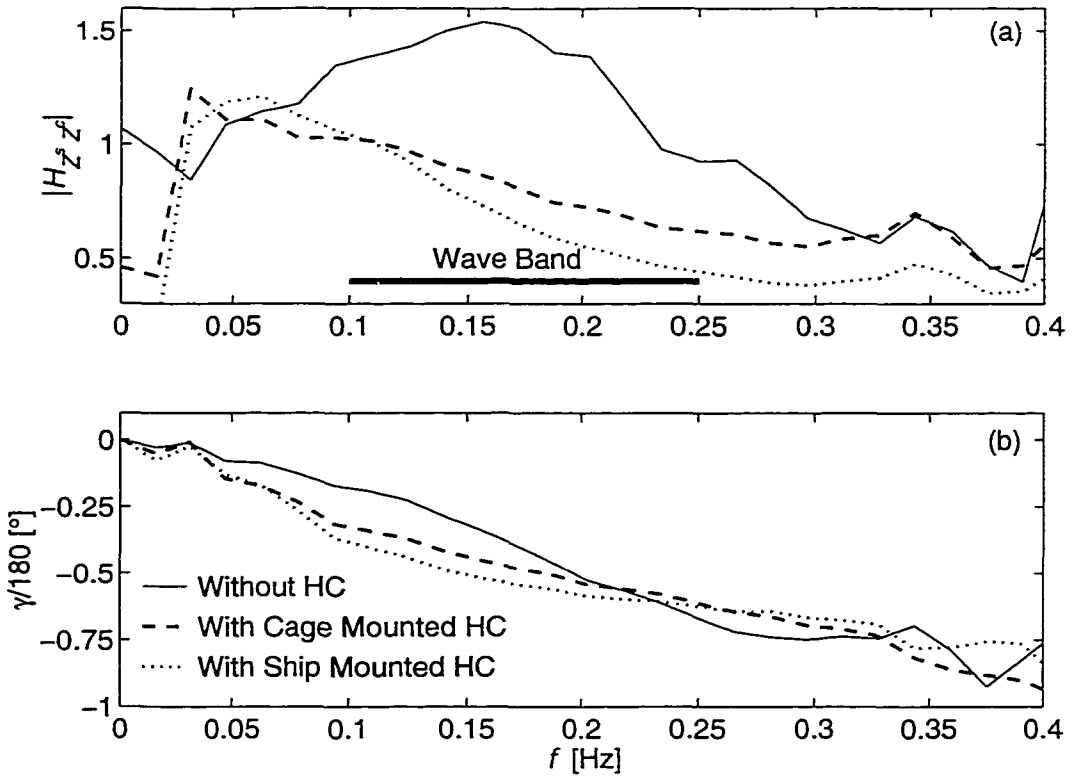

Fig. 8. The magnitude (a) and phase (b) of the transfer function between ship and cage motion estimated from the position records for operation at 8 200 ft (2 500 m). Estimates for the uncompensated system (solid line) and for the cage (dashed line) and ship (dotted line) compensated system with Δ_T = 16.4 ft (5 m) and are overlaid for comparison.

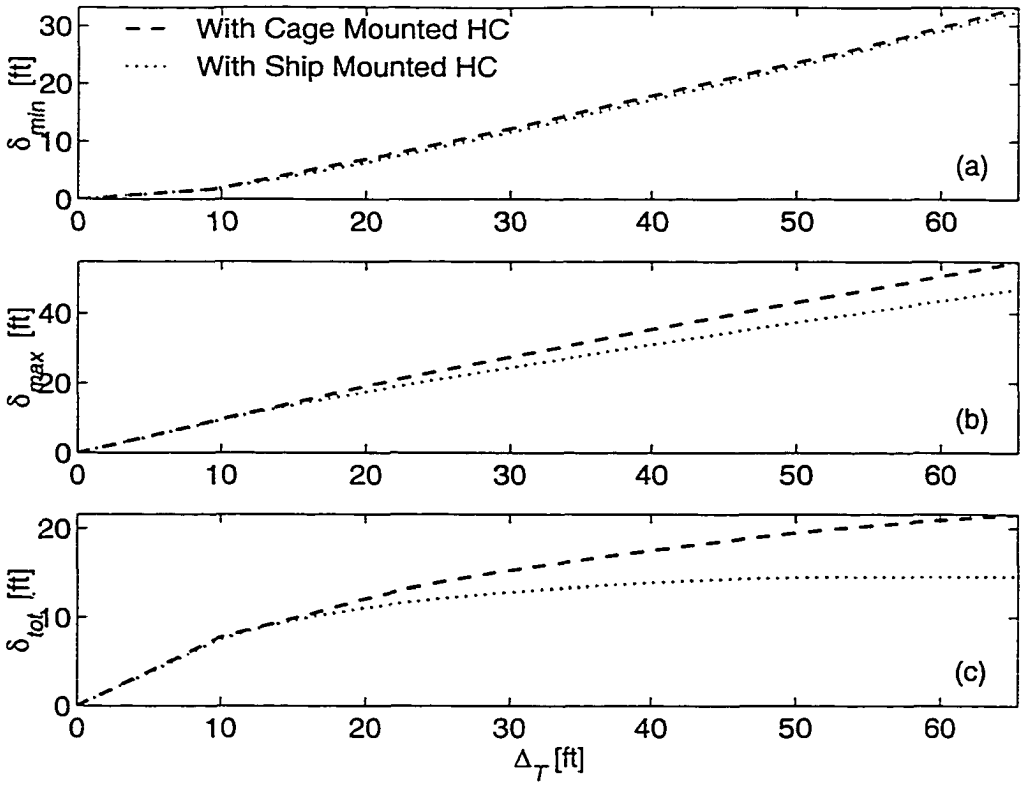

Fig. 9. The minimum (a), maximum (b) and total travel (c) of the cage–mounted (dashed line) and ship–mounted (dotted line) compensation systems.

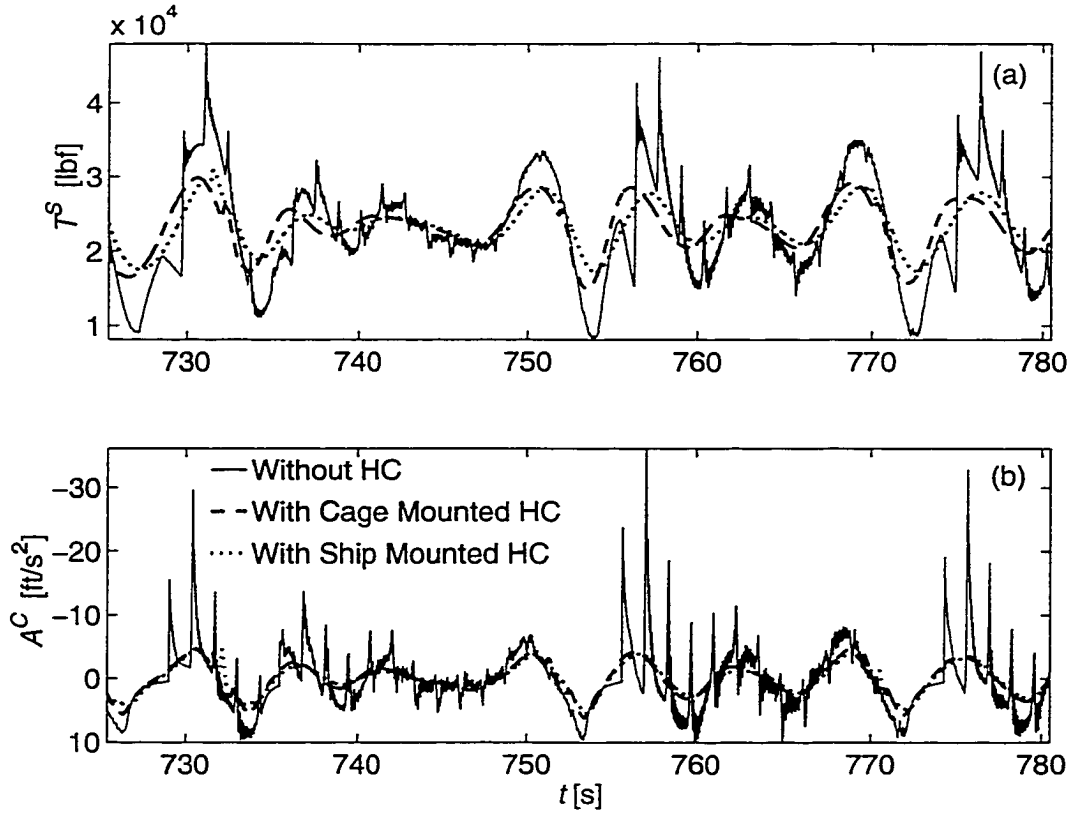

Fig. 10. The tension in the tether at the ship (a) and the acceleration of the cage (b) for the uncompensated system (solid line), cage compensated system (dashed line) and ship compensated system (dotted line)for S_A = 14.4 ft (4.4 m).

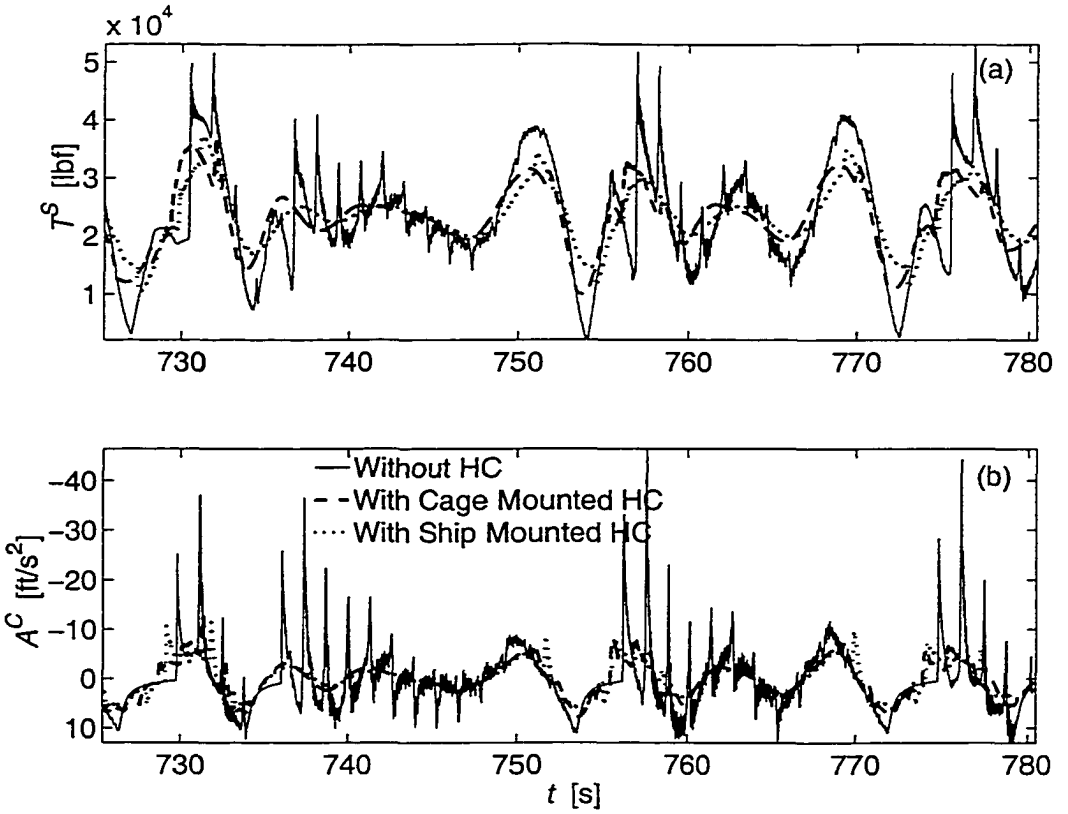

Fig. 11. The tension in the tether at the ship (a) and the acceleration of the cage (b) for the uncompensated system (solid line), cage compensated system (dashed line) and ship compensated system (dotted line)for $S_A = 21.7$ ft (6.6 m).

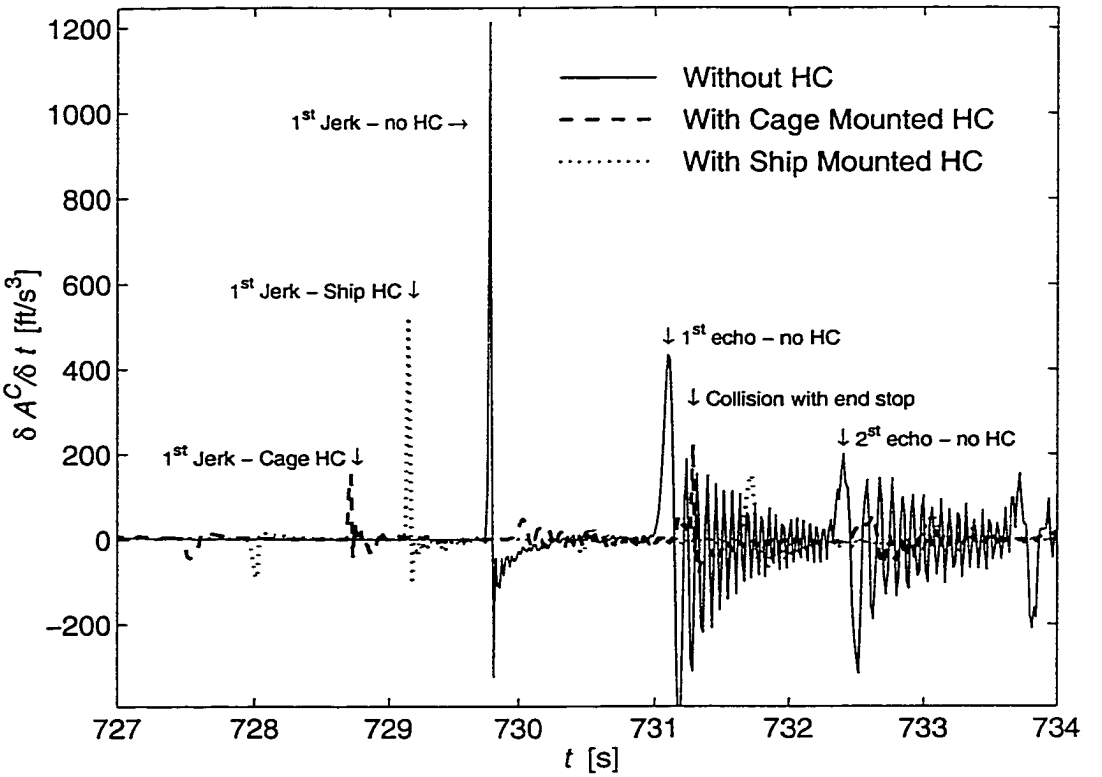

Fig. 12. Time derivative of the acceleration of the cage (jerk) for the uncompensated system (solid line), cage compensated system (dashed line) and the ship compensated system (dotted line) for $S_A = 21.7$ ft (6.6 m).

Appendix E

Discretization of the Tether Equation

Discretization of the Tether Equation

Substituting (C2), (C3), (C4), and (C5) into (4.1) we obtain the balance of forces in the tangent direction at point p in element i using a coupled set of reference and elastic coordinates:

$$m_i\left(\ddot{z}+\ddot{u}_i\right)=\frac{\partial}{\partial s}\left(E_iA_i\frac{\partial u_i}{\partial s}\right)+\left(\rho_c(s)-\rho_w\right)A_ig-\frac{1}{2}\rho_wA_i\left(\frac{\partial u_i}{\partial s}+1\right)C_D^i\left(\dot{Z}+u_i\right)\left|\dot{Z}+u_i\right|$$

The elastic displacement is approximated using the trial solution developed in Appendix C. For element i, the trial solution is:

$$u_i\approx\tilde{u}_i(s,t;a)=u_i^{(1)}(t)\phi_{i,1}(s)+u_i^{(2)}(t)\phi_{i,2}(s)$$

where

$$\phi_{i,1}(s)=\frac{s_i^{(2)}-s}{s_i^{(2)}-s_i^{(1)}}\qquad\phi_{i,2}(s)=\frac{s-s_i^{(1)}}{s_i^{(2)}-s_i^{(1)}}$$

The form of Galerkin's method is:

$$\int_{s_i^{(1)}}^{s_i^{(2)}}R_i(s,t;u)\phi_{i,j}ds=0\qquad j=1,2$$

where the residual is:

$$R_i(s,t;u)=m_i(\ddot{Z}+\ddot{\tilde{u}}_i)-\frac{\partial}{\partial s}EA\frac{\partial\tilde{u}^i}{\partial s}-(m_i-\rho_wA_i)g+1/2\rho_wA_i(\varepsilon+1)C_D^i\left((\dot{Z}+\dot{\tilde{u}}_i)\left|\dot{Z}+\dot{\tilde{u}}_i\right|\right)$$

where $\varepsilon << 1$ and therefore $\varepsilon + 1 \approx 1$. The integral is simplified by termwise separtion of the residual such that $R_i = \sum_{k=1}^{5} R_{i,k}$ and the coresponding terms are:

$$R_{i,1}(s,t;u) = m_i(\ddot{Z}); \qquad R_{i,2}(s,t;u) = m_i(\ddot{\tilde{u}}_i) \qquad R_{i,3}(s,t;u) = -\frac{\partial}{\partial s} EA \frac{\partial \tilde{u}_i}{\partial s};$$

$$R_{i,4}(s,t;u) = -(m_i - \rho_w A_i)g; \quad \text{and} \quad R_{i,5}(s,t;u) = 1/2\rho_w A_i C_D^i \left((\dot{Z} + \dot{\tilde{u}}_i)\left|\dot{Z} + \dot{\tilde{u}}_i\right|\right);$$

Terms $R_{i,1}$ and $R_{i,5}$ do not invovle the trial solution integrate to:

$$R_{i,k}(s,t;u) \int_{s_i^{(1)}}^{s_i^{(2)}} \phi_{i,j}(s)ds = \tfrac{1}{2} R_{i,k}(s,t;u) l_i \qquad j = 1,2; k = 1,6$$

where $l = s_i^{(2)} - s_i^{(1)}$. Applying Galerkin's method to $R_{i,2}$ yeilds the consistent mass representation:

$$\begin{bmatrix} m_i \int_{s_i^{(1)}}^{s_i^{(2)}} \ddot{\tilde{u}}_i \phi_{i,1}(s)ds \\ m_i \int_{s_i^{(1)}}^{s_i^{(2)}} \ddot{\tilde{u}}_i \phi_{i,2}(s)ds \end{bmatrix} = m_i l_i \begin{bmatrix} 1/3 & 1/6 \\ 1/6 & 1/3 \end{bmatrix} \begin{bmatrix} \ddot{u}_i^{(1)} \\ \ddot{u}_i^{(2)} \end{bmatrix}$$

We integrate $R_{i,3}$ by parts and obtain:

$$\begin{bmatrix} -E_i A_i \left(\frac{\partial \tilde{u}}{\partial s} \phi_{i,1} \Big|_{s_a}^{s_b} - \int_{s_a}^{s_b} \frac{\partial \tilde{u}}{\partial s} \frac{\partial \phi_j}{\partial s} ds \right) \\ -E_i A_i \left(\frac{\partial \tilde{u}}{\partial s} \phi_{i,2} \Big|_{s_a}^{s_b} - \int_{s_a}^{s_b} \frac{\partial \tilde{u}}{\partial s} \frac{\partial \phi_j}{\partial s} ds \right) \end{bmatrix} = \frac{E_i A_i}{l_i} \begin{bmatrix} 1 & -1 \\ -1 & 1 \end{bmatrix} \begin{bmatrix} u_i^{(1)} \\ u_i^{(2)} \end{bmatrix} + \begin{bmatrix} \beta_i^{(1)} \\ \beta \end{bmatrix}$$

where the boundary terms are:

$$\beta_i^{(1)} = E_i A_i \frac{\partial \tilde{u}}{\partial s} \phi(s_i^{(1)})_{i,1}$$

$$\beta_i^{(2)} = E_i A_i \frac{\partial \tilde{u}}{\partial s} \phi(s_i^{(2)})_{i,2}$$

Expanding $R_3(z,t;u)$ and evaluating for positive $\dot{Z}+\dot{\tilde{u}}_i$

$$\begin{bmatrix} \frac{\rho_W A_i}{2} \int_{s_i^{(1)}}^{s_i^{(2)}} C_D^i \left(\dot{Z}+\dot{\tilde{u}}_i\right)^2 \phi_{i,1} ds \\ \frac{\rho_W A_i}{2} \int_{s_i^{(1)}}^{s_i^{(2)}} C_D^i \left(\dot{Z}+\dot{\tilde{u}}_i\right)^2 \phi_{i,2} ds \end{bmatrix} = \frac{\rho_W C_D^i D_i l_i}{2} \begin{bmatrix} \left(\frac{1}{3}\left(\dot{Z}+\dot{u}_i^{(1)}\right)^2 + \frac{1}{6}\left(\dot{Z}+\dot{u}_i^{(2)}\right)^2 - \frac{1}{12}\left(\dot{u}_i^{(1)}-\dot{u}_i^{(2)}\right)^2\right) \\ \left(\frac{1}{6}\left(\dot{Z}+\dot{u}_i^{(1)}\right)^2 + \frac{1}{3}\left(\dot{Z}+\dot{u}_i^{(2)}\right)^2 - \frac{1}{12}\left(\dot{u}_i^{(1)}-\dot{u}_i^{(2)}\right)^2\right) \end{bmatrix}$$

and thus, when $\dot{Z}+\dot{\tilde{u}}_i$ is either positive or negative over element i, the discritized form of $R_3(z,t;u)$ is:

$$\begin{bmatrix} f_i^{(1)} \\ f_i^{(2)} \end{bmatrix} = \frac{\rho_W C_D^i D_i l_i}{2} \begin{bmatrix} \left(\frac{1}{3}\left(\dot{Z}+\dot{u}_i^{(1)}\right)\left|\dot{Z}+\dot{u}_i^{(1)}\right| + \frac{1}{6}\left(\dot{Z}+\dot{u}_i^{(2)}\right)\left|\dot{Z}+\dot{u}_i^{(2)}\right| - \frac{1}{12}\left(\dot{u}_i^{(1)}-\dot{u}_i^{(2)}\right)\left|\dot{u}_i^{(1)}-\dot{u}_i^{(2)}\right|\right) \\ \left(\frac{1}{6}\left(\dot{Z}+\dot{u}_i^{(1)}\right)\left|\dot{Z}+\dot{u}_i^{(1)}\right| + \frac{1}{3}\left(\dot{Z}+\dot{u}_i^{(2)}\right)\left|\dot{Z}+\dot{u}_i^{(2)}\right| - \frac{1}{12}\left(\dot{u}_i^{(1)}-\dot{u}\right)\left|\dot{u}_i^{(1)}-\dot{u}_i^{(2)}\right|\right) \end{bmatrix}$$